4-2020

Synthesis, Characterization, Electronic Structure of Reduced Graphene Oxide and NH_2-MIL-125(Ti) Modified $BiNbO_4$ and Their Photocatalytic Activities

Maram Yahya Bakiro

Recommended Citation

Bakiro, Maram Yahya, "Synthesis, Characterization, Electronic Structure of Reduced Graphene Oxide and NH_2-MIL-125(Ti) Modified $BiNbO_4$ and Their Photocatalytic Activities" (2020). *Chemistry Theses*. 10.
https://scholarworks.uaeu.ac.ae/chem_theses/10

United Arab Emirates University

College of Science

Department of Chemistry

SYNTHESIS, CHARACTERIZATION, ELECTRONIC STRUCTURE OF REDUCED GRAPHENE OXIDE AND NH_2-MIL-125(Ti) MODIFIED $BiNbO_4$ AND THEIR PHOTOCATALYTIC ACTIVITIES

Maram Yahya Bakiro

This thesis is submitted in partial fulfilment of the requirements for the degree of
Master of Science in Chemistry

Under the Supervision of Dr. Ahmed H. Alzamly

April 2020

Declaration of Original Work

I, Maram Yahya Bakiro, the undersigned, a graduate student at the United Arab Emirates University (UAEU), and the author of this thesis entitled "*Synthesis, Characterization, Electronic Structure of Reduced Graphene Oxide and* NH_2*-MIL-125(Ti) Modified* $BiNbO_4$ *and its Photocatalytic Activities*", hereby, solemnly declare that this thesis is my own original research work that has been done and prepared by me under the supervision of Dr. Ahmed H. Alzamly, in the College of Science at UAEU. This work has not previously been presented or published or formed the basis for the award of any academic degree, diploma or a similar title at this or any other university. Any materials borrowed from other sources (whether published or unpublished) and relied upon or included in my thesis have been properly cited and acknowledged in accordance with appropriate academic conventions. I further declare that there is no potential conflict of interest with respect to the research, data collection, authorship, presentation and/or publication of this thesis.

Student's Signature: ______________________ Date: ___April 16, 2020__

Advisory Committee

1) Advisor: Ahmed H. Alzamly
Title: Associate Professor
Department of Chemistry
College of Science

2) Co-advisor: Muna B. Alfalasi
Title: Associate Professor
Department of Chemistry
College of Science

Approval of the Master Thesis

This Master Thesis is approved by the following Examining Committee Members:

1) Advisor (Committee Chair): Ahmed H. Alzamly
   Title: Associate Professor
   Department of Chemistry
   College of Science

   Signature _________ ___ Date Apri 16, 2020

2) Member: Haythem Ali Mohammad Saadeh
   Title: Associate Professor
   Department of Chemistry
   College of Science

   Signature _________ ____ Date Apri 16, 2020

3) Member (External Examiner): Nathir Al-Rawashdeh
   Title: Professor
   Department of Chemistry
   Institution: Higher College of Technology, UAE

   Signature _______ _______ Date Apri 16th,2020

This Master Thesis is accepted by:

Acting Dean of the College of Science: Professor Maamar Ben Kraouda

Signature Maamar Benkraouda Date July 5, 2020

Dean of the College of Graduate Studies: Professor Ali Al-Marzouqi

Signature Ali Hassan Date July 5, 2020

Copy ____ of ____

Abstract

The present thesis focuses on the design and synthesis of novel visible light photocatalysts for CO_2 utilization. In recent years, Bi-based materials have shown remarkable photocatalytic activity in the field of CO_2 reduction. Particularly, $BiNbO_4$ has many promising applications as a visible light harvesting material due to its band gap position and orbital hybridization. In this study, an intensive effort has been made to study the effect of different reaction parameters such as temperature and pH of different synthetic methodology applied. The new photocatalytic materials have been characterized using different characterization techniques including PXRD, BET, SEM, EDX and UV-Vis DRS. Since the activity of $BiNbO_4$ is limited due to high recombination rate of the photogenerated electron-hole pairs and the low surface area, to minimize this effect, reduced graphene oxide modified $BiNbO_4$ composite material was fabricated using simple mechanical mixing. Moreover, Ti-based amine functionalized metal organic frameworks (MOFs) modified $BiNbO_4$ hybrid material was also prepared. The activity of prepared $BiNbO_4$/r-GO heterojunction photocatalysts was examined for the cycloaddition of CO_2 with propylene oxide as a photocatalytic model reaction. Interestingly, no polymeric material was formed and selective cyclic propylene carbonate in high yield was obtained, with the highest yield obtained when using 5% r-GO by mass. Furthermore, the activity of $BiNbO_4$/NH_2-MIL-125(Ti) was found increase upon the addition of 50% NH_2-MIL-125(Ti) by mass.

Keywords: $BiNbO_4$, photocatalysis, light harvesting, reduced graphene oxide (r-GO), metal organic framework (MOF), carbon dioxide.

Title and Abstract (in Arabic)

تحضير وتوصيف ودراسة البنية الالكترونية ل $BiNbO_4$ المعدل بأكسيد الجرافين المختزل وبمادة NH_2-MIL-125(Ti) وتحديد نشاطه كحافز ضوئي

الملخص

الهدف من هذه الأطروحة هو تصميم وتحضير مواد جديدة لها القدرة على التحفيز الضوئي واستخدامها في تفاعلات ثاني أوكسيد الكربون. في السنوات الأخيرة، أظهرت المواد العضوية المكونة من عنصر البزماث نشاطًا تحفيزيًا رائعًا في مجال الحد من ثاني أوكسيد الكربون. على وجه الخصوص $BiNbO_4$ الذي يتمتع بالعديد من الخصائص و التطبيقات الواعدة في مجال التحفيز الضوئي وذلك بسبب بنيته الاكترونية والمدارية التي تنشط في نطاق الضو المرئي. حيث اثبتت الدراسات الحديثة مدى فاعليته في مجال صناعة غاز ثاني أوكسيد الكربون. في هذه الأطروحة، تمت دراسة تأثير معاملات التفاعل المختلفة مثل درجة الحرارة ودرجة الحموضة على البنية الذرية وخصائص $BiNbO_4$ المحضر. تم توصيف المواد التحفيزية الجديدة المحضرة باستخدام تقنيات توصيف مختلفة بما في ذلك PXRD و BET و SEM و EDX و UV-Vis DRS. نظرًا لأن نشاط $BiNbO_4$ محدود بسبب سرعة معدل إعادة معادلة الشحنات المولدة ضوئيًا وكذلك مساحة السطح المنخفضة نسبيا، تم تصنيع مادة $BiNbO_4$ المعدلة بأوكسيد الجرافين المختزل باستخدام الخلط الميكانيكي. علاوة على ذلك، تم تحضير $BiNbO_4$ المعدل باستخدام مادة (MOFs) المصنة من التيتانيوم NH_2-MIL-125 (Ti). تم تحديد نشاط المحفزات الضوئية المعدلة بأوكسيد الجرافين المختزل $BiNbO_4$ / r-G تحت اشعة الضوء المرئي بإضافة ثاني أكسيد الكربون لأوكسيد البروبيلين كتفاعل نموذجي. من المثير للاهتمام أنه لم يتم تكوين أي مادة بوليمرية وتم الحصول على cyclic propylene carbonate بشكل انتقائي وبكمية وفيرة. مع الحصول على أعلى إنتاجية عند استخدام خمسة بالمئة من أوكسيد الجرافين المختزل. علاوة على ذلك، تم زيادة نشاط $BiNbO_4$/NH_2-MIL-125 (Ti) عند إضافة خمسين بالمئة NH_2-MIL-125 (Ti).

مفاهيم البحث الرئيسية: المحفزات الضوئية، التحفيز الضوئي، أوكسيد الجرافين، ثاني أكسيد الكربون، metal organic framework (MOF)، $BiNbO_4$.

Acknowledgements

First and foremost, I am very grateful to GOD Almighty for the blessing and courage that have made this research and thesis possible.

Immeasurable appreciation and deep gratitude to my supervisor Prof. Ahmed H. Alzamly for giving me the opportunity to work in his lab and providing invaluable guidance and continues support throughout this thesis. His vitality, vision, dedication, sincerity and motivation have deeply inspired me. It was a great privilege to work under his supervision. I am extremely grateful for what he has offered me. I would also like to thank him for his friendship, empathy and great sense of humor.

I am extremely grateful to my beloved father Yahya Bakiro who encouraged and believed in me and the amazing, remarkable, loving mother Hind Mustafa for their continues support. I appreciate your love and effort in making me a better person. I achieved great things because of your prayers and good counsel.

I am very much thankful to my brother Mohammed Amin and my sister Muzna who offered invaluable support and humor over the years. A minute of communicating with you brings me so much joy and pleasure that it is enough for me for the whole day. Thank you for being joyful no matter what.

I am very much indebted to my best friend Salwa Ahmed who has a wonderful ability to read my mind. It is great, because this is what friendship is all about. Thank you for being the sympathetic, kind and generous friend I always wanted to have. I am really grateful for having you in my life.

Dedication

To my beloved parents and family

Table of Contents

List of Tables

List of Figures

List of Abbreviations

α	Absorptivity Coefficient
Å	Angstrom
BET	Brunauer-Emmett-Teller
Bi	Bismuth
$BiVO_4$	Bismuth Vanadate
CB	Conduction Band
CCs	Cyclic Carbonates
CdS	Cadmium Sulfate
CO_2	Carbon Dioxide
DIW	Deionized Water
DPC	Diphenyl Carbonate
DRS	Diffused Reflectance Spectroscopy
EDX	Energy Dispersive X-Ray Spectroscopy
E_g	Band Gap
eV	Electron Volt
Fe	Iron
GPa	Giga Paskal
h	Planck Constant
H_2	Hydrogen Gas
IPCC	Intergovernmental Panel on Climate Change
IR	Infrared
K	Kelvin

MIL	Matériaux de l′Institut Lavoisier
Mn	Manganese
MOFs	Metal Organic Frameworks
Nb	Niobium
Ni	Nickel
NMR	Nuclear Magnetic Resonance
PC	Propylene Carbonate
PXRD	Powder X-Ray Diffraction
r-GO	Reduced Graphene Oxide
RPM	Rounds Per Minute
SEM	Scanning Electron Microscopy
SYS	System
Ta	Tantalum
TiO_2	Titanium Dioxide
TW	Terawatt
UV	Ultraviolet
V	Voltage
v	Light Frequency
VB	Valence Band
Vis	Visible
WO_3	Tungsten Oxide
Zn	Zinc
ZnO	Zinc Oxide
ZnS	Zinc Sulfide

Chapter 1: Introduction

1.1 Overview

The global energy supply is mainly provided by the combustion of fossil fuels which resulted in a rapid increase of the atmospheric carbon dioxide level, in turn, triggering a cascade of environmental and health problems.[1] According to the Intergovernmental Panel on Climate Change (IPCC), the greenhouse gas emissions should be reduced to half by 2030 in order to mitigate climate change.[2] Moreover, the continuous depletion of fossil fuels reserves necessitates a demand for secure, clean, and sustainable energy supply for the future.[3] Therefore, the conversion of CO_2 into commercially valuable chemicals is an essential goal that would positively impact global carbon neutrality by recycling CO_2 into usable products such as fuel, value-added chemicals and starting materials for polymeric products. In this context, a growing number of research facilities are already pursued this goal. George Olah carbon dioxide to renewable methanol plant, Reykjanes, Iceland, is an example of a chemical plant that converts CO_2 into methanol.[4] Asahi Kasei Chemicals in Tokyo, Japan, has developed catalysts for using CO_2 as a feedstock to produce diphenyl carbonate (DPC).[5]

Economically speaking, as a source of carbon, CO_2 can be cheaply captured.[6] However, the conversion of such stable molecule into bulk chemical compounds that are more useful, requires a huge amount of energy. This is because of the high stability of the carbon-oxygen double bonds in carbon dioxide. Figure 1 represents the length of carbon-oxygen bond in some organic molecules compared to that of CO_2. To promote sustainability, the energy needed to overcome the stability of CO_2 should come from a renewable source and not from fossil fuel, because using fossil fuel will cause more damage by producing more CO_2 to the atmosphere.

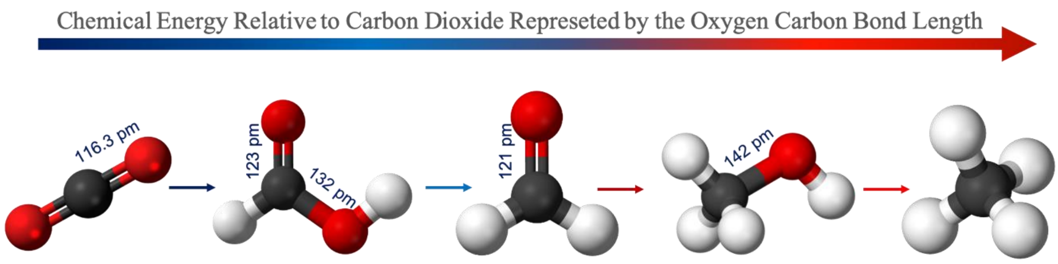

Figure 1: Chemical energy relative to CO_2. Represented by the oxygen-carbon bond length, going from left to right, the oxygen-carbon bond length elongated which means the bond has been weakened. Atoms color: oxygen (red), carbon (black) and hydrogen (weight).

Based on the above, the development of renewable, sustainable and green technologies is an urgent necessity. Such technologies include: solar, wind and others.[7,8] Solar energy is free, most abundant among all renewable energy sources. Energy from the sun reaches the earth surface at a rate of 1.2×10^5 TW by far, exceeding the current world energy consumption of 17 TW ($1TW = 10^{12}$ J/s).[9] Thus, the development of visible light driven photocatalysts is of considerable interest in the area of clean and renewable energy. In recent years, the study of semiconductor photocatalysts has attracted attention due to its potential in environmental application[10] that includes the generation of hydrogen from water splitting, fuel production from carbon dioxide reduction, selective organic transformations, and many other applications.[11,12]

1.2 CO_2 utilization via the cyclic addition of CO_2 into epoxides

The synthesis of organic cyclic carbonates (CCs) via the insertion of CO_2 into epoxides has been known for over 50 years.[13] It was first discovered in 1969 by Inoue et al.[14] Particularly, propylene carbonate (PC) is valuable as a dipolar aprotic solvent.[15] It has many industrial application where it can be found in glue, paint remover, cosmetics and it can also be used as a dispersant that helps decrease the viscosity of materials.[16] PC is a biodegradable, and nontoxic material.[17]CCs in general offer an environmentally friendly and safe alternative to the hazardous propylene oxide,[18] and the standard toxic organic solvents that includes tetrahydro furan (THF), chloroform and the aromatic solvents. Moreover, due to their high dielectric constant, (e.g., the dielectric constant of PC at 298 K is 65.5),[19] CCs are used as an electrolyte in Li-ion batteries.[20]

The cyclic addition of CO_2 into epoxide is a thermodynamically demanding reaction; the conversion requires very high temperature and pressure conditions. There are many ways to overcome those energy barriers and facilitate the conversion process. Those include the use of photocatalysis and the acid-base pair catalysis. The acid-base pair catalysis promotes this reaction and allows it to proceed under mild conditions. In essence, the activation of CO_2 occurs at the base sites; then the nucleophilic substitution causes the ring-opining of epoxide at the acidic cite of the catalyst (Figure 2). An example of the acid-base pair catalysis involves the design of an amine-functionalized catalyst that will be further discussed in Chapter 4.

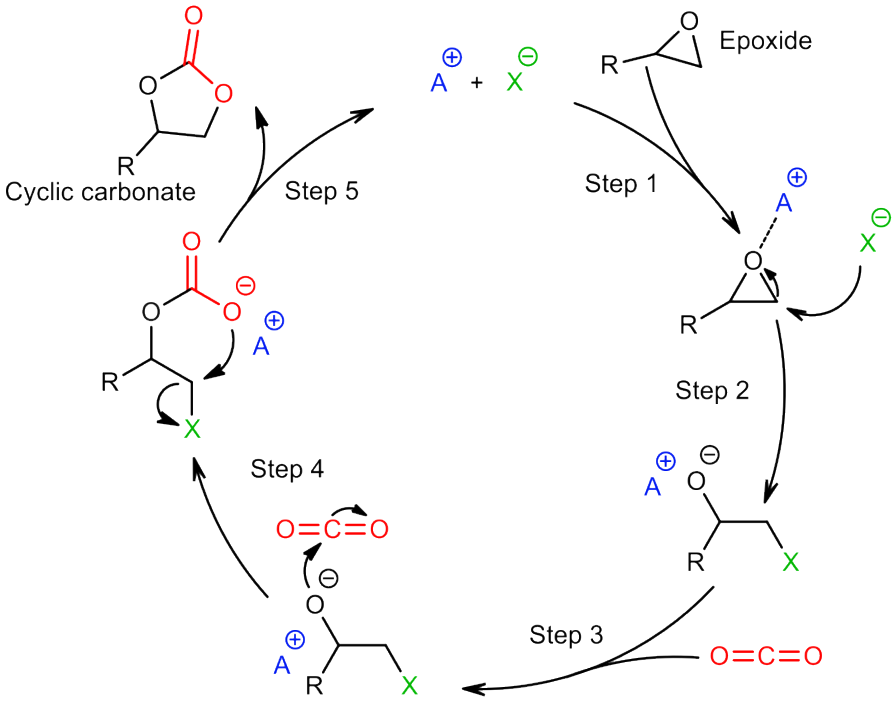

Figure 2: Proposed mechanism the cyclic addition of CO_2 into epoxide to form cyclic carbonate.

1.3 Background on semiconductor photocatalysis

Photocatalysis is a phenomenon where a semiconductor photocatalyst accelerates a kinetically slow photoreaction; reaction that utilizes light.[21,22] Examples of such semiconductor photocatalysts are: TiO_2, ZnS, ZnO, CdS, WO_3, Fe_2O_3 and $BiVO_4$. For a photocatalyst to be an ideal, it should possess the following criteria: I) stability in aqueous/nonaqueous medium under light irradiations, II) suitability for visible and/or near UV light energy harnessing, III) excellent separation of photogenerated charge carriers to prevent fast charge recombination, IV) lack of toxicity V) low production cost VI) adequate surface area and VII) the valance band edge of the photocatalyst should be at potential that is greater than +1.23 V vs. the reversible hydrogen electrode (RHE) for the reaction to be thermodynamically favored, $2H_2O \rightarrow 4H^+ + 4e^- + O_2$, $E° = 1.23$ V vs. SHE.[23,24] Number of photocatalysts of suitable valance band shows low or negligible activity due to the lack of some of the above mentioned criteria.[25] Therefore, the fabrication an effective photocatalyst remains of significant challenge.

Thus far, research has given priority for TiO_2 photocatalyst owing to its outstanding photocatalytic activity.[26] However, TiO_2 suffers from drawbacks that limits its activity under solar irradiation, particularly, utilizing visible light. TiO_2 has a band gap of 3.2 eV that matches absorption in the UV light which composed only 3-5% of the solar spectrum.[27,28] Several techniques have been developed in order to lower the band gap of the photocatalyst, shift the light absorption capability towards visible region, and extend its spectral response to visible light.[29–31] Those include metal[32] and non-metal[33] doping, formation of composite heterojunction of two or more semiconductors.[34] Or the fabrication of semiconductors materials that have more suitable band gap. Particularly, Bi-based mixed transition metal oxides.

1.4 Mixed transition metal oxides

Much research devoted toward multicomponent metal oxides, in particular, mixed transition metal oxides due to their outstanding catalytic,[35] electrochemical,[36] magnetic,[37] electrical,[38] optoelectronic and biomedical properties.[39] Mixed transition metal oxides of the formula ABO_4 (ABO_4; A and B are transition metals such as Bi, V, Co, Ni, Zn, Mn, Fe, Nb, etc.) are the most widely used catalysts for various applications in many fields.[40] For example: selective reduction of CO,[41] water demand remediation,[42] catalysts / co-catalyst in many selective organic transformations,[43] photocatalytic water splitting[44] and SO_2 destruction.[45] Various methods have been investigated for the preparation of ABO_4 mixed transition metal oxides including: sol-gel,[46,47] co-precipitation method,[48] hydrothermal method,[49] mechanochemical synthesis,[50] and using microwave irradiation.[41]

1.5 Overview Bismuth-based mixed metal oxides

Bismuth-based multicomponent metal oxide, $BiMO_4$, especially transition metals have attracted increasing interest owing to their well-defined diverse structures,[51] intrinsic properties[52] and their potential applications.[53] In particular, bismuth vanadate, ($BiVO_4$), attracted increasing interest as ferroelastic material,[54–58] and has been regarded as one of the most promising photocatalyst due to its unique photoelectrochemical properties, and outstanding features such as narrow band gap of ~2.4 eV[59,60] along with an appropriate valance and conduction band alignment that are suitable for water oxidation.[61] $BiVO_4$ exhibits good stability in aqueous media and has low fabrication cost. However, it suffers from some limitations. Theoretically, its activity towards hydrogen conversion is restricted due to the conduction band positioning that is lower than that needed to reduce H^+ to H_2.[62] Synthesis and characterization of $BiVO_4$ achieved a great progress since 1999.[61] $BiVO_4$ exists in three different polymorphs, two of which are not highly photoactive.[63] The three different structure phases are; orthorhombic pucherite, tetragonal dreyerite, and monoclinic clinobisvanite. Monoclinic clinobisvanite of 2.4 eV band gap is the most photoactive.[64]

1.6 Bismuth niobate structure

Among transition metal niobates and with a fine tuned structure, bismuth niobate ($BiNbO_4$), has been reported as a promising microwave dielectric ceramic.[65] The merit of enhanced photocatalytic activities associated with metal niobite is that the energy level of Nb-4d level along with the distorted octahedral (NbO_6) units in the metal niobite lower the band gap of such photocatalysts in such a way that they absorb light in the visible region of the spectrum.[66] Bismuth niobite exists in two polymorphs: orthorhombic (α-$BiNbO_4$), the low-temperature phase, and a triclinic (β-$BiNbO_4$), the high-temperature phase.[67] $BiNbO_4$ was first synthesized by Aurivillius and Arkiv in 1951.[68] In 1962, Roth and Waring demonstrated the formation of the orthorhombic phase at low temperature and claimed the irreversible transformation of the triclinic phase to the orthorhombic phase upon heating at 1293 K, which eventually melts at 1518 K.[69] Further investigations by Diehl and Carpentier in 1973 provided a structural refinement of β-$BiNbO_4$ and revealed similar discoveries that were detailed by Roth and Waring with respect to the irreversibility of the phase transformation from β-$BiNbO_4$ to α-$BiNbO_4$. Moreover, they reported the use of β-$BiNbO_4$ as an antiferroelectric and ferro-elastic materials.[70,71] In 1993, full structural description of $BiNbO_4$ orthorhombic phase was provided by Subramanian and Calabrese.[72] In their report, they describe the growth of α-$BiNbO_4$ particles from BiOF flux at temperature below 1173 K. Furthermore, they attributed the irreversible nature of phase transformation from β-$BiNbO_4$ to α-$BiNbO_4$ to the lattice structure difference between the high-temperature phase and the low-temperature phase.

The transformation of β-$BiNbO_4$ to α-$BiNbO_4$ was first observed in 2007 upon heating the bulk of β-$BiNbO_4$ to a temperature range of 973 K to 1303 K. The transformation was hypothesized to be related to associated activation of stress and heat energy in the heating course. This observation was not observed in powder samples and the cooling course.[73] Zhai et al. reported the co-existence of what is denoted as low-β phase formed below 1023 K as the thermodynamically metastable state of $BiNbO_4$ along with the preformed $Bi_5Nb_3O_{15}$ intermediate phase facilitated by using citrate method in the preparation. The low-β completely transforms into the α-$BiNbO_4$ phase when thermally heated above 1313 K, the α-$BiNbO_4$ transforms into β-$BiNbO_4$ (High-β which formed above 1313 K) again.[74,75]

The formation of both phases of $BiNbO_4$ was investigated systematically over a wide range of temperatures and pressures as a driving force for phase transition (573-2073 K and 0-5 GPa).[76] The solid-state method was adopted for the formation of both β-$BiNbO_4$ and α-$BiNbO_4$ at 1423 K and 1173 K, respectively Figure 3. In their findings, Xu et al. reported that heating the bulk β-$BiNbO_4$ at 1173 K prompts transformation to the α-$BiNbO_4$. Both phases convert to what is denoted as a high-pressure (HP-$BiNbO_4$) metastable phase which occurs at a pressure above 3 GPa and 1073 K. It was found that the temperature requirement to obtain such a phase transformation decreases as the pressure increases.[77,78] Moreover, heating HP-$BiNbO_4$ phase at 101.325 kPa to 1423 K and 873 K converts it back to β-$BiNbO_4$ and α-$BiNbO_4$, respectively.

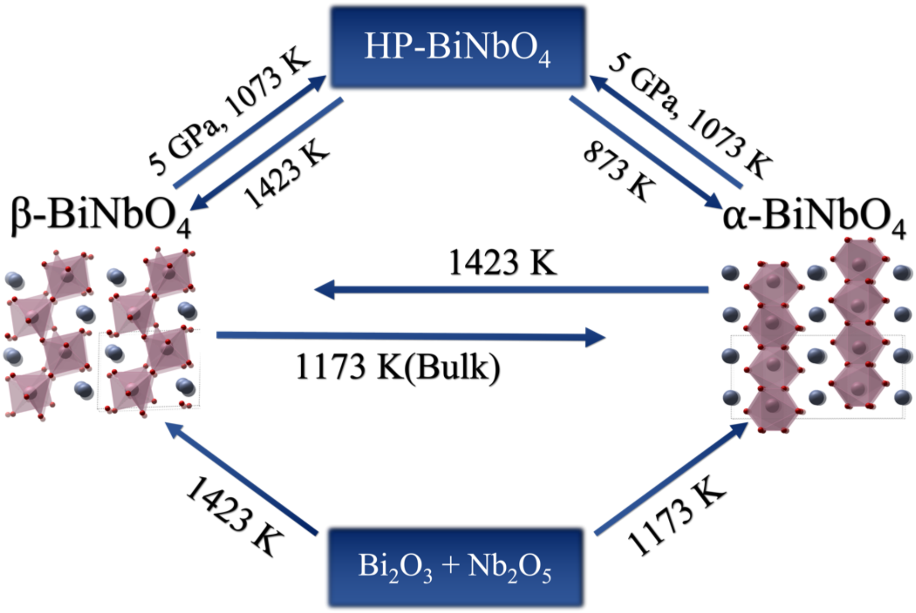

Figure 3: Phase transitions of $BiNbO_4$ at high pressure and high temperature.

To understand the band structures of different phases of $BiNbO_4$, Zou et al. reported the substitution effect of Ta^{5+} by Nb^{5+} on photocatalytic, photophysical, and structural properties of $BiTa_{1-x}Nb_xO_4(0 \leqq x \leqq 1.0)$. In their findings, the orthorhombic exhibits much higher activity than that of triclinic photocatalyst, which is higher than that of the well-known TiO_2.[79] The band structure of $BiNbO_4$ consists of $6s^2$ energy level of Bi^{3+} and the 2p energy level of O^{2-} at the valance band. The d-level of Nb^{5+} lies on the conduction band of $BiNbO_4$. Figure 4 depicts the band structure of $BiNbO_4$, the $6s^2$ level of Bi^{3+} lies just above the 2p level of O^{2-} in the case of β-$BiNbO_4$. Nonetheless, the situation is reversed in the case of α-$BiNbO_4$, in this case the 2p level of O^{2-} lies just above the $6s^2$ level of Bi^{3+}. Distinctive band structures were attributed to the crystal structure of these two phases. The band gap of metal oxides is defined by the oxygen 2p-level and the metal d-level. Hence, the band gap of β-$BiNbO_4$ (high-temperature triclinic phase) is relatively wider than that of α-$BiNbO_4$ (low-temperature orthorhombic phase). Accordingly, α-$BiNbO_4$ is the more efficient visible-light-harvesting phase than the β-$BiNbO_4$ counterpart.[80] This explanation is in agreement with the 1995 article by Wiegel et al.[81]

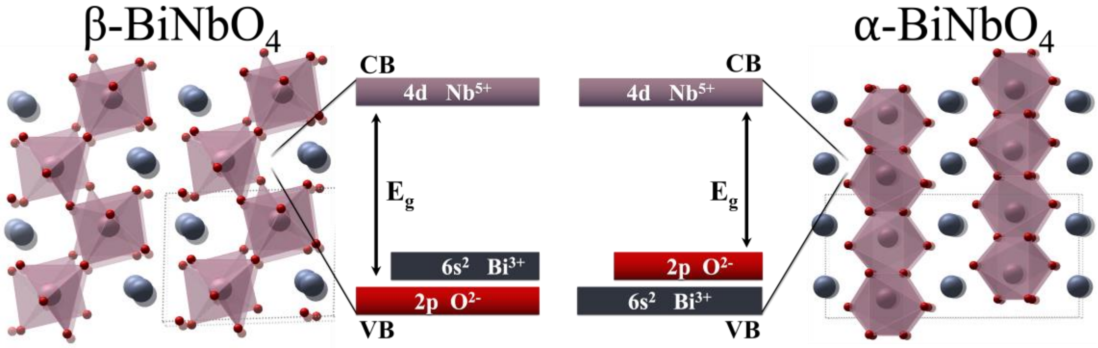

Figure 4: Band structures of both α and β-$BiNbO_4$. α-$BiNbO_4$ has a smaller band gap because the oxygen 2p-level lays above the Bi 6s level, which makes it closer to the 4d energy level of Nb. As for the β-$BiNbO_4$, the oxygen 2p energy level is below the Bi 6s energy level. That explains the difference in the band gap between the two phases. Atom colors: blue: Bi, purple: Nb and red: O.

1.7 Crystal structure of $BiNbO_4$

$BiNbO_4$ has two polymorphous structures: triclinic and orthorhombic. The crystal structures corresponding to the orthorhombic α-$BiNbO_4$ and the triclinic β-$BiNbO_4$ are represented in Figure 5. The difference between the two crystalline structures is due to the arrangement of (NbO_6) polyhedron with respect to the bismuth atoms. In the orthorhombic system, (NbO_6) polyhedron alternate with bismuth atoms in a planar manner,[82] with a relatively large cell volume, (~330 Å^3). Whereas in the triclinic phase, such alternating occurs in a distorted manner,[70] and the cell volume is smaller than that of the orthorhombic system (about 324 Å^3).[83]

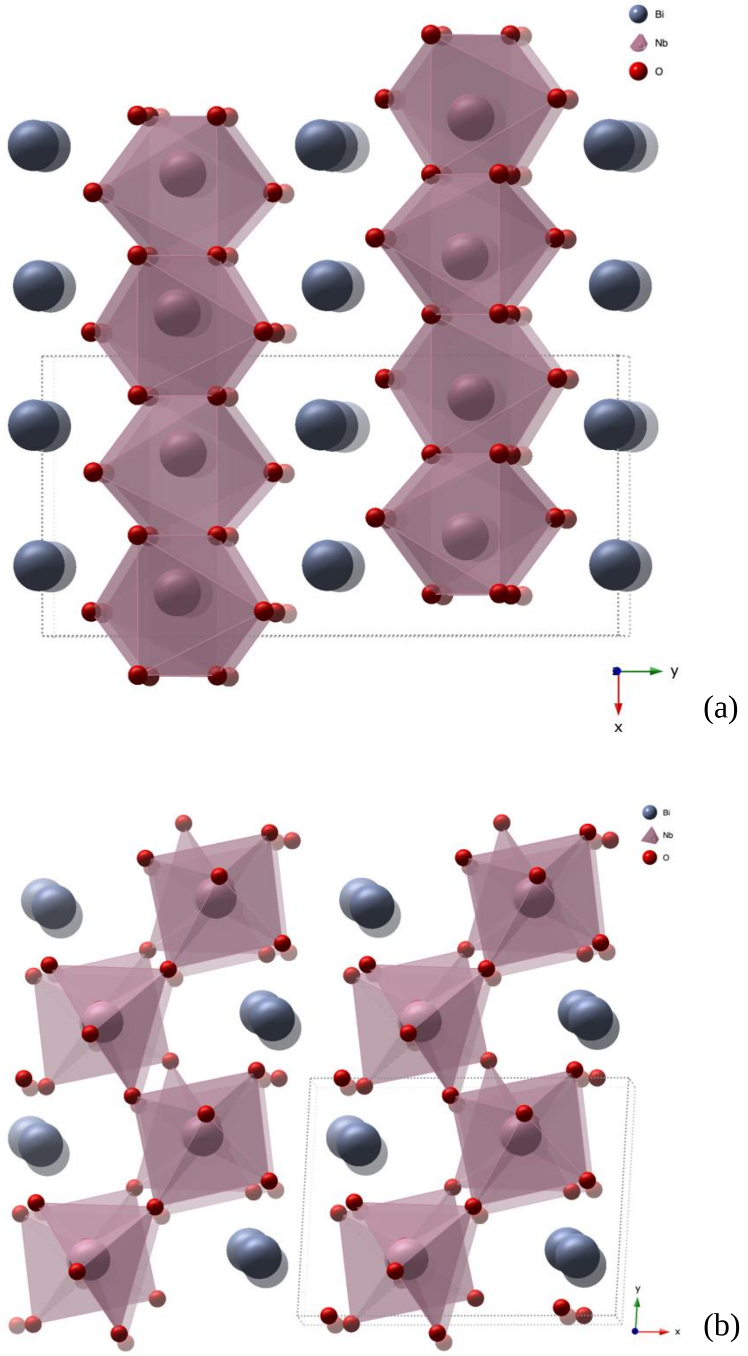

Figure 5: Crystal structure of $BiNbO_4$ phases. Representing the arrangement of (NbO_6) polyhedron with respect to the bismuth atoms, (a) α-$BiNbO_4$ (orthorhombic system, space group P*nna*), (NbO_6) polyhedron alternate with bismuth atoms in a planar manner, (b) β-$BiNbO_4$ (triclinic system, space group P^{-1}), (NbO_6) polyhedron alternate with bismuth atoms in a zig-zag manner. Atom colors: niobium (purple); bismuth (blue) and oxygen (red).

1.8 Band structure of $BiNbO_4$

In spite of the wide variety of mixed metal oxides, still, the fundamental basis of every semiconductor photocatalyst is its property and energy structure. In essence, it is the band position vs. the Standard Hydrogen Electrode (SHE) that underlines the activity of the photocatalyst and the operation of the photochemical system.[84,85] Bismuth oxide Bi_2O_3 has a band gap that is lower than 3.0 eV.[86] In the other hand, nioubium oxide has a very large band gap that is even larger than that of TiO_2.[87–89] In contrast, $BiNbO_4$ has a band gap that is in between the two metal oxides; Bi_2O_3 and Nb_2O_5. The valance band edge of $BiNbO_4$ is higher than those of TiO_2 and $BiVO_4$ Figure 6. Thus, the photocatalytic oxidation capability of $BiNbO_4$ supposed to be higher than that of $BiVO_4$ and TiO_2 which they have almost the same valence band edge potential of 2.9 eV Figure 6.[62] Herein, based on the valence band position, the ability of oxygen evolution should be higher when using $BiNbO_4$ as photocatalyst compared to TiO_2 or $BiVO_4$. However, the conduction band potential of both $BiVO_4$ and $BiNbO_4$ are higher than that needed to reduce H^+ to H_2. Therefore, the applications are limited when it comes to hydrogen evolution.

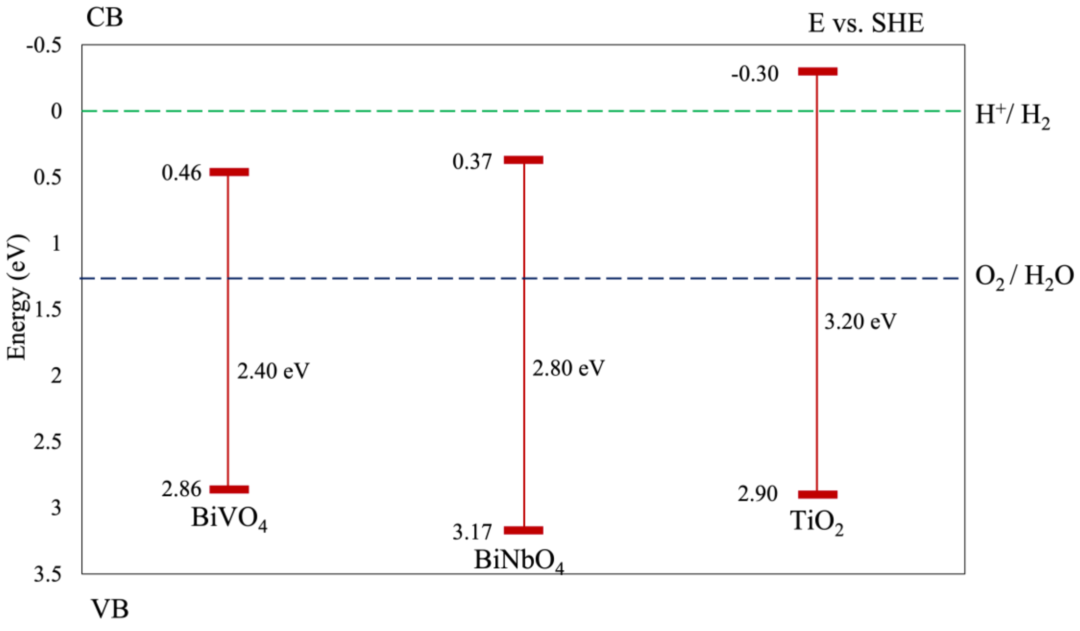

Figure 6: Valence and conduction band positions of $BiNbO_4$, $BiVO_4$ and TiO_2 vs. the standard hydrogen electrode (SHE).

1.9 $BiNbO_4$/r-GO nanocomposite

The fabrication of semiconductor material with a small band gap that harvest visible light comes with a price. Due to the small energy difference between the valance and the conduction band, the photo-induced polarity that is necessary for the photoreaction to proceed tends to annihilate by a process called recombination of electron hole pairs. The exited electrons fall back to the energy level that is associated with the generated positive hole. Eventually, both charge carriers disappear in the process and the redox reaction associated with the charge separation stops accordingly. This serious drawback can be enhanced by using electron scavenger materials such as reduced graphene oxide (r-GO) which suppress charge recombination.[90] $BiNbO_4$-r-GO nanocomposite will be further discussed in (Chapter 3).

1.10 Isoreticular functionalized (MOFs) for CO_2 utilization

It has been generally acknowledged that Metal Organic Frameworks, MOFs, are porous highly crystalline materials with a remarkably high surface area. Those materials are assembled by the coordination of metal ions by organic linkers.[91] MOFs exhibit their unique features, that include their defined crystal structures and net system, high surface area, and tunable pore structures.[92,93] These features make them potential materials for various applications. Nonetheless, MOFs suffer from considerable drawbacks, such as poor chemical, and thermal stability and electrical conductivity, deter this materials from exhibiting full potential for real practical applications.[94–98] Therefore, it is of a great interest to further enhance the functionality of MOFs. The challenge of designing an effective photocatalyst for carbon dioxide utilization lies in the fact that the photocatalytic system should provide high activity, selectivity and efficiency at the same time. Particularly, Ti^{IV}-MOFs combine the efficient photocatalytic activity of titanium oxide and the light harvesting nature of organic linkers. For instance, MIL-125 is a promising photocatalyst with a band edge of 3.6 eV that makes it a UV active material.[99] However, it would be more efficient to use material that are active in the visible region of the spectrum to efficiently utilizes more of the solar light. Accordingly, toward tuning the optical response of such active material, an iso-reticular amine functionalized analogue, denoted as NH_2-MIL-125 Figure 7, was synthesized. NH_2-MIL-125 experience a band gap of 2.6 eV which makes it a visible light active material.[100] It has been acknowledged that the amine functionalized MOF achieved higher photocatalytic activity toward CO_2 utilization under visible light irradiation.[101] Notably, activated NH_2-MIL-125(Ti) has a large surface area of 1492 $m^2\,g^{-1}$ with a pore volume of 0.66 $cm^3\,g^{-1}$. CO_2 adsorption uptake capacity of NH_2-MIL-125(Ti) can go up to176 mg g^{-1} at 273 K, which is relatively higher than that of MOF-5 and MOF-177 at 1 atm CO_2 pressure conditions. The high capacity was attributed to the smaller micropores of NH_2-MIL-125(Ti) (ca. 6Å) compared to MOF-177 (ca. 11Å) and MOF-5 (ca. 12Å), which can promote stronger van der Waals interaction with carbon dioxide molecules (ca. 3.3Å).[102]

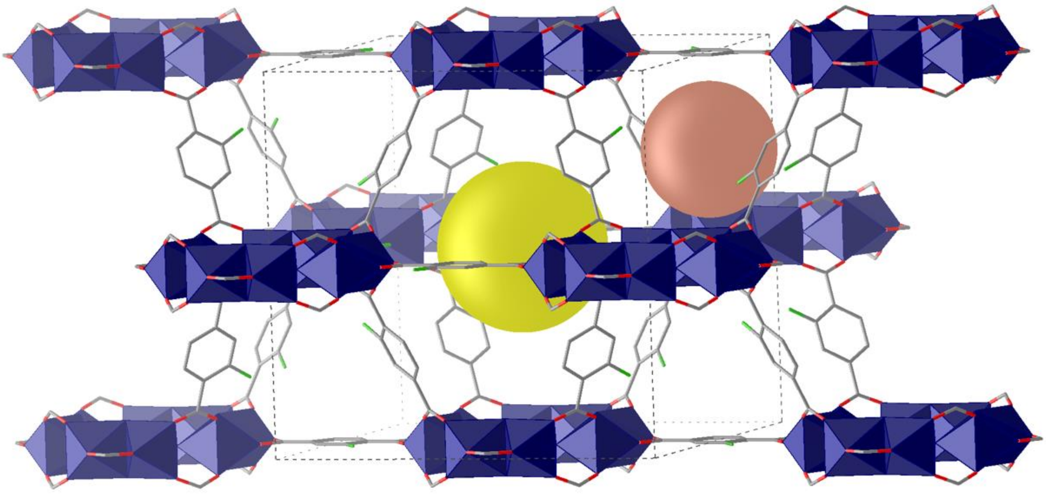

Figure 7: A schematic structure of NH_2-MIL-125. Atom colors: Ti (blue); C (gray); N (green) and O (red). H atoms were omitted for clarity.

1.11 Aim of the thesis

This introduction mainly attempts to summarize the recent progress in designing $BiNbO_4$, an alternative for TiO_2 and $BiVO_4$ photocatalysts. The work done in this area is relatively limited and systematic study (of preparation) has not been done yet. In this work, $BiNbO_4$ was prepared using three different synthetic routes: co-precipitation, hydrothermal and citrate, under various pH values: 2, 7 and 10 with the objective to study the effect of pH and reaction conditions on phase polymorphism of $BiNbO_4$. Moreover, investigation the activity of $BiNbO_4$/r-GO and $BiNbO_4$/NH_2-MIL-125(Ti) nanocomposites upon the cycloaddition of CO_2 with propylene carbonate to form cyclic propylene carbonate under visible light irradiation.

Chapter 2: $BiNbO_4$ Prepared Using Different Routes

2.1 Introduction

Semiconductor photocatalyst has been prepared using different methodologies including solid-state, coprecipitation, citrate sol-gel and hydrothermal methods. The first attempts to prepare $BiNbO_4$ was utilizing solid-state method. This method involves mixing the starting materials and heating the mixture at elevated temperature to obtain the desired solid product.[103] Operating at high temperature results in an agglomerated product with relatively low surface area and poor catalytic activity. However, it was not until recently when the solution-based techniques were developed to open the possibility of having control over the porosity, particle size, surface area and even the shape of the particles.

The most convenient method to prepare solid state catalyst is the coprecipitation method. It is a typical solution-based technique as it is usually carried out in an aqueous medium where the product precipitates out right after mixing the solutions of the starting precursors. This method is convenient because it is quick, easy and doesn't require costly setup or harsh conditions.[104] The method provides a better control over stoichiometry and purity of prepared sample and it requires lower calcination temperature.[105] The conventional Co-precipitate method is cost-effective and has different advantages regarding particle size and surface area.[106,107]

Hydrothermal synthesis utilizes solvents and applying high pressure and temperature conditions that is above the critical point of the solvent. Where the solubility of reactants tends to increase upon increasing the pressure and temperature which results in speeding up the reaction.[108] Comparing to other synthetic methods, hydrothermal method allows product formation at relatively low temperature.[109] Disadvantages of this technique includes the need for autoclaves and the inability to have control over the size and the shape of products.[110]

In 1967, Pechini developed a sol–gel method to prepare materials that have an unfavorable hydrolysis equilibrium. Such materials includes alkaline-earth niobates and titanates.[111] This method was named after him as a Pechini method or liquid-mix process. It was not until 1970s when Anderson popularized this approach to synthesis perovskite powders.[112]

Calcination temperature has a considerable impact on the crystallinity and the characteristic of the products to be obtained. Such characteristics include the particle size, porosity, surface area, impurity content and the crystal growth which affect the lattice phase and parameters.[72,77,113–115] Crystallinity in particular has a significant impact on charge separation efficiency of the photocatalyst.[116,117] Thus, calcination temperature has to be controlled carefully. The pH has a considerable effect on surface topography, morphology, grain size which all have a significant impact on the photocatalytic performance.[118]

2.2 Research design and methodology

$BiNbO_4$ mixed phase was studied using three distinctive synthetic routes: co-precipitation, hydrothermal, and citrate precursor methods Figure 8. Moreover, the effect of pH, surfactant, and temperature on the phase polymorphism and band gaps properties of prepared $BiNbO_4$ nanoparticles was investigated.

2.2.1 Materials

Bismuth (III) Nitrate pentahydrate ($Bi(NO_3)_3{\cdot}5H_2O$), Bismuth (III) Citrate ($[O_2CCH_2C(OH)(CO_2)CH_2CO_2]Bi$, 99.99%), Ammonium Niobate (V) Oxalate hydrate ($C_4H_4NNbO_9{\cdot}xH_2O$, 99.99%), Acetic Acid (CH_3COOH, 99.7%), Hydrochloric Acid (HCl, 37%), Ammonium Hydroxide (NH_4OH, ≥99%), Ethylene Glycol ($HOCH_2CH_2OH$, ≥99.5%), Sodium Dodecyl Sulfate ($CH_3(CH_2)_{11}OSO_3Na$, ≥98.5%) and Polyethylene Glycol average M_n 400 (PEG-400) were purchased from Sigma Aldrich and used as received without further purification. Aqueous solutions were prepared using doubly distilled water passed through a Millipore Milli-Q® integral 15 water purification system. All Samples calcined using carbolite ELF type 201 furnace open to atmosphere.

2.2.2 Preparation of mixed-phase $BiNbO_4$ photocatalyst

Co-precipitation method: A series of $BiNbO_4$ nanoparticles were prepared by co-precipitation method using bismuth nitrate pentahydrate, and ammonium niobate (V) oxalate hydrate as starting materials, with a stoichiometric proportion of 1:1, $Bi(NO_3)_3{\cdot}5H_2O:C_4H_4NNbO_9{\cdot}xH_2O$. In a typical synthesis, 5 g of $Bi(NO_3)_3{\cdot}5H_2O$ was dissolved in 100 mL 4 M acetic acid under mild heating for complete dissolution (bismuth solution). $C_4H_4NNbO_9{\cdot}xH_2O$ was dissolved in 75 mL deionized water (niobium solution). Bismuth solution was added to the niobium solution, the two solutions were mixed and kept under constant stirring using Witeg MSH-20D speed adjusted at 300 RPM. Then, acetic acid (CH_3COOH) or ammonium hydroxide (NH_4OH) was used to adjust the pH values to 2, 7, and 10, respectively. The obtained white colloidal solution was left under constant stirring for 24 h followed by evaporating the excess solvent. Finally, the obtained powder was dried, calcined at

1023 K and 1173 K respectively for 6 h. When surfactant was used, it was added to the niobium solution before being added to the bismuth solution at the following Mol % i.e. (3% SDS, 10% EG, 10% PEG).

Hydrothermal method: Same as above-mentioned procedure was implemented for synthesis of $BiNbO_4$ using hydrothermal method. However, the colloidal solution was transferred into high-pressure Parr reactor model 4848 equipped with turbine type impellers, speed adjusted at 300 RPM at 493 K for 24 h. The obtained powder was dried by evaporating the excess solvent and calcined at 1023 K for 6 h.

Citrate precursor method: $BiNbO_4$ nanoparticles was prepared by citrate method using bismuth (III) citrate, and ammonium niobate (V) oxalate hydrate as starting materials, with a stoichiometric proportion of 1:1, Bi^{3+}: Nb^{5+}. In a typical synthesis, 5 g of bismuth (III) citrate was dissolved in 100 mL deionized water. ammonium niobate (V) oxalate hydrate was dissolved in 75 mL deionized water. The two solutions were mixed and kept stirring. Amount of concentrated nitric acid or ammonium hydroxide was used to adjust the pH values to 2, 7, and 10, respectively. The obtained white gel was aged for 24 h followed by evaporating the excess solvent. Finally, the obtained powder was calcined at 1023 K for 6 h. Figure 8 represents detailed synthetic steps for each method used in this study.

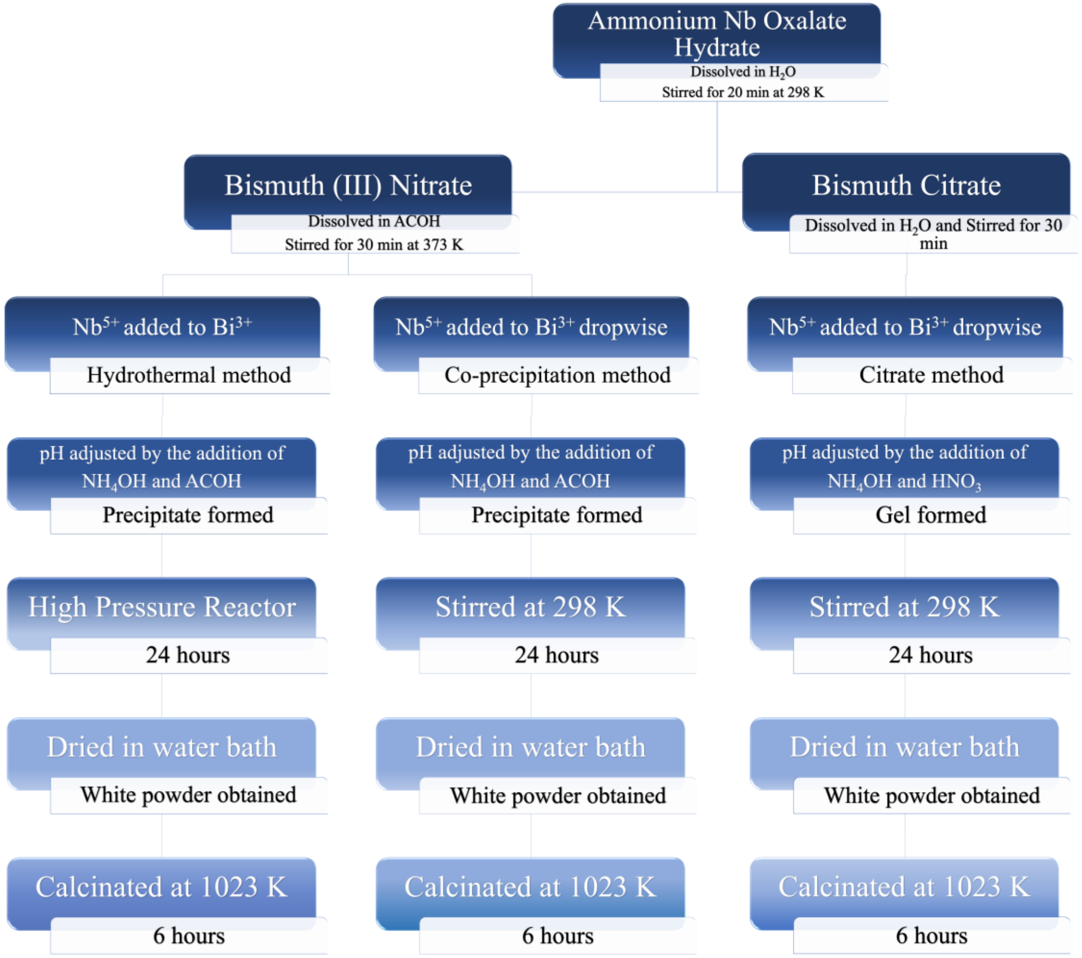

Figure 8: Detailed synthetic steps for each method used in this study.

2.3 Characterization of the photocatalysts

This section provides a detailed investigation of the analytical methods and techniques used to characterize structure and properties of the obtained photocatalysts. Such investigation considers structural, optical, morphological and elemental analysis of the as synthesized photocatalysts with the aim of determining their ability to undergo light driven photocatalytic transformations.

2.3.1 Powder X-ray diffraction (PXRD)

The crystalline phase of the prepared $BiNbO_4$ solid was investigated using Shimadzu-6100 powder XRD diffractometer equipped with Cu-Kα radiation tube operated at 40 kV and 30 mA over the 2θ range of 10°-75° at a rate of 2 deg/min where $\lambda = 1.542$ Å. The PXRD pattern of $BiNbO_4$ was analyzed and confirmed based on the standard PXRD database card (ICDD, 2018). Figure 9 (I) illustrates the PXRD patterns of $BiNbO_4$ synthesized using co-precipitation method at different pH values and calcined at 1023 K for 6 hours. The diffraction peaks assigned by the letters O, T and N correspond to α-$BiNbO_4$, β-$BiNbO_4$ and Nb_2O_5 respectively. Based on the obtained PXRD data, the lattice exhibits α to β phase transformation upon increasing the pH, PXRD patterns were correlated to the crystallographic information data base (PDF-00-016-0295) and (PDF 00-016-0486). Figure 9 (I) illustrates the PXRD pattern of the photocatalyst prepared at pH 2 using co-precipitation method, as shown the majority of the PXRD peaks including the main peak corresponding to (hkl) of (121) plane at $2\theta = 28.3$ are readily indexed to α-$BiNbO_4$ orthorhombic phase, space group: *Pnna*. In contrast, peaks at $2\theta = 29.5$, 34.2 and 46.9 could be assigned to β-$BiNbO_4$ triclinic phase despite the fact it is rather weak. Calculated cell parameters from PXRD data of α-$BiNbO_4$ are as follows: a= 4.99 Å, b=11.70 Å, c=5.69 Å, these results are in good agreement that reported previously in the literature.[119] PXRD pattern of photocatalyst prepared at pH 7 using co-precipitation method, demonstrates the co-existence of both orthorhombic and triclinic phases Figure 9 (I). Based on calculated Reference Intensity Ratio (RIR),[120] 50.23% of the obtained powder present is mainly the β-$BiNbO_4$ i.e. the triclinic phase. Moreover, the PXRD pattern shows a gradual 0.1° shift for the peak towards a higher scattering angles which can be attributed to the tensile stress within the crystal that causes the lattice elongation.[121] Figure 9 (I) shows the PXRD pattern of the photocatalysts prepared at pH 10 using co-precipitation method. Based on the pattern obtained, the diffraction peaks of the β-$BiNbO_4$ phase are more pronounced, based on the reference intensity ratio, 82% of the obtained powder is present as β-$BiNbO_4$. At this point, it is tempting to say as the pH increase the β-$BiNbO_4$ becoming more dominant. Figure 9 (III) shows the PXRD patterns of photocatalyst prepared using hydrothermal assisted solid-state approach at different pH values and calcined at 1023 K for 6 hours. Figure 9 (III) indicates that photocatalyst prepared at pH 2 shows dominantly α-$BiNbO_4$ phase. Nonetheless, as pH increases the dominant phase becomes the triclinic β-$BiNbO_4$ phase. Figure 9 (IV) shows the PXRD patterns of prepared photocatalysts using citrate precursor method at different pH values and calcined at 1023 K for 6 hours. The co-existence of both α-$BiNbO_4$ and β-$BiNbO_4$ form is obvious at pH 2 and pH 10 as shown in Figure 9 (IV). On the other hand, at pH 7 α-$BiNbO_4$ is more pronounced. Moreover, there is an individual niobium oxide present along the obtained product Figure 9 (IV). Figure 9 (II) shows the PXRD patterns of the prepared photocatalysts using co-precipitation method at pH 2 and calcined at 1023 K with different surfactant added. Both phases are co-exist however as indicated from DRS calculation, the α phase is the dominant when using EG and SDS as surfactant, Figure 9 (II) and Table 4.

Figures 9 (V, VI and VII) illustrate the PXRD patterns of photocatalysts prepared using co-precipitation method at different pH values and calcined at 1023 K and 1173 K for 6 hours. As shown, there is a gradual disappearance to the peaks correspond to the α-$BiNbO_4$ upon increasing calcination temperature (1023 K to 1173 K) of the prepared photocatalyst at pH 2 and pH 10. Moreover, ~ 0.1°- 0.2° shift of peaks towards higher angle was observed upon increasing the calcination temperature, which can be attributed to the tensile stress within the crystal lattice. On the other hand, there is a 0.1° shift in the PXRD pattern towards lower scattering angels upon increasing the temperature of the prepared photocatalysts at pH 7 as shown in Figure 9 (VI). This shift can be attributed to the compressive stress within the crystalline lattice. Subsequently, when compared to the photocatalyst calcined at 1023 K, the volume and the lattice parameters were increased upon increasing the temperature of samples prepared at pH 7 and decreased upon increasing the temperature for samples prepared at pH 2 and pH 10. The average particle size was calculated using Debye–Scherrer equation considering the broadening of the main peak at each case, calculated results are tabulated in Tables 1-5.

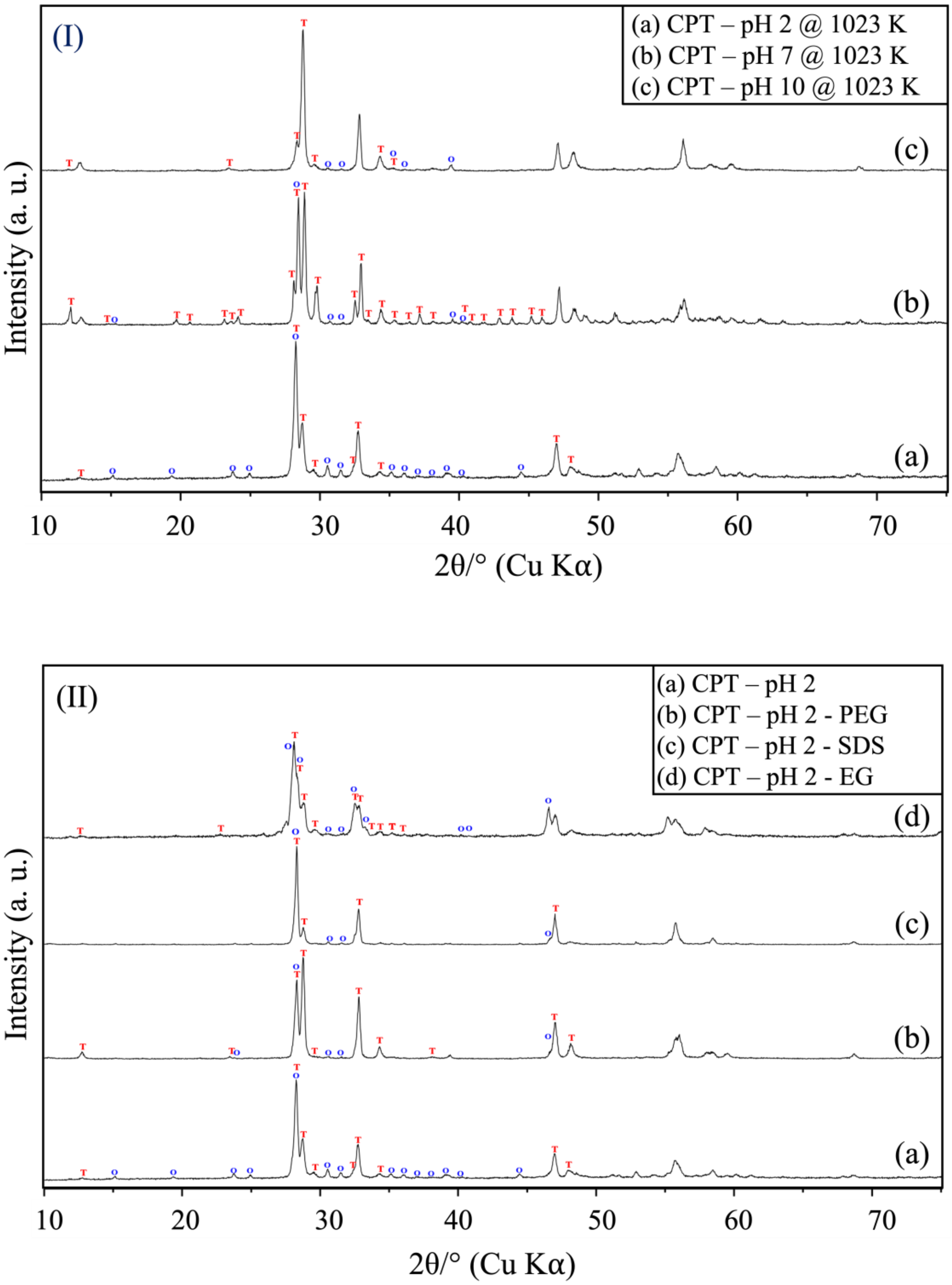

Figure 9: PXRD patterns of $BiNbO_4$. (I) Co-precipitation. (a) pH 2, (b) pH 7, (c) pH 10; (II) pH 2, calcined at 1023 K: (a) no surfactant, (b) polyethylene glycol (PEG), (c) sodium dodecyl sulfate (SDS), (d) ethylene glycol (EG); (III) Hydrothermal: (a) pH 2, (b) pH 7, (c) pH 10; (IV) Citrate precursor: (a) pH 2, (b) pH 7, (c) pH 10; (V) Co-precipitation, calcined at 1023 K and 1173 K at pH 2; (VI) Co-precipitation, calcined at 1023 K and 1173 K at pH 7; (VII) Co-precipitation, calcined at 1023 K and 1173 K at pH 10. The diffraction peaks assigned by the letters O, T and N are correspond to α-$BiNbO_4$, β-$BiNbO_4$ and Nb_2O_5, respectively.

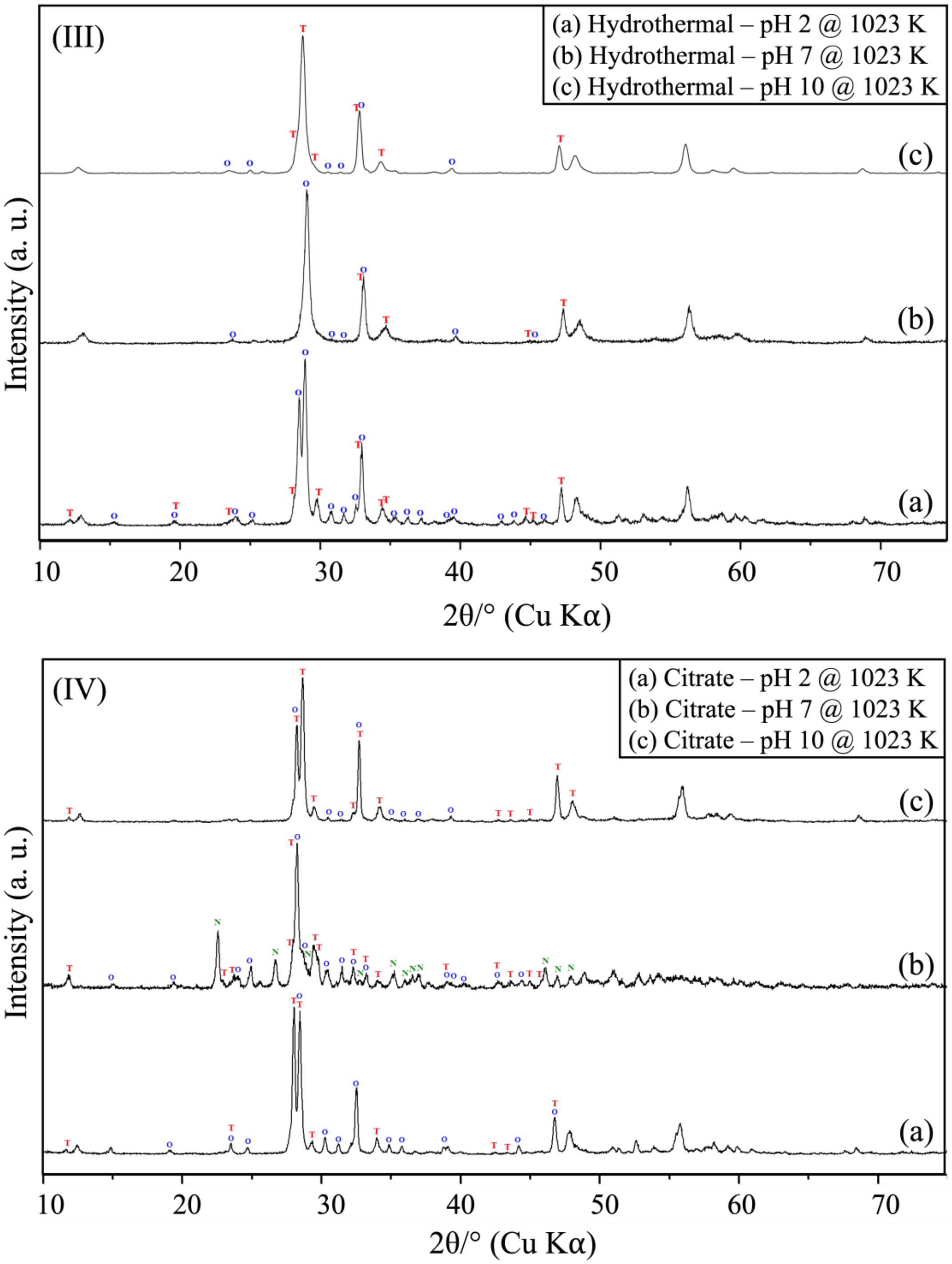

Figure 9: PXRD patterns of $BiNbO_4$: (I) Co-precipitation. (a) pH 2, (b) pH 7, (c) pH 10; (II) pH 2, calcined at 1023 K: (a) no surfactant, (b) polyethylene glycol (PEG), (c) sodium dodecyl sulfate (SDS), (d) ethylene glycol (EG); (III) Hydrothermal: (a) pH 2, (b) pH 7, (c) pH 10; (IV) Citrate precursor: (a) pH 2, (b) pH 7, (c) pH 10; (V) Co-precipitation, calcined at 1023 K and 1173 K at pH 2; (VI) Co-precipitation, calcined at 1023 K and 1173 K at pH 7; (VII) Co-precipitation, calcined at 1023 K and 1173 K at pH 10. The diffraction peaks assigned by the letters O, T and N are correspond to α-$BiNbO_4$, β-$BiNbO_4$ and Nb_2O_5, respectively (continued).

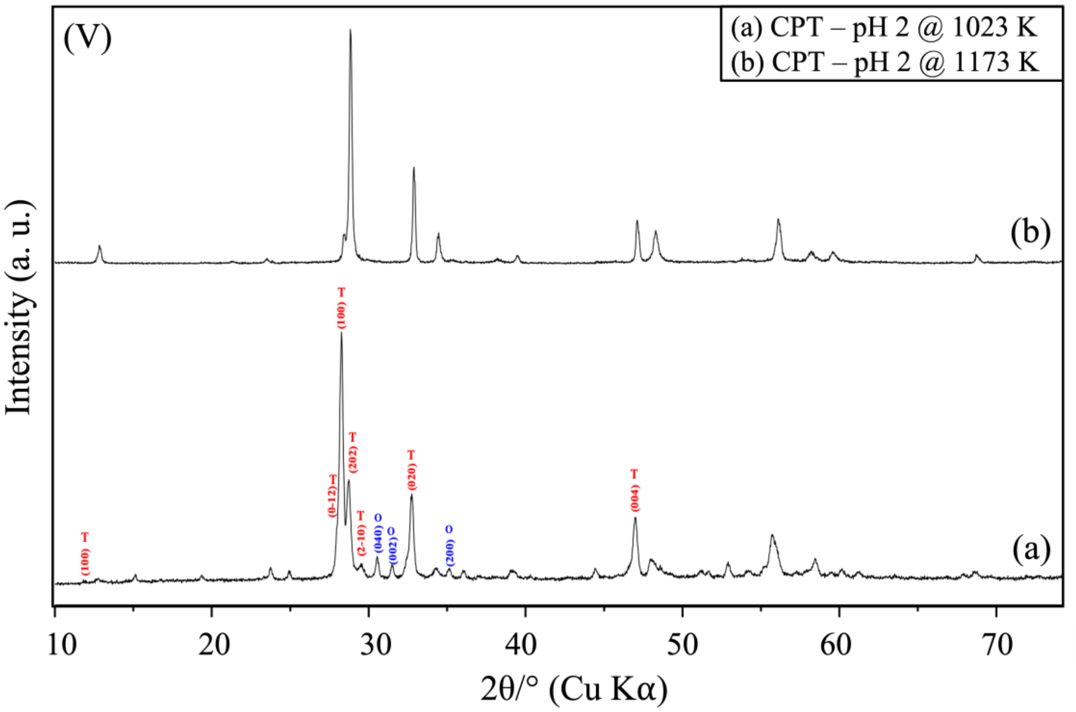

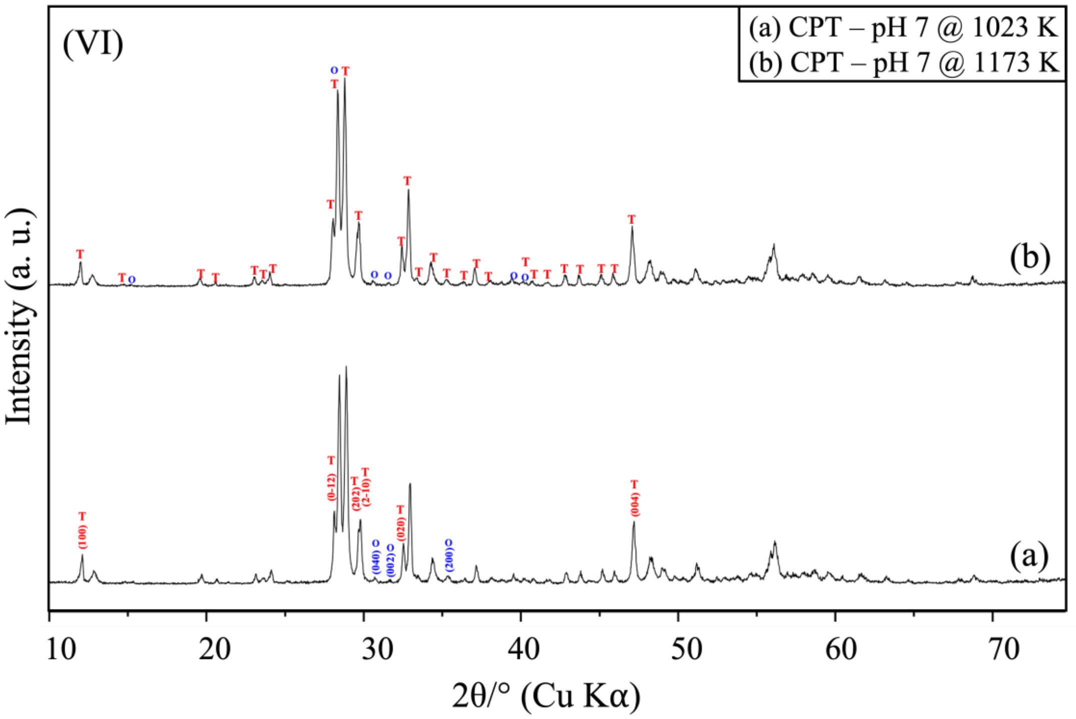

Figure 9: PXRD patterns of $BiNbO_4$: (I) Co-precipitation. (a) pH 2, (b) pH 7, (c) pH 10; (II) pH 2, calcined at 1023 K: (a) no surfactant, (b) polyethylene glycol (PEG), (c) sodium dodecyl sulfate (SDS), (d) ethylene glycol (EG); (III) Hydrothermal: (a) pH 2, (b) pH 7, (c) pH 10; (IV) Citrate precursor: (a) pH 2, (b) pH 7, (c) pH 10; (V) Co-precipitation, calcined at 1023 K and 1173 K at pH 2; (VI) Co-precipitation, calcined at 1023 K and 1173 K at pH 7; (VII) Co-precipitation, calcined at 1023 K and 1173 K at pH 10. The diffraction peaks assigned by the letters O, T and N are correspond to α-$BiNbO_4$, β-$BiNbO_4$ and Nb_2O_5, respectively (continued).

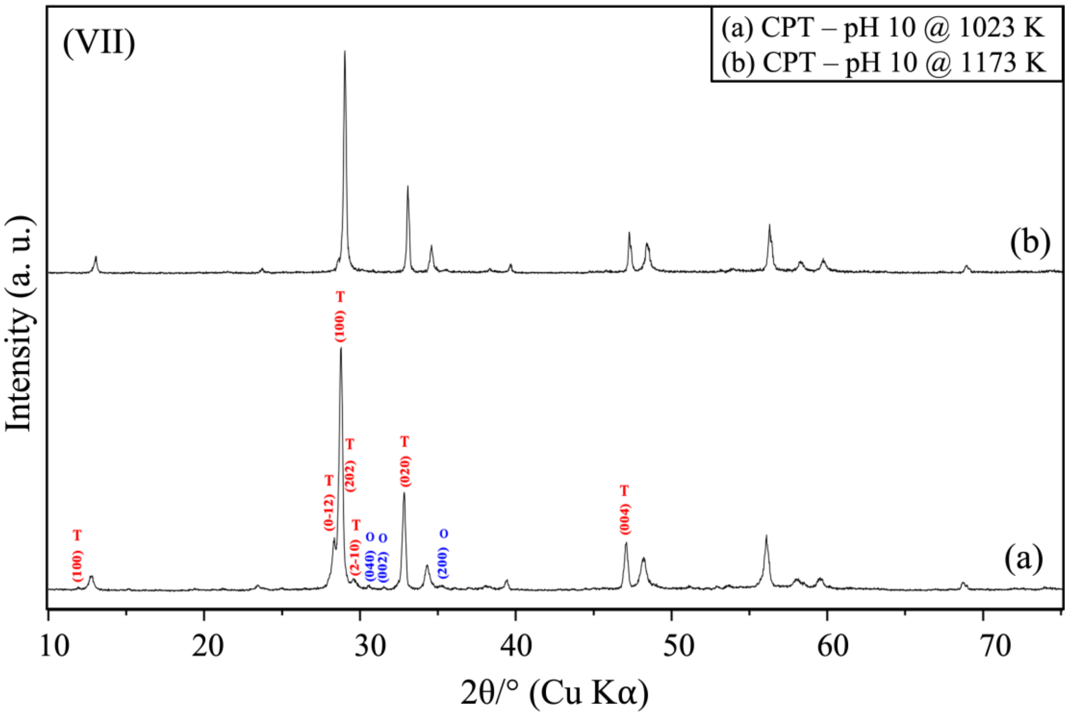

Figure 9: PXRD patterns of $BiNbO_4$: (I) Co-precipitation. (a) pH 2, (b) pH 7, (c) pH 10; (II) pH 2, calcined at 1023 K: (a) no surfactant, (b) polyethylene glycol (PEG), (c) sodium dodecyl sulfate (SDS), (d) ethylene glycol (EG); (III) Hydrothermal: (a) pH 2, (b) pH 7, (c) pH 10; (IV) Citrate precursor: (a) pH 2, (b) pH 7, (c) pH 10; (V) Co-precipitation, calcined at 1023 K and 1173 K at pH 2; (VI) Co-precipitation, calcined at 1023 K and 1173 K at pH 7; (VII) Co-precipitation, calcined at 1023 K and 1173 K at pH 10. The diffraction peaks assigned by the letters O, T and N are correspond to α-$BiNbO_4$, β-$BiNbO_4$ and Nb_2O_5, respectively (continued).

2.3.2 UV-Vis diffuse reflectance spectroscopy (UV-Vis DRS)

Diffused reflectance spectra were obtained using Shimadzu UV-3600 UV-Vis spectrophotometer and recorded in the range from 200 nm to 800 nm. High purity barium sulfate ($BaSO_4$) used as a standard for baseline correction. The output spectrum shows relation between the intensity of light reflected versus the wavelength. The band gap energies were calculated using the results obtained from the DRS spectra using Tauc plot method.[122] The band gap was calculated considering that these photocatalysts were direct semiconductors and using equation (1).

$$(\alpha\ h\nu)^{1/2}=A(h\nu-E_g) \qquad (1)$$

Where α is the absorptivity coefficient, and hv is the energy of the applied incident light in electron volt, n depends on the nature of transition, for direct allowed transition, the value for n is ½, A is a proportionality.[123] The value of E_g can be estimated by extrapolating the linear fit of a plot of $(\alpha hv)^{1/n}$ vs. (hv), Figure 10.

Tauc plot of prepared photocatalyst using co-precipitation method at pH 2 and calcined at 1023 K Figure 10 (a), photocatalyst prepared at such condition was found to have the narrowest band gap of 2.8 eV. Nevertheless, photocatalysts prepared at higher pH used in this study were found to have relatively larger band gap (> 3.2 eV) i.e. capable of harvesting UV light. UV-Vis DRS measurements confirm the dominance of α-$BiNbO_4$ phase at pH 2 whereas β-$BiNbO_4$ dominant at pH 7 and pH 10 respectively which is also in a good agreement with the PXRD results Figure 9.

With respect to the photocatalysts prepared using hydrothermal assisted solid-state approach Figure 10 (b), the narrowest band gap of 3.26 eV is corresponding to photocatalyst prepared at pH 2. Therefore, it's tempting to assume that all samples prepared by hydrothermal assisted solid-state approach can only harvest UV light. Though, from PXRD argument it is concluded that α-$BiNbO_4$ is the dominant phase at pH 2.

Figure 10 (c) represents band gaps of photocatalysts prepared by citrate precursor method. The narrowest band gap of 2.69 eV is related to the α-$BiNbO_4$ prepared at pH 7, this was further confirmed by the PXRD shown in Figure 9 (IV). Whereas, photocatalysts prepared at pH 2 and pH 10 show absorbance at lower wavelength i.e. in the UV region of the spectrum. When ethylene glycol is used as a surfactant, significant shift of absorption band towards the visible region for the photocatalyst prepared at pH 2 occurred i.e. a red shift of 34.06 nm. On the other hand, when polyethylene glycol (PEG-400) is used as a surfactant, a blue shift of 67 nm in the ban gap energy was observed indicating a dominant β-$BiNbO_4$ phase is present. Moreover, when using SDS as a surfactant, a red shift of 4.8 nm was observed. Tauc plots Figure 10 (d).

Figure 10 (e, f and g) shows Tauc plots for the direct allowed transition of $BiNbO_4$ calcined at 1023 K and 1173 K synthesized using coprecipitation method at different pH values. Increasing the calcination temperature from 1023 K to 1173 K caused a significant shift of absorption band towards UV region that reveals the role of temperature on phase transition of orthorhombic of $BiNbO_4$ to the triclinic. Moreover, this observation is further supported using PXRD data shown in Figure 9.

The band position of crystalline materials is affected by the crystalline structure, more specifically, the lattice volume. Decreasing lattice constant will decrease the interatomic distance, which in turn, increase the binding energy of the valence electrons to the parent atom. Therefore, more energy is needed to excite the electrons to the conduction band. The crystal structures corresponding to the orthorhombic α-$BiNbO_4$ and the triclinic β-$BiNbO_4$ are represented in Figure 5, (Chapter 1). The difference between the two crystalline structures is due to the arrangement of (NbO_6) polyhedron with respect to the bismuth atoms. In the orthorhombic system, (NbO_6) polyhedron alternate with bismuth atoms in a planar manner,[82] with a relatively large cell volume, (~330 Å^3). Whereas in the triclinic phase, such alternating occur in a distorted manner,[70] and the cell volume is smaller than that of the orthorhombic system (about 324 Å^3).[83]

Based on the findings, there is a direct correlation between band gap of prepared photocatalysts and lattice volume; as the lattice volume increases the band gap decreases. As an example, in Table 1; photocatalyst prepared under coprecipitation method at pH 2 shows coexistence of both phases with a major rhombic phase of ~70% in the mixture with lattice volume of 332.1 Å^3 which led to a smaller band gap of 2.8 eV. On the other hand, as Table 2 shows when comparing photocatalysts prepared under hydrothermal method at pH 7 and 10, band gap increased to 3.43 eV with majority of triclinic phase present. The wider band gap can be attributed to the lower crystal volume of 265.64 Å^3 and 274.79 Å^3 respectively. All discussion above can be applied systematically to all prepared photocatalyst with consisting trend across the board.

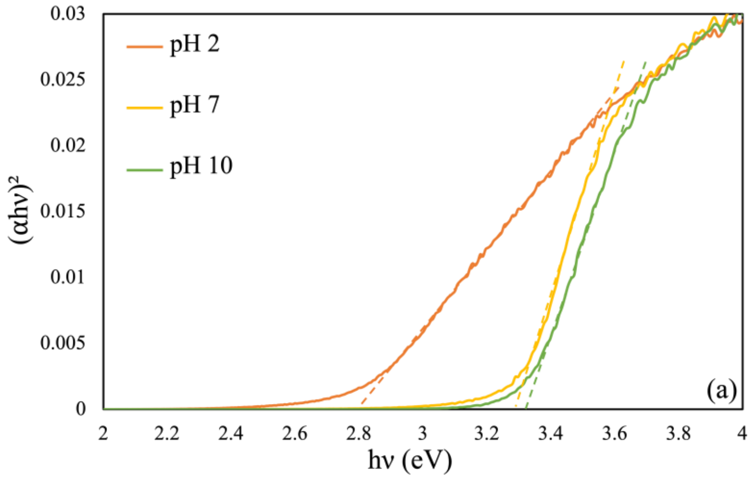

Figure 10: Tauc plots of directly allowed transition of $BiNbO_4$. (a) Co-precipitation; (b) Hydrothermal; (c) Citrate method; (d) Co-precipitation at pH 2; (e, f, and g) Co-precipitation calcined at 1023 K and 1173 K at pH 2, pH 7, and pH 10, respectively.

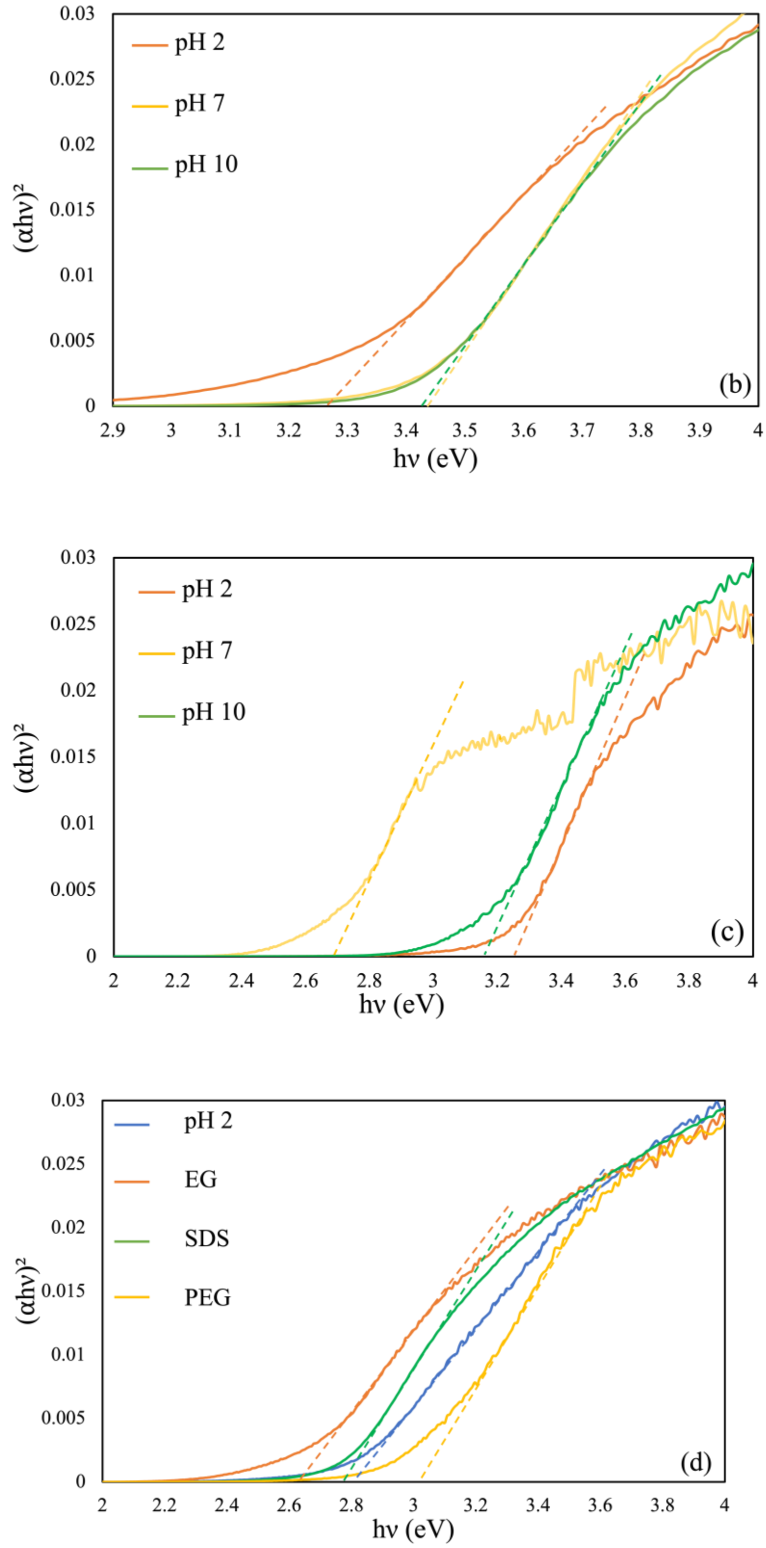

Figure 10: Tauc plots of directly allowed transition of $BiNbO_4$. (a) Co-precipitation; (b) Hydrothermal; (c) Citrate method; (d) Co-precipitation at pH 2; (e, f, and g) Co-precipitation calcined at 1023 K and 1173 K at pH 2, pH 7, and pH 10, respectively (continued).

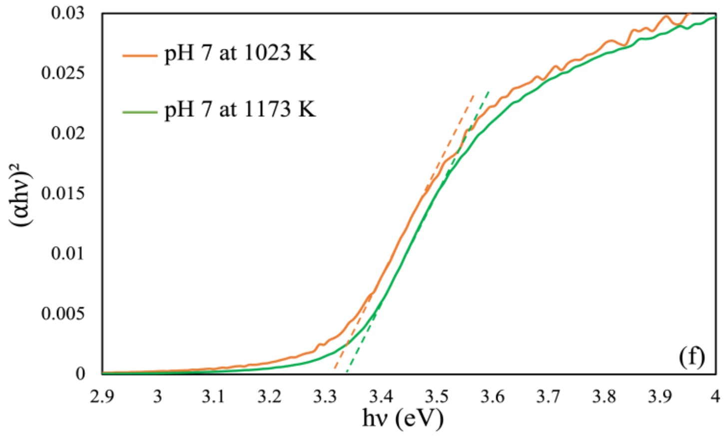

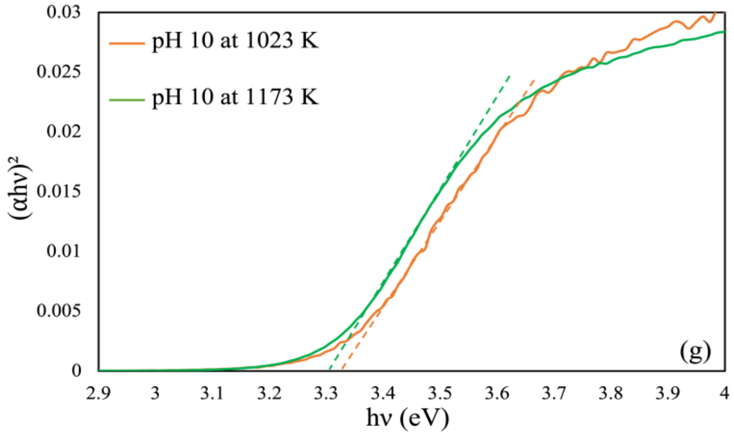

Figure 10: Tauc plots of directly allowed transition of $BiNbO_4$. (a) Co-precipitation; (b) Hydrothermal; (c) Citrate method; (d) Co-precipitation at pH 2; (e, f, and g) Co-precipitation calcined at 1023 K and 1173 K at pH 2, pH 7, and pH 10, respectively (continued).

2.3.3 Scanning electron microscopy (SEM)

Scanning electron microscope (SEM) images were obtained from samples applied to carbon tape using FEI SEM Quanta Inspect S50 Scanning electron microscope operated at an accelerating voltage of 15-30 kV equipped with EDX-Oxford INCA PENTA system for determining the elemental distribution on the surface of the sample. SEM images of prepared photocatalysts are shown in Figure 11. The morphologies of $BiNbO_4$ photocatalysts prepared under co-precipitation method

Figure 11 (a-c) show the formation of agglomerated particles. However, $BiNbO_4$ photocatalysts prepared under co-precipitation with surfactants Figure 11 (d-f), irregular grains were obtained. Moreover, under hydrothermal conditions, photocatalyst prepared at pH 2, Figure 11 (g), shows a stretched agglomeration with rough surface and low porosity, nevertheless as the pH increases particles turns into condensed compact structure of agglomeration fine powders. Furthermore, applying citrate precursor method, agglomeration across all pH values under study is observed. Particles prepared using citrate precursor method (Figure 11 (j-l)) and hydrothermal condition Figure 11 (g-i) appeared to be larger than the other preparation conditions under the same magnification. This can be attributed to the presence of severe particle agglomeration.

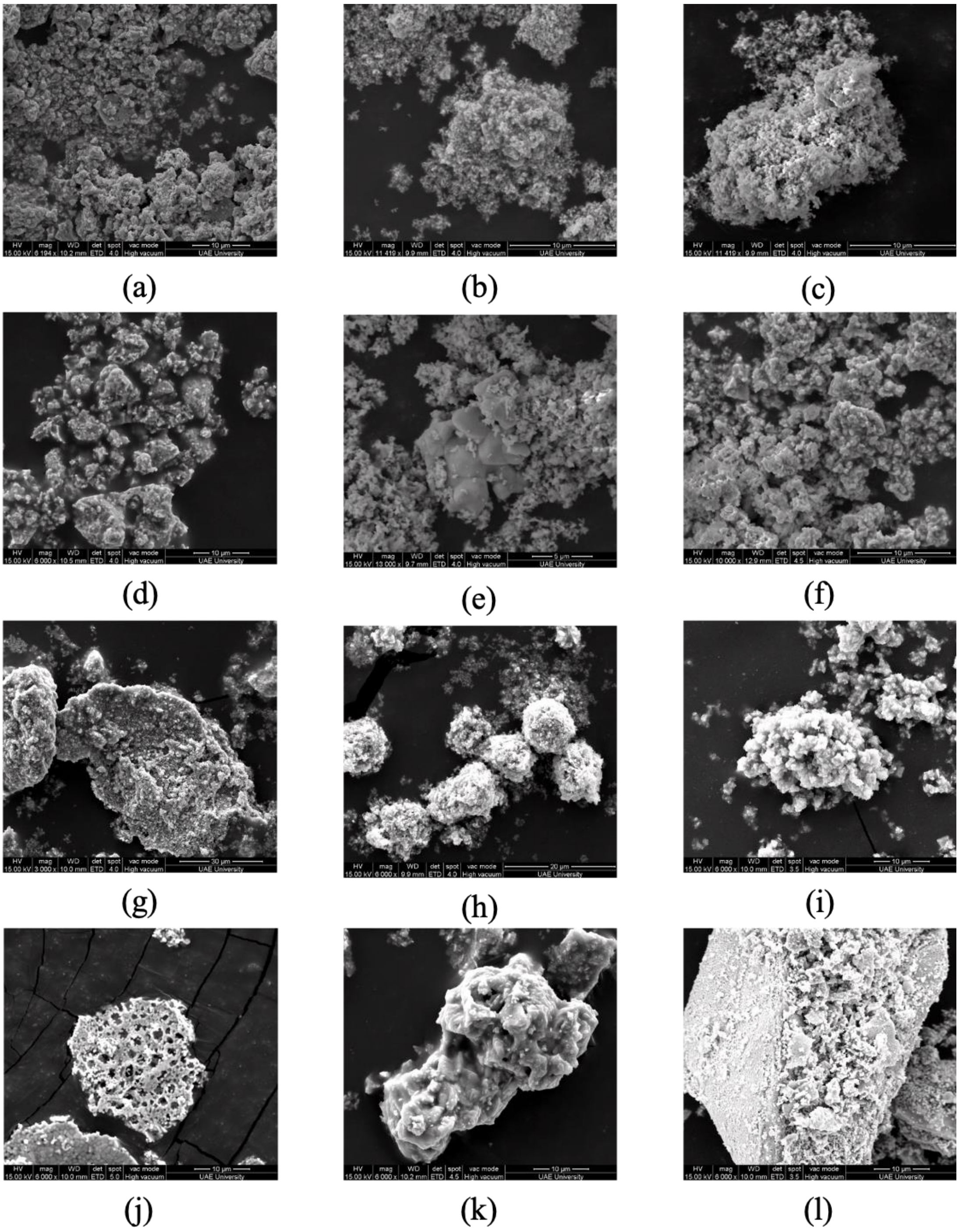

Figure 11: SEM images of $BiNbO_4$ calcined at 1023 K. (a) co-precipitation; pH 2, (b) co-precipitation, pH 7; (c) co-precipitation, pH 10; (d) co-precipitation, EG; (e) co-precipitation, PEG; (f) co-precipitation, SDS; (g) hydrothermal, pH 2; (h) hydrothermal, pH 7. (h) hydrothermal, pH 7; (i) hydrothermal, pH 10; (j) citrate precursor, pH 2; (k) citrate precursor, pH 7; (l) citrate precursor, pH 10.

2.3.4 Specific surface area and porosity

Surface area and porosity were characterized using N_2 adsorption at 77 K using a Quantachrome Autosorb-1 volumetric gas sorption instrument. Before measurements, samples were degassed at 473 K for two hours. Brunauer-Emmett-Teller (BET) theory was used to calculate surface area, pore size distributions were determined by Barett-Joyner-Halenda (BJH) model based on the desorption branch of the N_2 isotherms. Specific surface area and porosity data are presented in Tables 1-5. Surface area and pore size for all prepared catalysts were investigated using nitrogen adsorption/desorption isotherm. As presented in Tables 1-4, surface area for hydrothermally prepared photocatalysts is the highest when compared to other photocatalysts prepared under co-precipitation or citrate precursor conditions. Moreover, prepared photocatalysts at pH 2 and pH 7 using citrate method exhibited lager surface area than those prepared by co-precipitation method. The adsorption-desorption isotherm for the samples is of a type III isotherm with observed hysteresis loop range of 0.8-1.0 P/P^o. According to the obtained data, pore size ranges from 5.6 nm-7.8 nm, indicating that all photocatalysts possess mesoporous structures. Furthermore, hydrothermally prepared samples showed quite higher pore volume, especially sample prepared at a pH 7 and 1.

Table 1: Physical structure parameters of $BiNbO_4$ prepared using co-precipitation method at 1023 K.

pH condition	Band gap energy (eV)	S_{BET} ($m^2 g^{-1}$)	Pore size (nm)	V_{pores} (p/p°=0.95) (10^{-3} cm^3 g^{-1})	Crystalline size (nm)	Lattice constants							
						sys[a]	a (Å)	b (Å)	c (Å)	α /°	β /°	γ /°	Vol (Å^3)
2	2.86	1.0	7.6	1.9	23.1	T	7.66	5.54	7.91	90.09	78.11	86.65	327.88
						O	4.99	11.701	5.687	90	90	90	332.10
7	3.3	3.1	6.1	4.7	35.7	T	7.51	5.51	7.90	90.14	77.09	91.93	318.53
						O	4.96	11.65	5.66	90	90	90	309.25
10	3.3	2.9	5.7	4.1	34.3	T	7.26	5.50	8.03	91.94	74.04	82.61	305.58
						O	4.97	11.68	5.68	90	90	90	330.04

[a] sys refers to the crystalline system of $BiNbO_4$; T, triclinic and O, orthorhombic.

Table 2: Physical structure parameters of $BiNbO_4$ prepared using hydrothermal method at 1023 K

pH condition	Band gap energy (eV)	S_{BET} ($m^2 g^{-1}$)	Pore size (nm)	V_{pores} $_{(p/p°=0.95)}$ (10^{-3} cm^3 g^{-1})	Crystalline size (nm)	Lattice constants							
						sys[a]	a (Å)	b (Å)	c (Å)	α /°	β /°	γ /°	Vol (Å^3)
2	3.26	6.2	5.9	9.2	13.5	T	7.12	5.19	7.47	89.88	76.34	87.53	267.62
						O	4.94	11.63	5.65	90	90	90	324.60
7	3.43	12.9	7.5	24.3	23.1	T	-	-	-	-	-	-	-
						O	-	-	-	-	-	-	-
10	3.43	20.5	7.6	39.1	21.1	T	7.28	5.19	7.48	86.03	77.63	87.13	274.79
						O	4.91	11.81	5.73	90	90	90	332.27

[a] sys refers to the crystalline system of $BiNbO_4$; T, triclinic and O, orthorhombic.

Table 3: Physical structure parameters of $BiNbO_4$ prepared using citrate method at 1023 K

pH condition	Band gap energy (eV)	S_{BET} ($m^2 g^{-1}$)	Pore size (nm)	V_{pores} (p/p°=0.95) (10^{-3} cm^3 g^{-1})	Crystalline size (nm)	Lattice constants							
						sys[a]	a (Å)	b (Å)	c (Å)	α /°	β /°	γ /°	Vol ($Å^3$)
2	3.25	4.6	7.4	8.8	11.8	T	7.39	5.20	7.35	90.86	78.39	86.01	275.13
						O	4.84	11.84	5.74	90	90	90	328.93
7	2.69	4.5	7.0	8.0	-	T	-	-	-	-	-	-	-
						O	5.03	11.70	5.64	90	90	90	331.92
10	3.16	4.6	7.4	8.8	21.8	T	7.26	5.17	7.44	89.59	77.14	86.65	271.62
						O	4.79	11.75	5.73	90	90	90	322.50

[a] sys refers to the crystalline system of $BiNbO_4$; T, triclinic and O, orthorhombic.

Table 4: Physical structure parameters of $BiNbO_4$ prepared using co-precipitation method at 1023 K, pH 2 with Surfactant.

Surfactant	Band gap energy (eV)	S_{BET} ($m^2 g^{-1}$)	Pore size (nm)	V_{pores} (p/p°=0.95) (10^{-3} cm^3 g^{-1})	Crystalline size (nm)	Lattice constants							
						sys[a]	a (Å)	b (Å)	c (Å)	α /°	β /°	γ /°	Vol ($Å^3$)
No surfactant	2.80	1.0	7.6	1.9	23.1	T	7.66	5.54	7.91	90.09	78.11	86.65	327.88
						O	4.99	11.70	5.69	90	90	90	332.10
SDS	2.77	1.6	6.3	2.5	41.1	T	7.33	5.16	7.43	89.79	78.54	85.4	274.45
						O	4.95	11.72	5.71	90	90	90	331.26
PEG	3.30	1.2	5.7	1.7	32.9	T	-	-	-	-	-	-	-
						O	4.92	11.67	5.67	90	90	90	325.19
EG	2.6	0.6	7.8	1.2	18.6	T	7.63	5.51	7.92	90.56	102.0	86.34	325.29
						O	4.97	11.75	5.67	90	90	90	331.49

[a] sys refers to the crystalline system of $BiNbO_4$; T, triclinic and O, orthorhombic.

Table 5: Physical structure parameters of $BiNbO_4$ prepared using co-precipitation method at 1173 K

pH condition	Band gap energy (eV)	Crystalline size (nm)	Lattice constants							
			sys[a]	a (Å)	b (Å)	c (Å)	α /°	β /°	γ /°	Vol (Å^3)
2	3.13	43.5	T	-	-	-	-	-	-	-
			O	4.97	11.69	5.67	90	90	90	329.4
7	3.3	34.3	T	7.57	5.52	7.91	90.12	77.33	87.60	322.73
			O	4.94	11.69	5.67	90	90	90	327.43
10	3.3	47.7	T	-	-	-	-	-	-	-
			O	-	-	-	-	-	-	-

[a] sys refers to the crystalline system of $BiNbO_4$; T, triclinic and O, orthorhombic.

2.4 Conclusion

In the present study, a combination of orthorhombic α-$BiNbO_4$ and triclinic β-$BiNbO_4$ was always obtained when calcined at a temperature range from 1023 K to 1173 K. PXRD patterns suggest the co-existence of both phases where preferred phase formation is pH and temperature dependent. When co-precipitation method is used, it was observed that pH plays an important role towards the formation of β-$BiNbO_4$ phase, where high pH promotes β- β-$BiNbO_4$ structure, while low pH results in α-$BiNbO_4$ phase. In such a case, $BiNbO_4$ prepared at pH 2 shows the narrowest band gap of 2.86 eV with dominant α-$BiNbO_4$ phase present. Using citrate precursor method, $BiNbO_4$ prepared at pH 7 shows the narrowest band gap of 2.69 eV with dominant α-$BiNbO_4$ phase present, whereas, at acidic or basic conditions wider band gaps >3.0 eV were obtained with dominant β-$BiNbO_4$ phase present. Using hydrothermal approach, $BiNbO_4$ prepared at all pH range of present study show band gap >3.2 eV indicating their absorbance in the UV region. Finally, as temperature increases to 1173 K, a gradual transformation of α- to β is observed. Finally, it can be noticed that as the lattice volume increases, the band gap decreases.

Chapter 3: $BiNbO_4$/r-GO Nanocomposite

3.1 Introduction

Since the first report on electrochemical Photocatalytic water splitting using TiO_2 electrode, many oxide semiconductor photocatalysts have been subject to an intensive research studies.[26] The wide band gap of titanium dioxide (~3.2 eV) limits its photocatalytic activities excluding the UV light irradiation, hence, limits their use in practical applications under visible or IR irradiation, as the solar light is made of only 4% UV light. On the other hand, visible light makes up to 46% of the total solar radiation, representing a more useful region in the solar spectrum. Therefore, the design and synthesis of photocatalysts that utilize most of the energy in the visible light is of particular interest. Thus, for an effective utilization of visible light, semiconductor photocatalysts band gap should be ~ 2 eV.[124,125] Metal oxides and mixed metal oxides continue to be promising candidates for achieving such task because of their stability, low-cost and suitable band gap engineering.[126]

Metal oxides semiconductor visible light photocatalysts have drawn great interest in the past owing to their significant performance in removal of organic pollutants, hydrogen production from water splitting and energy conversion via CO_2 reduction.[127,128] Many metal oxides photocatalysts with visible light activities have been utilized for such aforementioned application.[129–132] Among them, metal oxide and mixed metal oxides containing bismuth photocatalysts were extensively studied due to their unique band structures, such photocatalysts includes: $BiVO_4$, Bi_2WO_6, and Bi_2MoO_6.[133–135] Since the valence band (VB) is hybridized Bi 6s and O 2p orbitals, it would greatly contribute to the band gap narrowing resulting in visible-light absorption of Bi-based oxides.[136]

Recently, bismuth niobate, $BiNbO_4$, has received much attention due to their excellent microwave dielectric properties, low sintering temperatures,[119,137] potential application in ferroelectrics,[138] optoelectronics,[139] luminescence,[140] micro-electro-mechanical system (MEMS)[141] and enhanced photocatalytic activities,[82] Moreover, $BiNbO_4$ have been studied and found to be photoactive for hydrogen evolution and organic pollutant removal.[75,142] Nevertheless, its quantum efficiency and photocatalytic performance is restricted due to the high recombination rate of photogenerated electron-hole pairs. To overcome this drawbacks, researchers attempted to prepare hybrid photocatalysts since the formation of a heterojunction with a conductive materials can suppress the recombination, leading to much efficient photocatalyst.[143–145]

Recently, research was devoted towards the preparation of nanocomposites that combines carbon materials and mixed metal oxides as a new scheme in photochemical catalysis.[146,147] Among various composites, bismuth niobate ($Bi_5Nb_3O_{15}$) / graphene nanocomposite, which has been reported as a photocatalytic system that combines the photocatalytic properties of the mixed metal oxide and the high-performance support of graphene-based materials. Moreover, the strong interaction between the matrix of graphene and the metal oxides nanoparticles is of great interest due to the effective visible light harvesting properties of the oxide that is coupled with the short electron diffuse length provided by the graphene sheet. The catalytic performance of the composite was found to be higher compared to those of individual pure compounds.[148]

Here in, $BiNbO_4$/r-GO nanocomposite have been synthesized through mechanical mixing, their photocatalytic activity was evaluated using photocatalytic cycloaddition of carbon dioxide into propylene oxide, producing selectively cyclic propylene carbonate without any polymeric material observed. This photoreaction has never been attempt using mixed metal oxide r-GO composite.

3.2 Experimental

Materials: Graphite powder (+100 mesh), NH_4OH, hydrazine hydrate, sulfuric acid, $NaNO_3$, $KMnO_4$, $NaBH_4$, 37% HCl ACS reagent and 30% H_2O_2 solution were purchased from Sigma Aldrich, all purchased chemicals were used as received.

Synthesis of r-GO: Reduced graphene oxide (r-GO) was synthesized via the exfoliation of graphite as follow: 2 g of graphite powder and 0.12 g of $NaNO_3$ were mixed in 60 mL sulfuric acid and kept under constant stirring for 1 h in an ice bath. After that, 6 g of $KMnO_4$ was added gradually to the mixture while stirring in an ice bath and left under constant stirring for another 1 h. later, 60 mL deionized water (DIW) was gradually added to the mixture. The mixture was kept stirring at 363 K for 30 min. An additional 200 mL of DIW was added, followed by addition of 30 mL H_2O_2 solution. The obtained graphene oxide (GO) powder was filtered and washed several times with 2 M HCl and DIW, dried for 1 day at 373 K. Subsequently, GO was chemically reduced using 15 mL hydrazine hydrate and kept stirring for 5 h. The reduced product was then washed with DIW, filtered and dried in oven at 373 K for a day.

Synthesis of $BiNbO_4$/r-GO Nanocomposites: $BiNbO_4$ was prepared at pH 2 using coprecipitation method and calcined at 1023 K as previously discussed in (Chapter 2). Three different photocatalyst composites have been prepared using simple mechanical mixing followed by heat and high-pressure treatment in a hydrothermal reactor. The composite denoted as $BiNbO_4$/5% r-GO was prepared as follows: in a Porcelain Pestle, 0.05 g of r-GO was added to 0.95 g of $BiNbO_4$ and mixed in 5 mL acetone as a reaction medium. The suspension was grinded until the acetone was evaporated completely. The previous step was repeated several times. Afterwards, the dried powder was transferred into a high-pressure reactor and 10 mL deionized water was added. The reactor was sealed and heated at 423 K for 24 hours. Sample was collected and dried at 373 K. Same procedure was implemented for the preparation of the remaining photocatalysts which were denoted as $BiNbO_4$/1%r-GO and $BiNbO_4$/10% r-GO.

3.3 Characterization of Nanocomposite

This section provides a detailed investigation of the analytical methods and techniques used to characterize structure and properties of the obtained photocatalysts. Such investigation considers structural, optical, morphological and elemental analysis of the as synthesized photocatalysts with the aim of determining their ability to undergo light driven photocatalytic transformations. The effect of r-GO on structural surface morphology and optical properties of the prepared photocatalysts was characterized using diffuse reflectance spectroscopy (DRS), powder X-ray diffraction (PXRD), scanning electron microscopy (SEM), energy dispersive X-Ray spectroscopy (EDX), Brunauer-Emmett-Teller for determination of the specific surface area and porosity (BET).

3.3.1 Powder x-ray diffraction (PXRD)

The crystalline structure and the purity of $BiNbO_4$/r-GO composites were analyzed and confirmed using Shimadzu-6100 powder XRD diffractometer equipped with (Cu Kα) radiation tube with a working voltage of 40 Kv and current of 30 mA, where $\lambda = 1.542$ Å over 2θ range of 10°–80° at a rate of 2°/min. Figure 12 represents the PXRD patterns of the associated photocatalysts composites. Lattice parameters of the prepared composites were calculated using Bragg's law and the crystalline sizes were calculated using Scherrer equation as discussed previously in (Chapter 2).

The PXRD patterns on Figure 12 (b) is perfectly indexed to that of pure $BiNbO_4$. According to the standard PXRD database for $BiNbO_4$, there are no extra peaks correspond to any impurities present in the sample. As for the prepared reduced graphene oxide particles Figure 12 (a), the characteristic peak correspond to r-GO appears at $2\theta = 26.3°$. The PXRD patterns of $BiNbO_4$/r-GO composites photocatalysts exhibited a combination of similar diffraction peaks correspond to both; pure $BiNbO_4$ and r-GO. It can be observed that the peaks correspond to $BiNbO_4$/r-GO coincide with those of pure $BiNbO_4$ in which all patterns indicate the presence of exact phase as pure $BiNbO_4$, with no extra peaks correspond to impurities or newly formed lattice structure. It's evident that, the intensity of r-GO peak increases upon increasing the amount of r-GO added, which reflects the percent amount of r-GO that exist in the samples. The r-GO peaks are marked in Figure 12; red arrow. Interestingly, the change in the lattice parameters associated with the shift of the peaks positions is due to the variation of the chemical composition upon increasing the amount of r-GO added. Such variation shall not contribute to the actual cell parameters since the physical mixing of substances does not cause any kind of chemical bond breaking or formation. Calculated cell parameters are listed in Table 6.

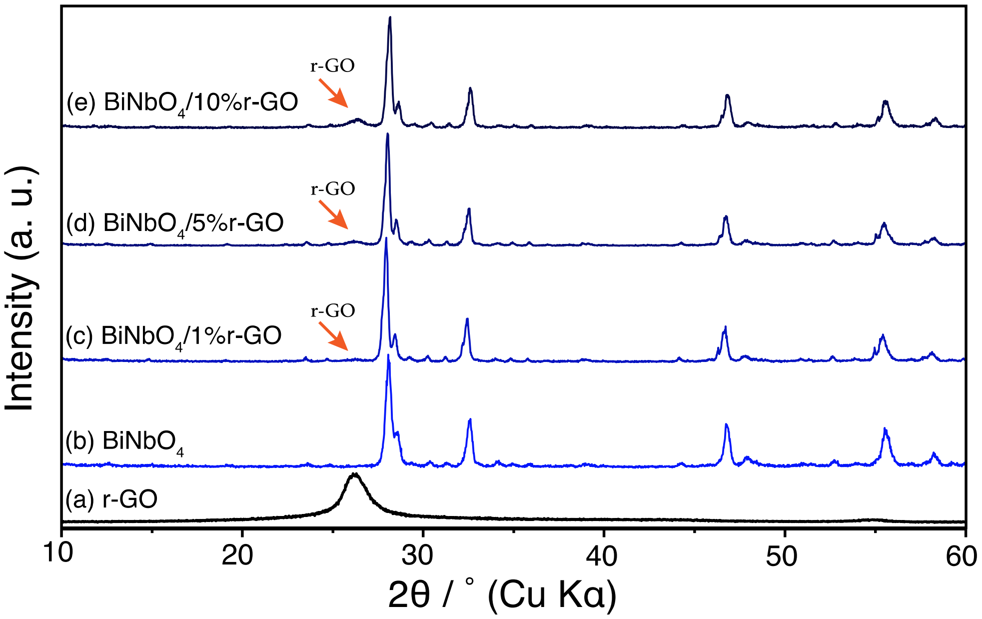

Figure 12: PXRD diffraction patterns of BiNbO$_4$/r-GO composites. (a) r-GO, (b) BiNbO$_4$, (c) BiNbO$_4$/1% r-GO, (d) BiNbO$_4$/5% r-GO, (e) BiNbO$_4$/10% r-GO. The intensity of r-GO peak increases upon increasing the amount of r-GO added. The r-GO peaks present in the composites are marked by a red arrow.

3.3.2 UV-Vis diffuse reflectance spectroscopy (UV-Vis DRS)

Diffuse reflectance spectra (DRS) was obtained using Shimadzu UV-3600 UV-Vis spectrophotometer. Spectra recorded over the range from 200 nm to 800 nm. Baseline correction was done using barium sulfate (BaSO$_4$) as a standard. As previously discussed in Chapter 2, the band gap energies were calculated applying Tauc plot considering that the electrons transitions in BiNbO$_4$ and BiNbO$_4$/r-GO composites are direct allowed transition. As demonstrated in Figure 13, all spectra show a strong light absorbance in the visible light region. Pure BiNbO$_4$ sample exhibit a band gap of 2.74 eV. Compared to pure BiNbO$_4$, the absorption wavelength of BiNbO$_4$/r-GO composites photocatalysts demonstrated a red shift towards lower energy upon increasing the amount of r-GO added. Table 6 lists the calculated band gap energies associated with each of the prepared photocatalysts.

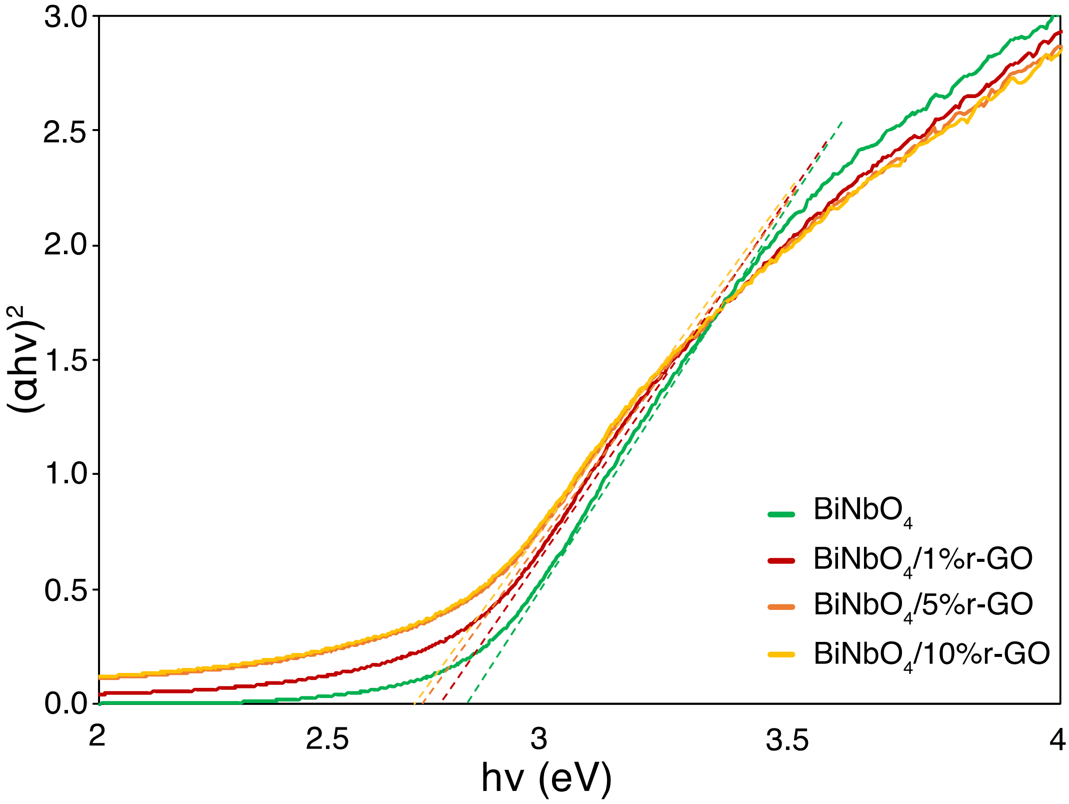

Figure 13: UV-Vis DRS spectrum of $BiNbO_4$/r-GO composites.

Table 6: Physical structure parameters of $BiNbO_4$ and $BiNbO_4$/r-GO composites photocatalysts.

Photoctalysts	Band Gap Energy (eV)	S_{BET} ($m^2\ g^{-1}$)	Pore Size (nm)	$V_{pores\ (p/p°=0.95)}$ ($10^{-3}\ cm^3\ g^{-1}$)	Crystalline Size (nm)	Lattice Constants				
						a (Å)	b (Å)	c (Å)	α=β=γ	Vol (Å)^3
$BiNbO_4$	2.74	0.41	129	0.88/0.97	21.11	4.87	11.82	5.73	90	329.9
$BiNbO_4$/1% r-GO	2.71	1.4	128	2.59/2.66	30.60	4.88	11.86	5.75	90	332.8
$BiNbO_4$/5% r-GO	2.68	2.01	110	3.34/3.35	31.89	4.85	11.84	5.74	90	329.9
$BiNbO_4$/10% r-GO	2.65	2.3	96	3.39/3.44	29.10	4.83	11.79	5.72	90	325.6

3.3.3 Scanning electron microscopy (SEM) analysis

Scanning electron microscopy (SEM) images and energy-dispersive X-ray spectroscopy (EDX) analyses of all prepared photocatalysts were obtained using Quattro ESEM operated at high vacuum with an accelerating voltage of 15–30 kV. The SEM analytical system equipped with EDX detector used to determine the elemental composition of the samples. Conductive carbon adhesive tape was used to mounting the sample during the analysis. Figure 14 shows the SEM images of $BiNbO_4$ and $BiNbO_4$/r-GO composites. Based on the data, images demonstrate a rough rock like morphology correspond to $BiNbO_4$. However, r-GO exhibits a smooth sheet like surface. Combinations of both $BiNbO_4$ and r-GO are clearly shown in the images of the composite samples. Figure 15 shows the elemental mapping of the atoms present in the samples. Based on the data, the elemental mapping indicates that r-GO is well mixed with $BiNbO_4$ particles. Thus, this should facilitate the electron transfer processes needed for reducing the charge recombination rate when catalyzing photoreactions. r-GO is marked in Figure 15 with red arrows. The atomic percent are listed in Table 7.

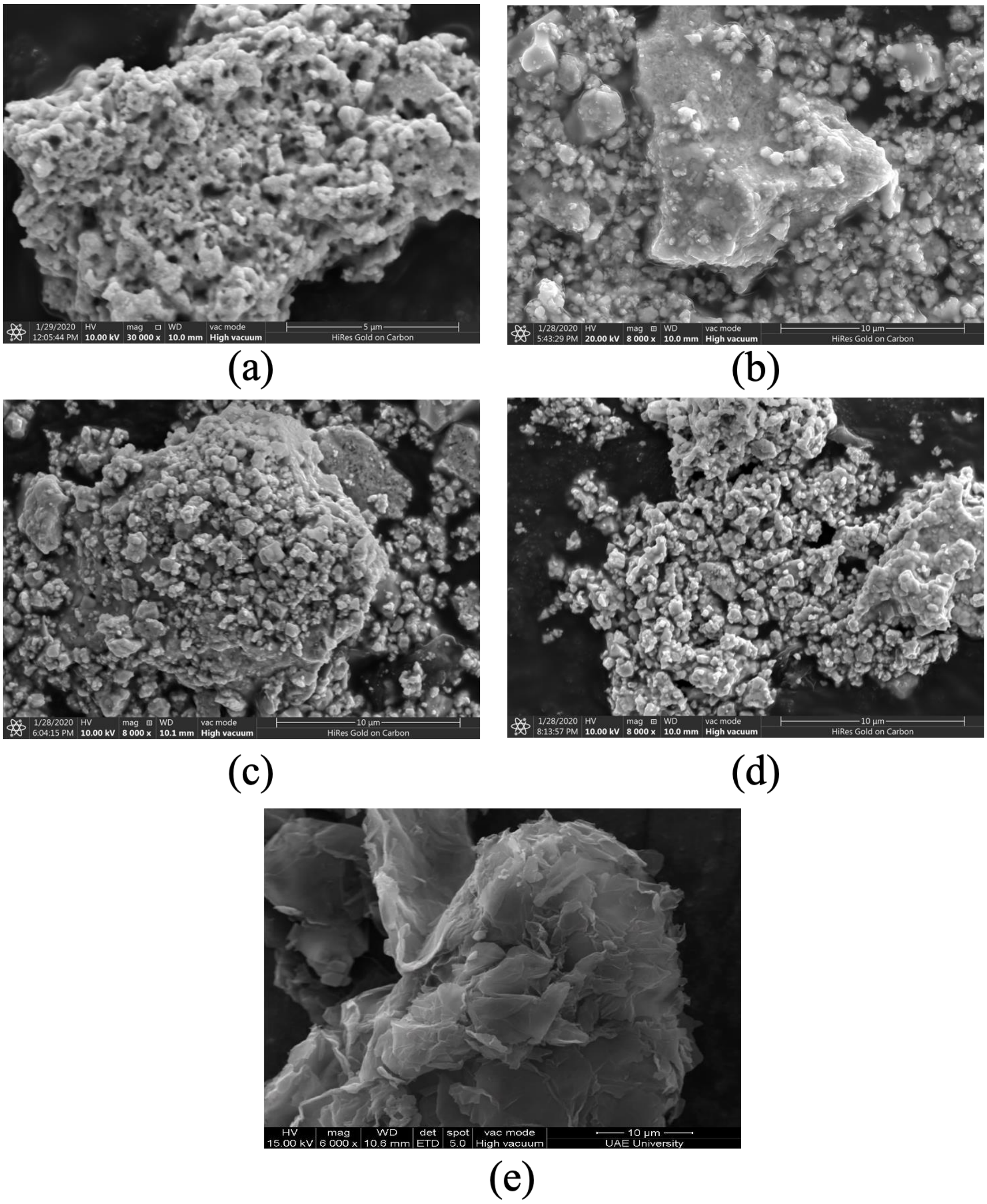

Figure 14: SEM images of $BiNbO_4$/r-GO composite. (a) $BiNbO_4$, (b) $BiNbO_4$/1% r-GO, (c) $BiNbO_4$/5% r-GO, (d) $BiNbO_4$/10% r-GO and (e) r-GO.

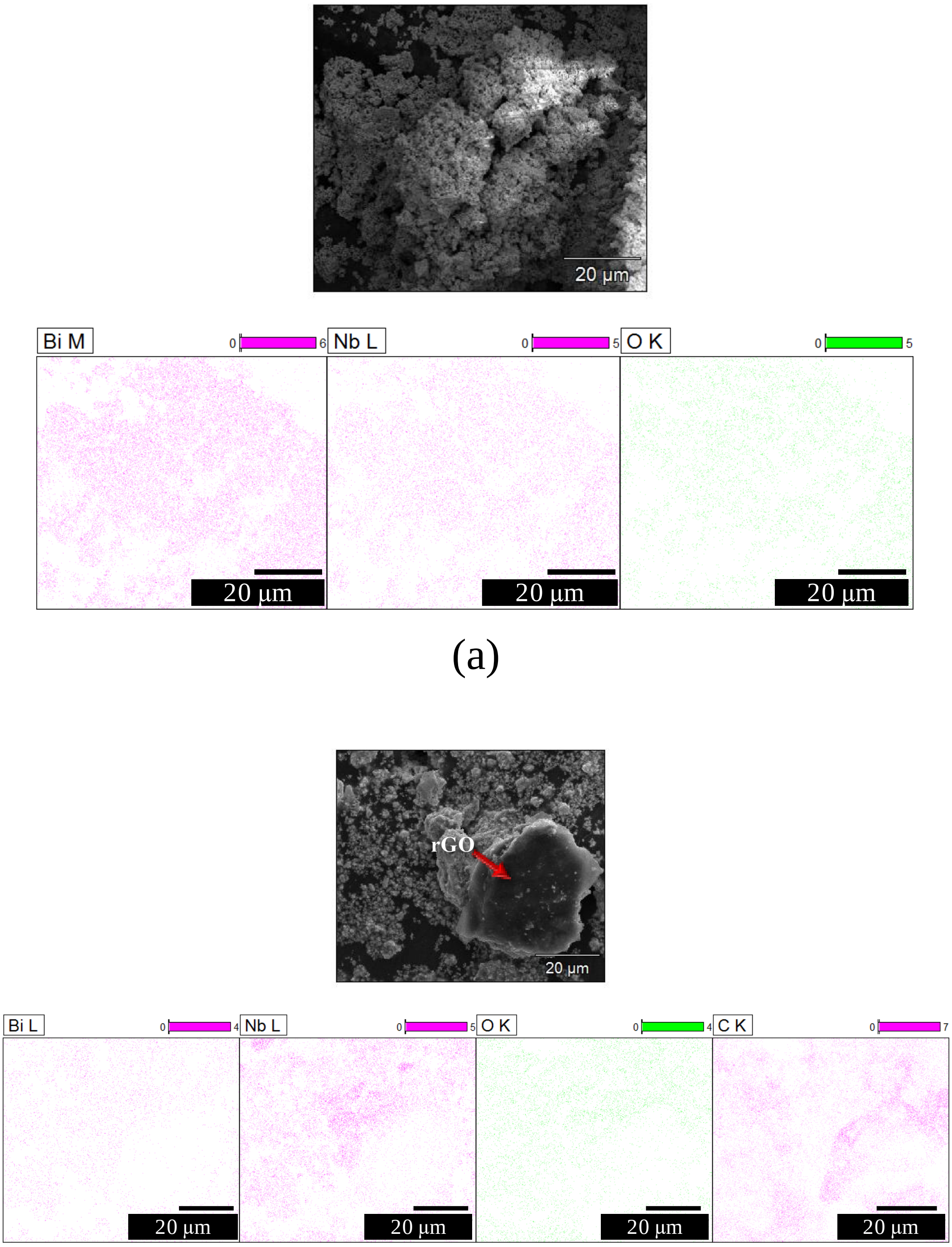

(a)

(b)

Figure 15: Elemental mapping of the atoms present in $BiNbO_4$/r-GO composites. (a) $BiNbO_4$, (b) $BiNbO_4$/1% r-GO, (c) $BiNbO_4$/5% r-GO, (d) $BiNbO_4$/10% r-GO.

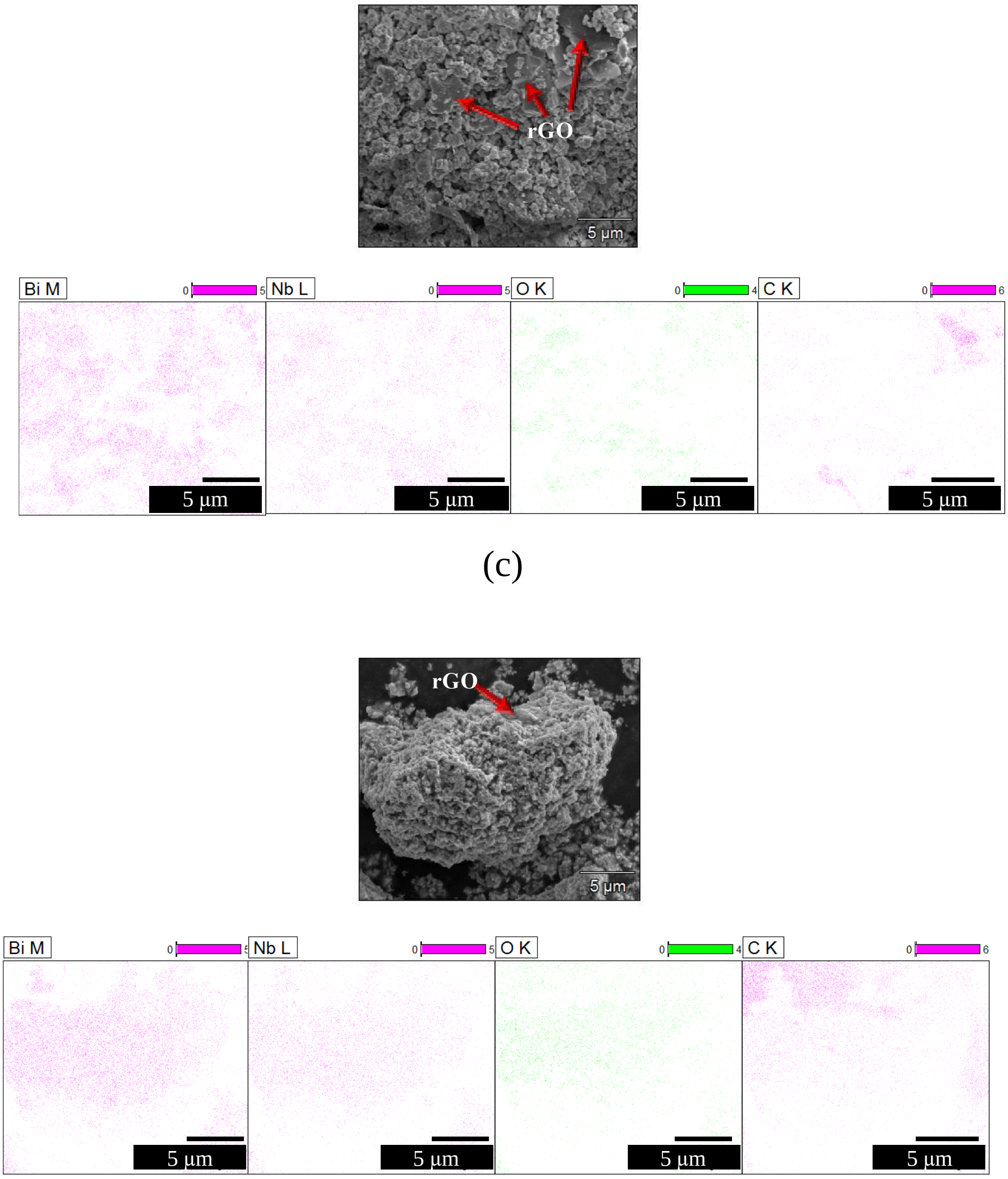

(c)

(d)

Figure 15: Elemental mapping of the atoms present in $BiNbO_4$/r-GO composite. (a) $BiNbO_4$, (b) $BiNbO_4$/1% r-GO, (c) $BiNbO_4$/5% r-GO, (d) $BiNbO_4$/10% r-GO (continued).

Table 7: Elemental analysis of the as prepared samples shows the atomic percent of the atoms present in $BiNbO_4$/r-GO samples.

Photocatalyst	Elemental Analysis (EDX), atom%			
	Bi	Nb	O^a	C^a
$BiNbO_4$	15.20	12.42	72.38	-
$BiNbO_4$/1% r-GO	11.94	6.58	43.60	37.88
$BiNbO_4$/5% r-GO	2.01	1.22	22.68	74.10
$BiNbO_4$/10% r-GO	5.80	3.32	28.41	62.46

[a] Conductive carbon adhesive tape was used to mounting the sample during the analysis. Therefore, C and O% are not representative of the actual elemental composition in the sample.

3.3.4 N_2 adsorption–desorption analysis

The surface area and the pore size of the prepared $BiNbO_4$/r-GO composite was carried out using Brunauer, Emmett and Teller (BET) method. N_2 adsorption desorption isotherms were recorded at 77 K, showing the amount of gas adsorbed (cm^3 g^{-1}) as a function of the relative pressure (p/p^o), where p is the equilibrium pressure of N_2 and p^o is the saturated vapor pressure at 77 K. Prior to the BET measurements, the powder samples were placed in a glass tube and heated at 420 K under vacuum for 2 hours. Figure 16 shows the N_2 adsorption-desorption isotherm. The obtained isotherms belong to type IV isotherm and it shows a very small hysteresis loop compare to $BiNbO_4$/r-GO composite samples. As indicated, the lower branch of the isotherm plot represents the gradual cumulative addition of N_2 gas into the surface of the adsorbent, and the upper branch represents the gradual gas withdrawal. In mesoporous materials, the hysteresis loop that forms in between the two branches is usually associated with the capillary condensation within the pores[149]. With an approximate pore size of 19 nm, $BiNbO_4$ was considered a mesopores material. Moreover, the size of the hysteresis loop increases upon increasing the amount of r-GO added, yet, the average pore size decreased. The surface area yielded the following values; 0.41(m^2g^{-1}) for $BiNbO_4$, 1.4 (m^2g^{-1}) for $BiNbO_4$/1% r-GO, 2.01 (m^2g^{-1}) for $BiNbO_4$/5% r-GO, 2.3 (m^2g^{-1}) for $BiNbO_4$/10% r-GO. Consequently, the average surface area increases upon increasing the amount of r-GO added. Results are listed in Table 6.

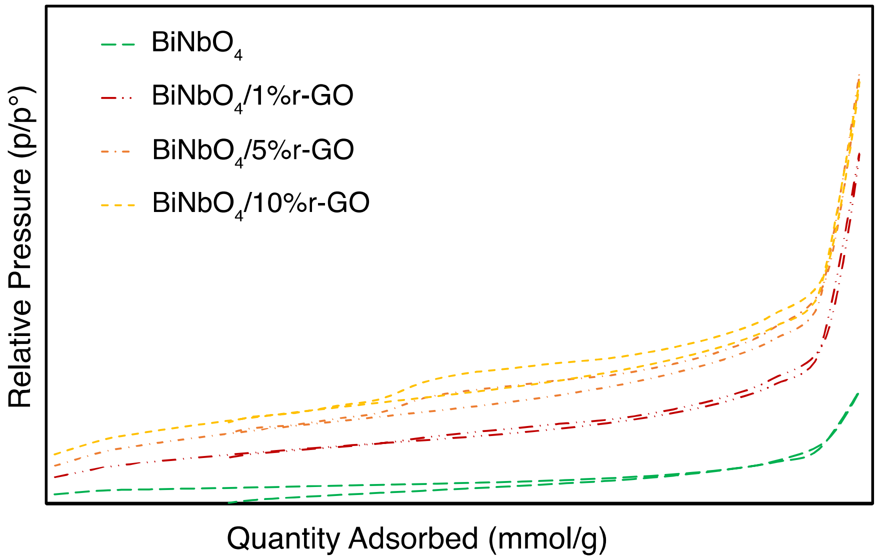

Figure 16: N_2 adsorption isotherm of $BiNbO_4$/r-GO composites.

3.4 Photocatalytic activity

The photocatalytic performance of the prepared samples were evaluated using the photocatalytic cycloaddition of carbon dioxide into the propylene oxide. In a typical reaction: 9 mg of tetra butyl ammonium bromide ($^nBu_4NBr$) co-catalyst was dissolved in a mixture of acetonitrile and methanol (5:1). 50 mg of the prepared photocatalyst and 100 µl of propylene oxide was added to the mixture. The reaction mixture was then transferred in to a 75 mL sealed tube and 0.045 mmol of CO_2 was added to the mixture in a Pyrex sealed tube. The reaction was placed 10 cm away from a 300 W halogen lamp (OSRAM HALOLINE) source and kept stirring for 6 hours under visible light irradiation. The desired organic product was then filtered, extracted using dichloromethane (DCM) and analyzed using nuclear magnetic resonance NMR (Varian 400 MHz) and infrared spectroscopy (IRPrestige-21, Shimadzu) between a scanned from 500 to 4000 cm^{-1} frequency range. The reactions yielded the desired product selectively in a high yield. Obtained results are listed in Table 8. The highest conversion yield was obtained when using $BiNbO_4$/5% r-GO as a photocatalyst, where 65% conversion was obtained. Three control experiments were carried out: in the absence of light at room temperature, in the absence of the prepared semiconductor and in the absence of light at 353 K to confirm the role of the prepared photocatalysts. Results showed that only 9% cyclic propylene carbonate was obtained when using only $^{n}Bu_4NBr$ in the absence of the prepared photocatalyst, and 14% conversion was obtained at 353 K in the absence of light. However, in the absence of light and heat, the reaction yielded no conversion. Using Acetonitrile and methanol as a solvent mixture in such ratio is because acetonitrile enhances the solubility of CO_2 in the reaction mixture. Methanol, in the other hand, acts as a hole scavenger in the photoreaction. The role of the $^{n}Bu_4NBr$ as a co-catalyst was to facilitate the ring opining process at the oxygen radical position formed at the semiconductor valance band. Electrons at the conduction band facilitate the CO_2 radical formation. As a conductor medium reduced graphene oxide sheet provides the support needed to prevent the charge recombination at conduction band by accepting electrons and maintain the charge separation needed for the reaction to continuously produce radicals. A proposed mechanism pathway is shown in Figure 17. The enhanced photocatalytic activity of $BiNbO_4$/5% r-GO was attributed to the high visible light absorption capability of $BiNbO_4$ particles. Moreover, using only 5 % r-GO was found to be optimal in the photocatalytic system, because this amount is enough to provide the support needed for the charge separation. Increasing the amount of r-GO up to 10% suppress the photocatalytic activity which can be attributed to hindering the maximum visible light absorption by r-GO Figure 18.

Table 8: Cycloaddition of CO_2 into PO[a] catalyzed by $BiNbO_4$/r-GO.

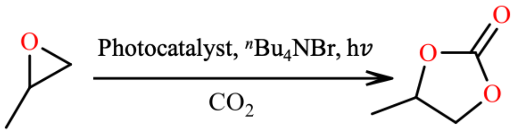

Entry	Photocatalyst	Yield[b] %	TON[c]	TOF$(x10^{-2})$[d]
1	$BiNbO_4$	37	0.9	3.7
2	$BiNbO_4$/1% r-GO	59	0.4	1.6
3	$BiNbO_4$/5% r-GO	65	0.32	1.3
4	$BiNbO_4$/10% r-GO	11	0.05	0.19

[a] Reaction conditions: epoxide (100 μL), photocatalyst (50 mg), ${}^{n}Bu_4NBr$ (9 mg) and carbon dioxide (1.48 MPa) at 353 K and 24 h.

[b] Yield of isolated product was determined by ^{1}H NMR spectroscopy, ^{13}C NMR and IR spectroscopy.

[c] TON= (mols of product)/(S_{BET} of the catalyst).

[d] TOF= (mols of product)/(S_{BET} of the catalyst)(reaction time, hour).

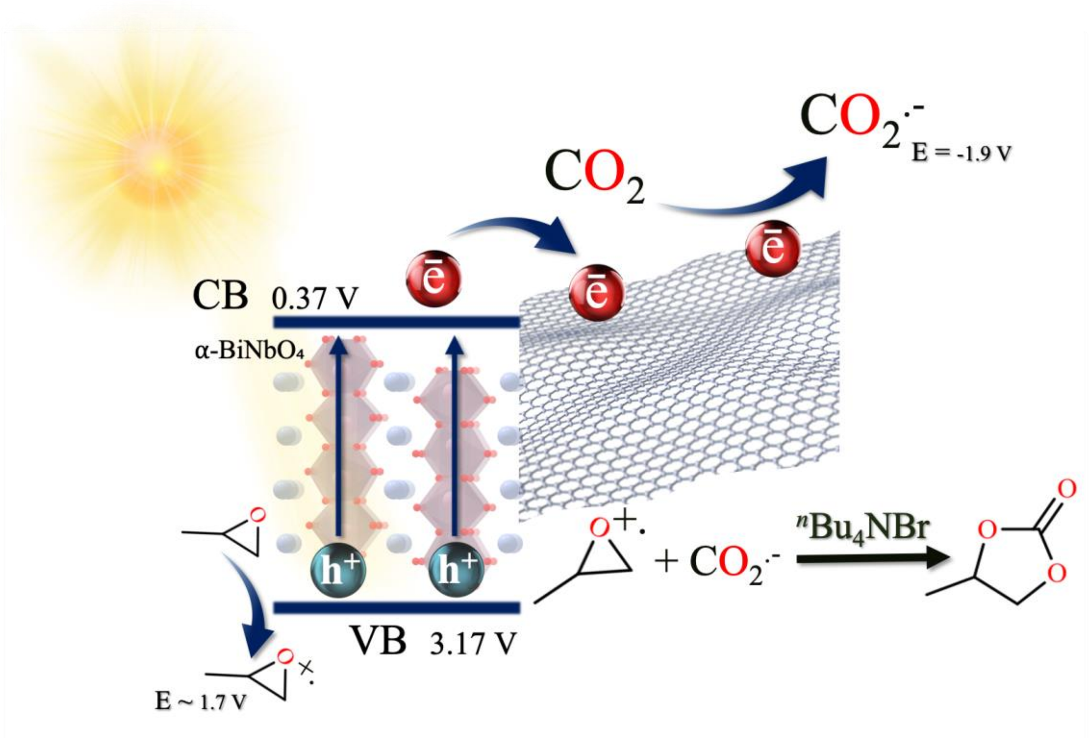

Figure 17: Proposed mechanism pathway of the photocatalytic cycloaddition of CO_2 into propylene oxide.

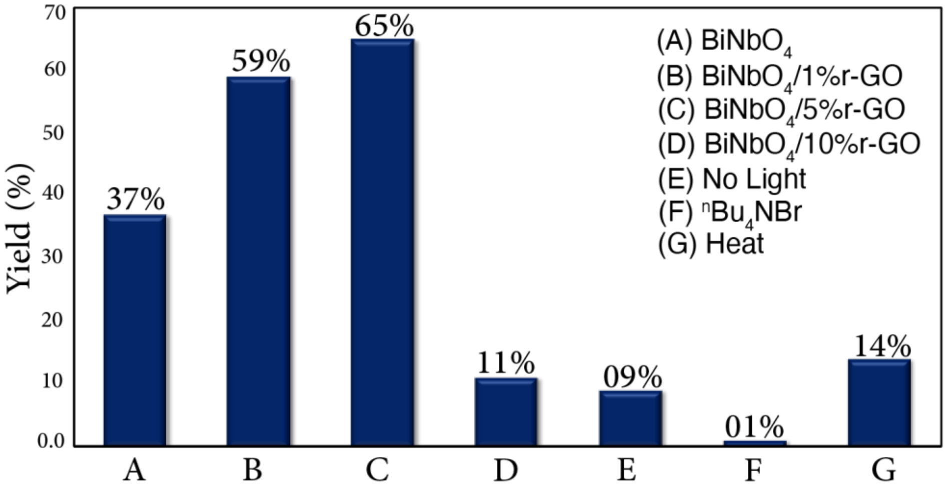

Figure 18: Bar chart represents yield of the obtained cyclic-propylene carbonate.

3.5 Conclusion

In short, the synthesis of reduced graphene oxide based $BiNbO_4$ nanocomposites was reported. Different ratios were prepared, their structures were analyzed and confirmed using PXRD. The obtained results showed no extra peaks correspond to newly formed impurities. The prepared composites exhibit an exaptational photocatalytic activity toward the cycloaddition of CO_2 into propylene oxide under visible light irradiation. The highest conversion yield achieved when using 5% r-GO. Apparently, high reduced graphene oxide ratio hinders the light harvesting process. However, it suppresses charge recombination and at 5% loading under the condition of this study, maintains the photoinduced electron-hole pairs. Hence, enhances the proses of radical formation that are necessary for the photocatalytic reaction to proceed.

Chapter 4: MOFs Modified $BiNbO_4$

4.1 Introduction

Recently, there has been an ongoing effort to combine MOFs with various materials to produce more efficient performing materials.[150–152] MOFs hybrid materials can incorporate an excellent properties and mitigate the shortcomings of the individual counterparts.[153,154] Many MOFs composites have been synthesized by incorporating various active materials such as: metal/metal oxides nanoparticles, carbon materials, polymers, polyoxometalates (POMs), quantum dots, ionic liquids, and others.[155–157] Synthesized MOFs composites have been utilized in many applications such as: gas storage, separation, sensing, catalysis and much more.[158–165]

As a heterogeneous catalysts, MOFs composites show improved characteristics due to possessing high porosity with ordered crystalline structures and high surface areas contribute to the uniform dispersion and the high availability of catalytic sites, which in turn increase their catalytic efficiency.[166,167] Surely, the confined pore sizes can inhibit the growth and agglomeration of the active species, and selectively transport substrate for size-selective catalysis.[168,169]

In this chapter, the design and syntheses of a new mixed metal oxide/MOFs photocatalysts has been presented. Namely, $BiNbO_4$/NH_2-MIL-125(Ti) composites, their photocatalytic activity toward CO_2 cycloaddition to propylene oxide. The photocatalytic incretion of CO_2 into epoxide via the incorporation of semiconductor photocatalyst and amine factionalized MOFs has not been reported yet.

4.2 Experimental

Synthesis of MIL-125-NH_2(Ti): All chemicals were purchased from Sigma-Aldrich and used without further purifications. In a typical reaction, (2-Amino-1,4-benzenedicarboxylic acid, NH_2-BDC) (1.1 mg, 6 mmol) was dissolved in a mixture of DMF and methanol (50 mL, 1:1 v/v) and kept stirring for 30 min. Titanium (IV) isopropoxide (888 mL, 3 mmol) was then added to the mixture and kept stirring for an hour. The mixture was transferred into a Pyrex sealed tube and heated at 423 K for 24 hours. After time has elapsed, the reaction was cooled to room temperature. The yellow product was recovered by filtration then washed three times with DMF to remove the unreacted materials, then the powder was washed several times with methanol. After that, the powder was soaked in DCM for 3 hours to exchange the trapped solvents with DCM. Last step was repeated several times. Finally, the solid yellow powder was dried at 373 K for 24 hours to afford the pure product as confirmed by PXRD.

Synthesis of $BiNbO_4$/NH_2-MIL-125(Ti) composites: $BiNbO_4$ was prepared at pH 2 using coprecipitation method and calcined at 1023 K as previously discussed in (Chapter 2). Three different photocatalyst composites were prepared using simple mechanical mixing. The composite denoted as $BiNbO_4$/NH_2-MIL-125(Ti)$_{(50:50)}$ was prepared as follows: in a Porcelain Pestle, 0.5g of NH_2-MIL-125(Ti) was added to 0.5g of $BiNbO_4$ and mixed in 5 mL acetone as a reaction medium. The suspension was grinded until acetone was evaporated completely. Previous step was repeated five times. After that, the powder was collected and dried at 373 K for 5 hours. Same procedure was implemented for the preparation of the remaining photocatalysts which were termed as $BiNbO_4$/NH_2-MIL-125(Ti)$_{(25:75)}$ and $BiNbO_4$/NH_2-MIL-125(Ti)$_{(75:25)}$.

4.3 Characterization of nanoparticles

Detailed investigations of structural, optical, morphological, elemental analyses of NH_2-MIL-125(Ti) and $BiNbO_4$/NH_2-MIL-125(Ti) nanocomposites and list of analytical techniques used for characterization are described in the following section.

4.3.1 Powder x-ray diffraction (PXRD)

The crystalline structure and the purity of $BiNbO_4$/NH_2-MIL-125(Ti) composites were analyzed using Shimadzu-6100 powder XRD diffractometer equipped with (Cu Kα) radiation tube with a working voltage of 40 Kv and current of 30 mA, where $\lambda = 1.542$ Å over 2θ range of 5°– 60° at a rate of 2°/min. Figure 19 represents the PXRD pattern of the prepared $BiNBO_4$, NH_2-MIL-125(Ti) and the composites. The XRD pattern of NH_2-MIL-125(Ti), Figure 19 (e) was perfectly indexed to the pure phase with no extra peaks correspond to impurities present in the samples.[170] The PXRD pattern of $BiNbO_4$/NH_2-MIL-125(Ti) composites photocatalysts exhibited a combination of similar diffraction peaks correspond to both of $BiNbO_4$ and NH_2-MIL-125(Ti). It can be observed that the peaks correspond to composite samples coincide with those of pure substances in which all patterns displayed indicating the presence of same phase as of pure starting material with no extra peaks correspond to impurities or newly formed lattice structure. The intensity of peaks corresponds to $BiNbO_4$ tend to decrease upon increasing the amount of NH_2-MIL-125(Ti) added, which reflects the percent amount of NH_2-MIL-125(Ti) present in the samples. Important to point out, the change in the lattice parameters associated with the shift of the peaks positions is due to the variation of the % composition upon increasing the amount of NH_2-MIL-125(Ti) added. Such variation shall not contribute to the actual cell parameters since the physical mixing of substances does not cause any kind of chemical bond breaking or formation. Calculated cell parameters are listed in Table 9.

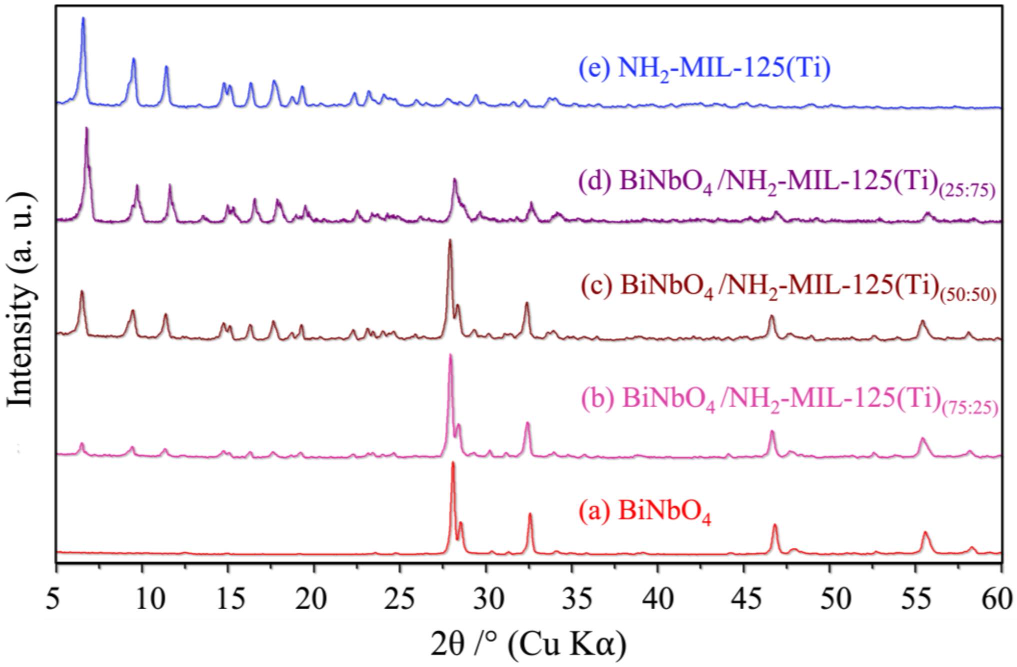

Figure 19: PXRD diffraction patterns of $BiNbO_4$/NH_2-MIL-125(Ti). (a) $BiNbO_4$, (b) $BiNbO_4$/NH_2-MIL-125(Ti)$_{(75:25)}$, (c) $BiNbO_4$/NH_2-MIL-125(Ti)$_{(50:50)}$, (d) $BiNbO_4$/NH_2-MIL-125(Ti)$_{(25:75)}$, (e) NH_2-MIL-125(Ti). The intensity of $BiNbO_4$ peaks decreases upon increasing the amount of NH_2-MIL-125(Ti) added.

4.3.2 UV-Vis diffuse reflectance spectra (DRS)

Diffuse reflectance spectra (DRS) were obtained using Shimadzu UV-3600 UV-Vis spectrophotometer. Spectra recorded over the range from 200 nm to 800 nm. Baseline correction was done using barium sulfate ($BaSO_4$) as a standard. As previously discussed in (Chapter 2), the band gap energies were calculated applying Tauc plot considering that the electrons transitions in $BiNbO_4$ and $BiNbO_4$/NH_2-MIL-125(Ti) composites are direct allowed transition. All spectra show a strong light absorption in the visible light region. NH_2-MIL-125(Ti) has a band edge of 2.69 eV correspond to ligand to metal charge transfer (LMCT), moreover, it is lower than the band gap of $BiNbO_4$, Figure 20. The band edges of both BiNbO and NH_2-MIL-125(Ti) vs. the standard hydrogen electrode are shown in Figure 21. The valance band edge of $BiNbO_4$ is larger than that of NH_2-MIL-125(Ti), therefor the oxidation capacity of $BiNbO_4$ is far more powerful than that of NH_2-MIL-125(Ti).[171] However, when it comes to hydrogen evolution, the conduction bend of NH_2-MIL-125(Ti) is more suitable for such reaction.

Compared to $BiNbO_4$ and NH_2-MIL-125(Ti), the absorption wavelength of $BiNbO_4$/NH_2-MIL-125(Ti) composites photocatalysts exhibited a red shift towards lower energy values upon increasing the amount of NH_2-MIL-125(Ti) added. Table 9 lists the calculated band gap energies associated with each of the prepared photocatalysts.

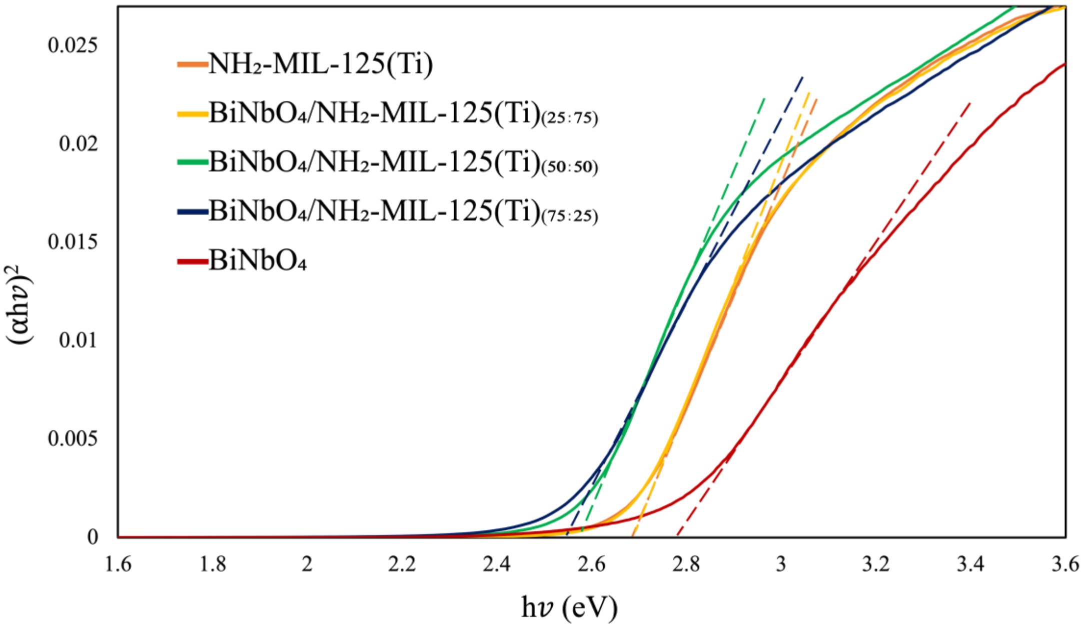

Figure 20: UV-Vis diffuse reflectance spectra of $BiNbO_4$/NH_2-MIL-125(Ti). $BiNbO_4$ (red), NH_2-MIL-125(Ti) (green), $BiNbO_4$/NH_2-MIL-125(Ti)$_{(25:75)}$ (yellow), $BiNbO_4$/NH_2-MIL-125(Ti)$_{(50:50)}$ (orange) and $BiNbO_4$/NH_2-MIL-125(Ti) $_{(75:55)}$ (blue).

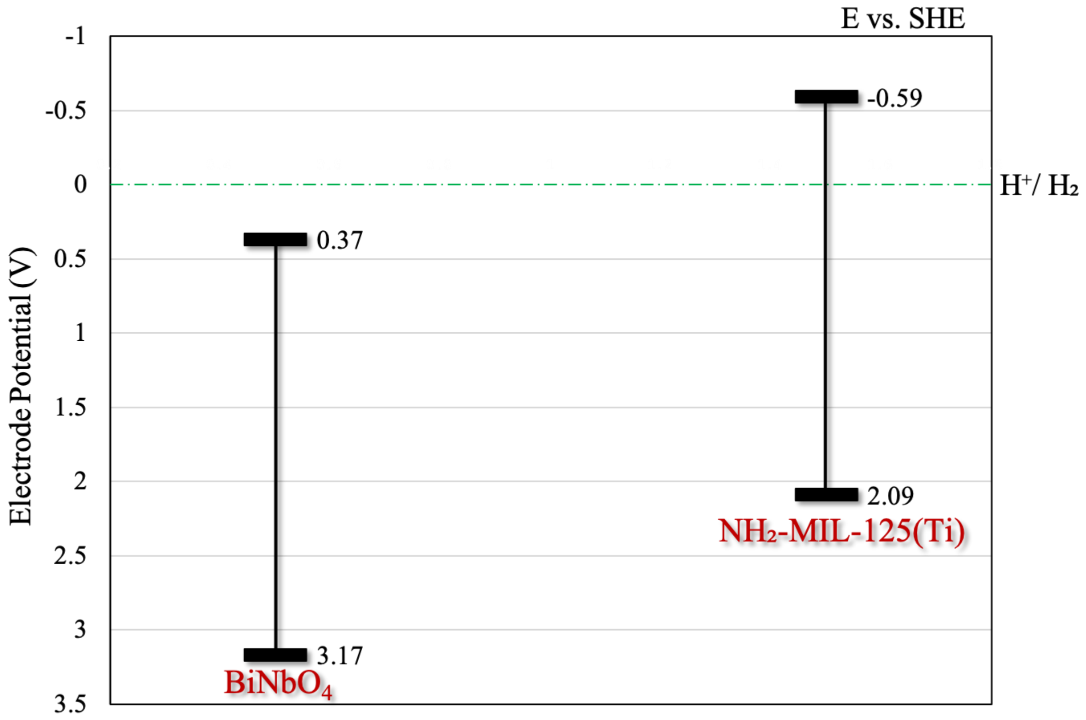

Figure 21: Valence and conduction band positions of $BiNbO_4$, and NH_2-MIL-125(Ti) vs. the standard hydrogen electrode (SHE).

Table 9: Physical structure parameters of NH_2-MIL-125(Ti), $BiNbO_4$ and $BiNbO_4/NH_2$-MIL-125(Ti) composites photocatalysts.

Photocatalysts	Band Gap Energy (eV)	S_{BET} ($m^2 g^{-1}$)	Pore Size (nm)	$V_{pores\ (p/p°=0.95)}$ (cm^3g^{-1})	Crystalline Size (nm)	Lattice Constanats[a]				
						a (Å)	b (Å)	c (Å)	α=β=γ	Vol $(Å)^3$
$BiNbO_4$	2.76	0.41	1.4	0.8/0.9 (10^{-3})	37.5	4.9	11.77	5.71	90	329
$BiNbO_4/NH_2$-MIL-125(Ti)$_{(75:25)}$	2.55	504	2.1	0.268/0.269	31.9	4.9	11.83	5.73	90	332
$BiNbO_4/NH_2$-MIL-125(Ti)$_{(50:50)}$	2.58	777	4.7	0.407/0.408	29.2	4.9	11.84	5.74	90	333
$BiNbO_4/NH_2$-MIL-125(Ti)$_{(25:75)}$	2.68	950.3	5.4	0.522/0.524	11.7	-	-	-	-	-
NH_2-MIL-125(Ti)	2.69	1054	2.1	0.562/0.563	4.95	-	-	-	-	-

[a] Lattice constant was calculated for $BiNbO_4$ orthorhombic phase.

4.3.3 Scanning electron microscopy (SEM)

Scanning electron microscopy (SEM) images and energy-dispersive X-ray spectroscopy (EDX) analyses of all prepared photocatalysts were obtained using Quattro ESEM operated at high vacuum with an accelerating voltage of 15–30 kV. The SEM analytical system equipped with EDX detector used to determine the elemental composition of the samples. Figure 22 displays the SEM images of the synthesized $BiNbO_4$/NH_2-MIL-125(Ti) composites. NH_2-MIL-125(Ti) is a crystalline nanoparticle as shown in Figure 22 (a). It can be noticed that the size of the obtained powder seems to be very small relative to the $BiNbO_4$ shown in Figure 22 (b). Therefore, each of the two material can possibly be distinguished in the images of the mixture samples. The small NH_2-MIL-125(Ti) particles lays at the surface of the rock-like structure of $BiNbO_4$. The atomic percent are listed in Table 10.

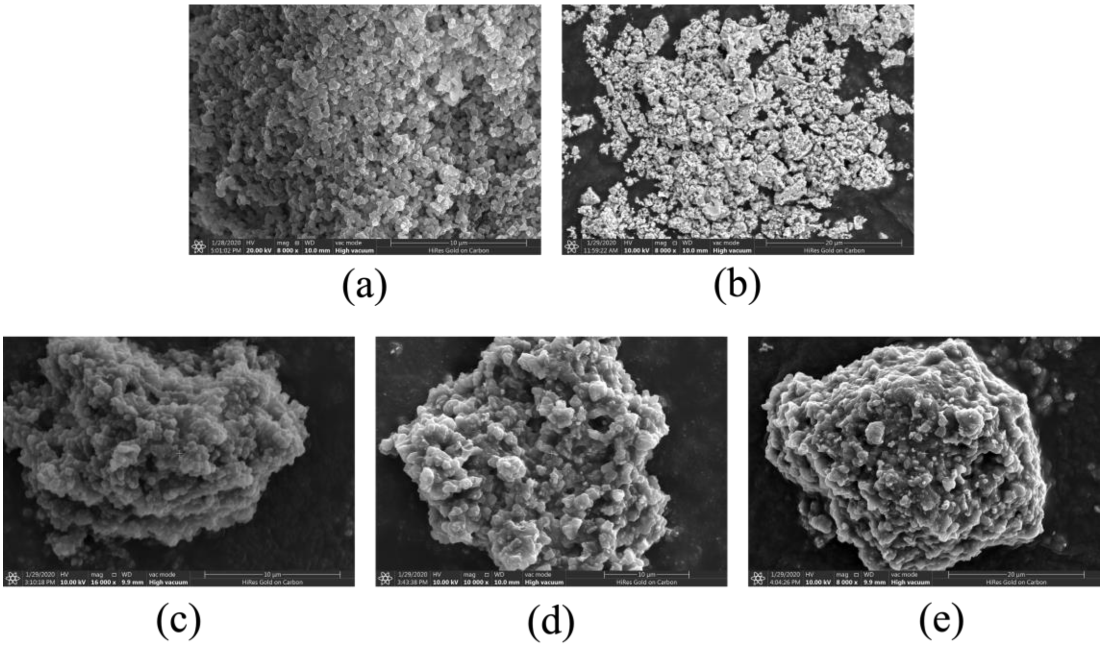

Figure 22: SEM images of $BiNbO_4$/NH_2-MIL-125(Ti). (a) NH_2-MIL-125(Ti), (b) $BiNbO_4$, (c) $BiNbO_4$/NH_2-MIL-125(Ti)$_{(25:75)}$, (d) $BiNbO_4$/NH_2-MIL-125(Ti)$_{(50:50)}$, (e) $BiNbO_4$/NH_2-MIL-125(Ti)$_{(75:25)}$.

Table 10: Elemental analysis of the as prepared samples shows the atomic percent of the atoms present in $BiNbO_4/NH_2$-MIL-125(Ti) samples.

Photocatalyst	Elemental Analysis (EDX), atom %					
	Bi	Nb	Ti	O	N	C
$BiNbO_4$	15.20	12.42	-	72.38	-	-
$BiNbO_4/NH_2$-MIL-125(Ti)$_{(75:25)}$	1.72	2.58	8.51	35.34	7.94	43.91
$BiNbO_4/NH_2$-MIL-125(Ti)$_{(50:50)}$	0.72	2.34	8.71	34.42	7.13	46.68
$BiNbO_4/NH_2$-MIL-125(Ti)$_{(25:75)}$	0.14	1.03	4.02	33.59	6.70	54.51
NH_2-MIL-125(Ti)	-	-	19.68	33.19	8.13	39.00

4.3.4 N_2 adsorption–desorption analysis

To examine the surface area and porosity of the prepared $BiNbO_4/NH_2$-MIL-125(Ti) composites, N_2 adsorption isotherm was performed at 77 K. Prior to the measurements, the powder samples were placed in a glass tube and heated at 420 K under vacuum for 4 hours. Figure 23 shows the corresponding isotherms prepared composites. As shown, all prepared photocatalysts exhibit mesoporous type IV isotherms. High surface area was determined by calculated Brunauer−Emmett−Teller (BET) and recorded as follow; 0.41, 504, 777, 950 and 1054 m^2g^{-1} for $BiNbO_4$, $BiNbO_4/NH_2$-MIL-125(Ti)$_{(75:25)}$, $BiNbO_4/NH_2$-MIL-125(Ti)$_{(50:50)}$, $BiNbO_4/NH_2$-MIL-125(Ti)$_{(25:75)}$ and NH_2-MIL-125(Ti) respectivly, Table 9. The calculated pore volume at the satuation uptake (p/p°=0.95) was found to be 0.0008/0.0009, 0.268/0.269, 0.407/0.408, 0.522/0.524 and 0.562/0.563 cm^3 g^{-1} for $BiNbO_4$, $BiNbO_4/NH_2$-MIL-125(Ti)$_{(75:25)}$, $BiNbO_4/NH_2$-MIL-125(Ti)$_{(50:50)}$, $BiNbO_4/NH_2$-MIL-125(Ti)$_{(25:75)}$ and NH_2-MIL-125(Ti) respectively Table 9. Remarkably, the surface area increased dramatically upon increasing the amount of NH_2-MIL-125(Ti) added.

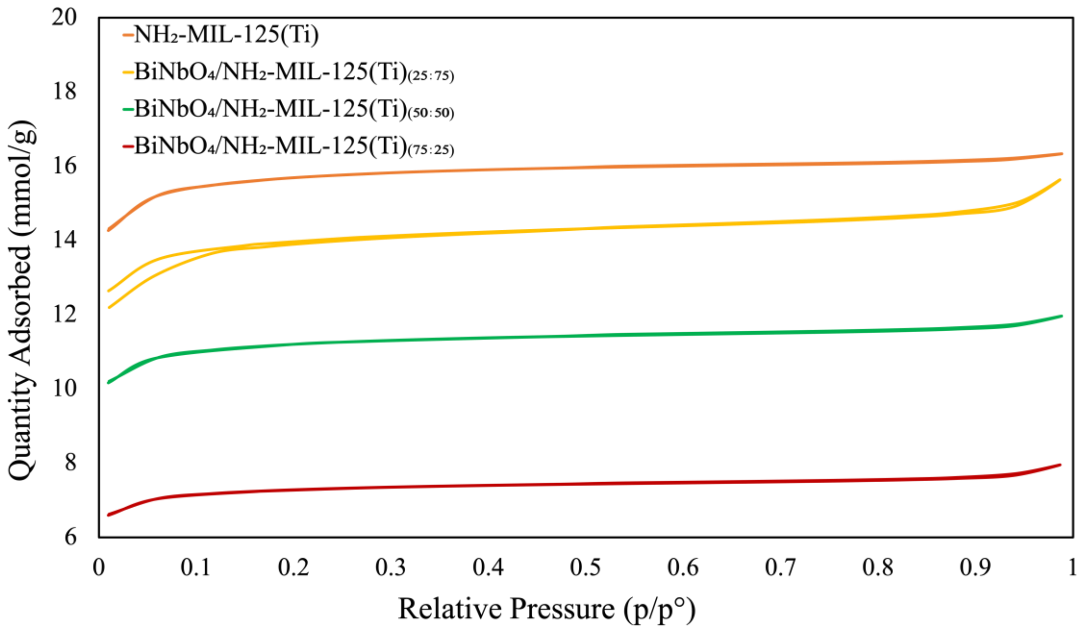

Figure 23: N_2 adsorption isotherm at 77 K. NH_2-MIL-125(Ti), $BiNbO_4/NH_2$-MIL-125(Ti)$_{(25:75)}$, $BiNbO_4/NH_2$-MIL-125(Ti)$_{(50:50)}$ and $BiNbO_4/NH_2$-MIL-125(Ti)$_{(75:25)}$.

4.4 Photocatalytic cycloaddition of CO_2 to propylene oxide

Experimental: The photocatalytic activities of the prepared samples were evaluated using the photocatalytic cycloaddition of carbon dioxide to the propylene oxide. Photocatalytic reactions were carried out in a 75 mL Pyrex sealed tube. In a typical reaction: propylene oxide (100 µl), photocatalyst (50 mg), tetra butyl ammonium bromide ($^{n}Bu_4NBr$, 9 mg) which serves as binary co-catalyst, a mixture of acetonitrile and methanol (6 mL, 5:1 v/v) and carbon dioxide (CO_2, 0.045 mmol) were added to a Pyrex sealed tube. The reaction tube was placed 10 mm away from a 300 W halogen lamp source and kept stirring for 24 hours under constant pressure (1.5 MPa). After 24 hours have elapsed, the excess CO_2 gas was vented, the photocatalyst was filtered out and the excess solvent was evaporated. The desired organic product was then extracted using dichloromethane (DCM) to afford the pure product as confirmed by ^{1}H NMR and ^{13}C NMR (Varian, 400 MHz) and infrared spectroscopy (IR Prestige-21, Shimadzu) between a 500-4000 cm^{-1} frequency range.

Discussion: NH_2-MIL-125(Ti) has many attractive features that makes it a promising candidate as a heterogeneous catalyst. These features include; the accessible titanium metal centers that provides an active Lewis acid site, Brønsted acid sites derived from the amine functionalized terephthalic organic linkers Figure 24, the large surface area and porosity that enhances the substrate diffusion within the large hierarchical pores of the extended reticular structure of NH_2-MIL-125(Ti) and the high CO_2 uptake capacity at the ambient reaction conditions.

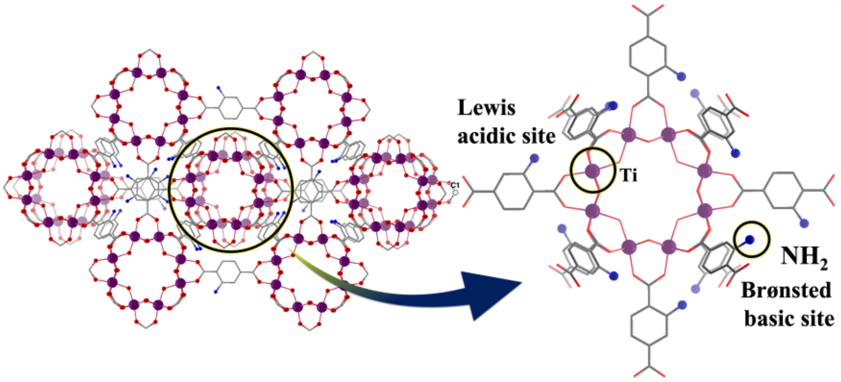

Figure 24: Lewis acidic site at the secondary building unit (SBU) and Brønsted basic site at the amine functionalized NH_2-BDC organic linker of NH_2-MIL-125(Ti).

With these outstanding features, it is of great interest to evaluate the photocatalytic activity of NH_2-MIL-125(Ti) combined with that of $BiNbO_4$ as a heterogeneous visible light photocatalyst for the cycloaddition of CO_2 to propylene oxide. Based on the obtained results, the photoreaction catalyzed by $BiNbO_4$ yielded 40% conversion of cyclic propylene carbonate, this low percent conversion can be attributed to the charge recombination phenomena that was previously discussed in (Chapter 3), and to the conduction band potential that is higher than that needed for

CO_2 radical formation.[172] However, NH_2-MIL-125(Ti) displayed even lower conversion percent, 12% cyclic propylene carbonate. Presumably, this low yield of NH_2-MIL-125(Ti) was partially attributed to the electronic effect of amino group of the functionalized linker. In fact, the amine substitution at the organic linker tend to reduce the Lewis acidity of the metal site, hence, limits the activity of the photocatalyst.[173] Moreover, band gap of NH_2-MIL-125(Ti) is relatively smaller than that of $BiNbO_4$. Therefore, charge recombination is more severe in NH_2-MIL-125(Ti) than it is in $BiNbO_4$. Thus, the formation of an interphase heterojunction is capable of optimizing the band gap potential and suppressing the recombination phenomenon.

In fact, in hybrid composites, enhanced photocatalytic activity was observed upon introducing mixed metal oxide to NH_2-MIL-125(Ti). According to the results, proposed photocatalytic pathway starts with the photoexcitation of electrons to the conduction band at the hybrid system, leaving positive holes at the valance band. The photoexcited electrons at the conduction band of $BiNbO_4$ can transfer to the lowest unoccupied molecular orbital (LUMO) of NH_2-MIL-125(Ti) (reductive sites). In a same manner, the generated positive holes can also transfer to the highest occupied molecular orbital (HOMO) of NH_2-MIL-125(Ti) (oxidative site). Accordingly, Ti^{4+} at the secondary building unit (SBU) of NH_2-MIL-125(Ti) gain electron to form Ti^{3+}.[174] The reduction of metal ion is responsible for the formation of the $CO_2^{\cdot -}$ radicals, resulting in efficient cyclic addition of CO_2 into propylene oxide Figure 25. Methanol acts as a hole scavenger, whereas $^{n}Bu_4NBr$ is a nucleophile used to open the propylene oxide ring. Acetonitrile helps solubilizing CO_2 in the reaction mixture. Apparently, $BiNbO_4$ and NH_2-MIL-125(Ti) heterojunctions provides more efficient electron-hole pairs separation than pure $BiNbO_4$ or NH_2-MIL-125(Ti), hence, enhanced photocatalytic performance. The highest conversion yield of 74% was observed when using $BiNbO_4$/NH_2-MIL-125(Ti) $_{(50:50)}$ composite as photocatalyst. This was attributed to the balance in the system. Since NH_2-MIL-125(Ti) has the more negative potential vs. the standard hydrogen electrode at the LUMO state, it is responsible for the production of CO_2 radicals in excess. However, the activation of the limiting reagent mostly occurs at the valance band of $BiNbO_4$ since it has more positive potential vs. the standard hydrogen electrode. In essence, for this specific reaction, sufficient amount $BiNbO_4$ is needed to activate propylene oxide (the limiting reagent). Notably, using only 25-gram percent of $BiNbO_4$ resulted in a low conversion present comparing to other prepared composites. Amine functionalized NH_2-MIL-125(Ti), on the other hand, provides CO_2 radicals in a sufficient amount and well-balanced manner. Thus, using 50-gram percent of each of the two materials resulted in a high yield. Increasing the amount of NH_2-MIL-125(Ti) added results in a low reaction yield. To ensure the conversion was performed photocatalytically, control experiments was carried out in the dark at the room temperature and only 6% conversion was observed. 10% conversion was obtained at 353 K in the absence of light, and 15% conversion was observed in the absence of the photocatalyst Figure 26, Table 11. Accordingly, it can be concluded that the hybrid materials have better performance than the individual $BiNbO_4$ or NH_2-MIL-125(Ti).

Table 11: Cycloaddition of CO_2 into PO[a] using $BiNbO_4/NH_2$-MIL-125(Ti).

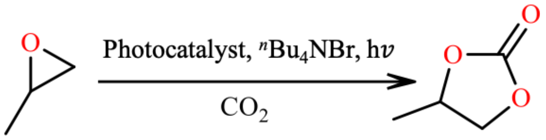

Entry	Photocatalyst	Yield[b] %
1	$BiNbO_4$	40
2	$BiNbO_4/NH_2$-MIL-125(Ti)$_{(75:25)}$	53
3	$BiNbO_4/NH_2$-MIL-125(Ti)$_{(50:50)}$	74
4	$BiNbO_4/NH_2$-MIL-125(Ti)$_{(25:75)}$	40
5	NH_2-MIL-125(Ti)	12
6	No Light	6
7	$^{n}Bu_4NBr$	15
8	Heat	10

[a] Reaction conditions: epoxide (100 µL), photocatalyst (50 mg), $^{n}Bu_4NBr$ (9 mg) and carbon dioxide (1.48 MPa) at 353 K and 24 h

[b] Yield of isolated product was determined by ^{1}H NMR spectroscopy, ^{13}C NMR and FT-IR spectroscopy.

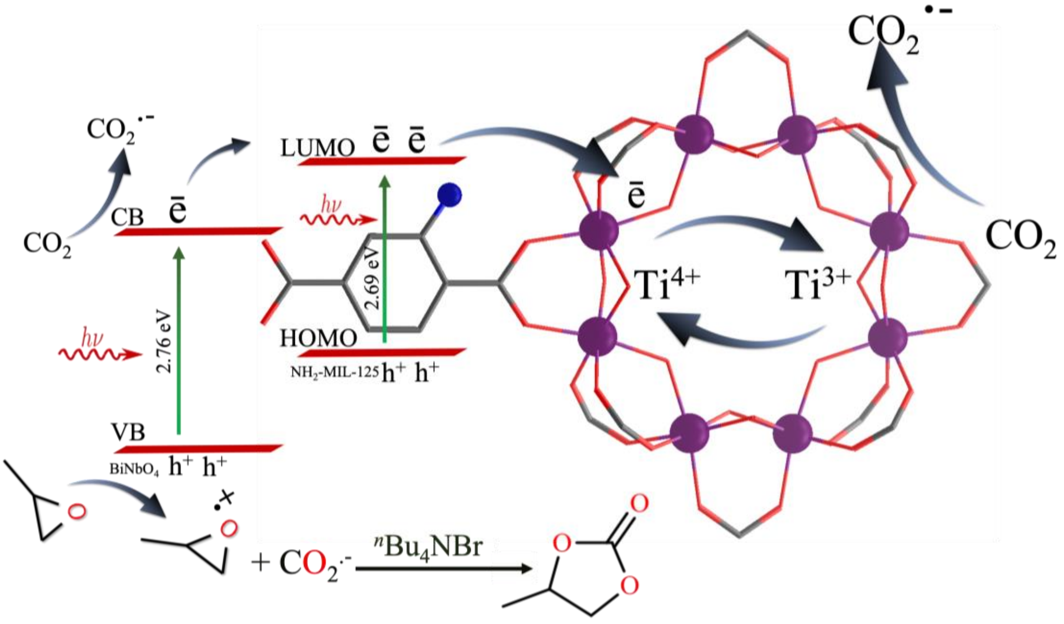

Figure 25: Proposed photocatalytic mechanism. The incident light excites the electrons at the valance band. The exited electrons transfer to the conduction band leaving a positive hole at the valance band. The excited electrons reduce Ti^{4+} to Ti^{3+}. CO_2 radical generate accordingly.

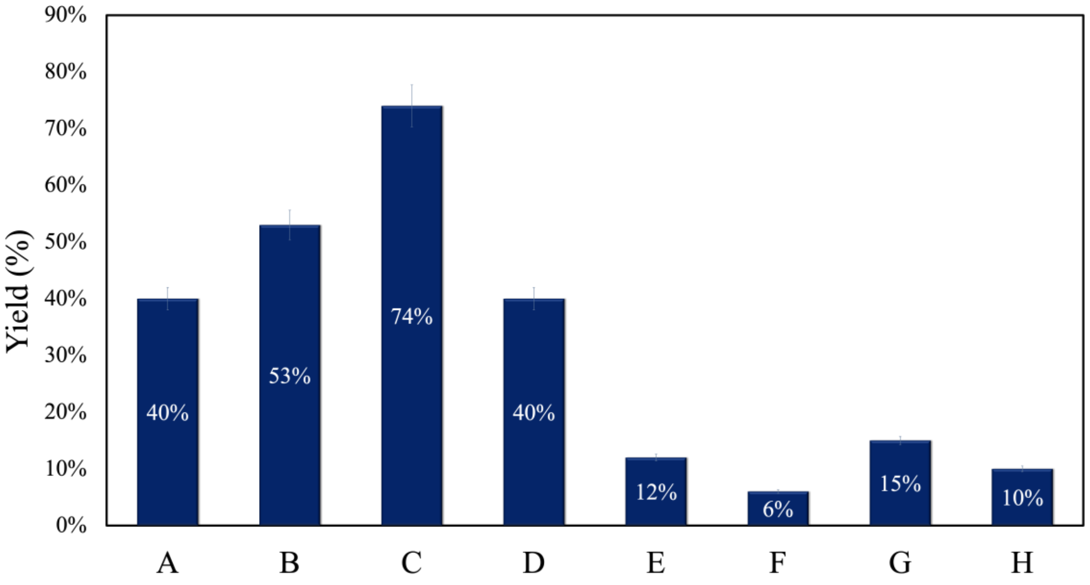

Figure 26: Bar chart represents yield of the obtained cyclic-propylene carbonate.

4.5 Conclusion

$BiNbO_4$/NH_2-MIL-125(Ti) hybrid material was prepared in different ratios. The crystalline structure of the prepared materials was analyzed using PXRD. The heterojunction was established, and the intensity of materials tend to correlate with increasing the amount add. Surface area was calculated using N_2 adsorption isotherm. The surface area and porosity were increased dramatically upon increasing the amount of NH_2-MIL-125(Ti) added. Band gap calculations showed a red shift towards lower energy values upon increasing the amount of NH_2-MIL-125(Ti). The photocatalytic performance of the hybrid materials was found to superior when compared to pure $BiNbO_4$ or NH_2-Mil-125(Ti), with 74% conversion, of an optimum mass ratio of $BiNbO_4$:NH_2-MIL-125, 50:50.

Chapter 5: Conclusion

Towards the aim of preparing active visible light semiconductor photocatalyst $BiNbO_4$ was prepared using different synthetic approaches; co-precipitation, hydrothermal and citrate methods under different calcined temperature values and pH conditions. A mixture of orthorhombic α-$BiNbO_4$ and triclinic β-$BiNbO_4$ was always obtained when calcined the powder at a temperature range from 1023 K to 1173 K respectively. PXRD patterns suggest the co-existence of both phases where preferred phase formation is pH and temperature dependent. When co-precipitation method is used, it was observed that pH plays an important role towards the formation of β-$BiNbO_4$ phase, where high pH promotes a mixture of α- β-$BiNbO_4$ structure, while low pH results in α-$BiNbO_4$ phase. In such a case, $BiNbO_4$ prepared at pH 2 shows the narrowest band gap of 2.86 eV with dominant α-$BiNbO_4$ phase present. Using citrate precursor method, $BiNbO_4$ prepared at pH 7 shows the narrowest band gap of 2.69 eV with dominant α-$BiNbO_4$ phase present, whereas, at acidic or basic conditions wider band gaps >3.0 eV was obtained with dominant β-$BiNbO_4$ phase present. Using hydrothermal approach, $BiNbO_4$ prepared at all pH range of present study show band gap >3.2 eV indicating their absorbance in the UV region. As the calcination temperature increases to 1173 K, a gradual transformation of α- to β was observed. Notably, there is a direct correlation between band gap of prepared photocatalysts and lattice volume; as the lattice volume increases the band gap decreases.

As photocatalyst, $BiNbO_4$ suffers from a charge recombination problem that limits its activity under visible light irradiation. In this regard, to enhance the activity of the $BiNbO_4$, different ratios composites of reduced graphene oxide and $BiNbO_4$ was prepared. As a conductor medium, r-GO’s role is to facilitate the transformation of charge carriers, suppress charge recombination and maintain the photoinduced electron-hole pairs. Hence, enhances the proses of radical formation that are necessary for the photoreaction to proceed. The photo catalytic activity of the prepared materials demonstrated an outstanding photocatalytic activity towards the cycloaddition of CO_2 into propylene oxide under visible light irradiation. The highest conversion percent achieved when using 5% r-GO.

To a certain extent, the activity of mixed metal oxides in general is limited due to their low surface area. Introducing metal organic framework to $BiNbO_4$ enhances the surface uptake capacity of the photocatalytic system. Moreover, it creates a heterojunction that facilitate the light harvesting process. $BiNbO_4$/NH_2-MIL-125(Ti) hybrid materials were prepared in different ratios. The surface area and porosity were increased dramatically upon increasing the amount of NH_2-MIL-125(Ti) added. Red shift towards lower energy values was observed when increasing the amount of NH_2-MIL-125(Ti). The photocatalytic performance of $BiNbO_4$/NH_2-MIL-125(Ti) composites were higher than either $BiNbO_4$ or NH_2-MIL-125(Ti).

References

(1) Sorrell, S. Reducing Energy Demand: A Review of Issues, Challenges and Approaches. *Renew. Sustain. Energy Rev.* 2015, 47, 74–82. DOI: 10.1016/j.rser.2015.03.002.

(2) Parry, M. L.; Canziani, O. F.; Palutikof, J. P.; van der Linden, P. J.; Hanson, C. E., C. Climate Change 2007: Impacts Adaptation and Vulnrbility. Contribution of Working Group II to the Fourth Assessment Report of the Intergovernmental Panel on Climate Change, IPCC, Cambridge University Press: Cambridge, UK, 2007.

(3) Hannah, R.; Roser, M. CO_2 and Greenhouse Gas Emissions, published online at OurWorldInData.org. Retrieved from: https://ourworldindata.org/co2-and-other-greenhouse-gas-emissions (accessed Oct 29, 2019).

(4) George Olah CO_2 to Renewable Methanol Plant, Reykjanes. Retrieved from: https://www.chemicals-technology.com/projects/george-olah-renewable-methanol-plant-iceland/ (accessed Oct 29, 2019).

(5) Asahi Kasei Chemicals. Retrieved from: https://www.asahi-kasei.co.jp/asahi/en/ (accessed Oct 29, 2019).

(6) Yu, J.; Balbuena, P. B. Water Effects on Postcombustion CO_2 Capture in Mg-MOF-74. *J. Phys. Chem. C* 2013, 117 (7), 3383–3388. DOI: 10.1021/jp311118x.

(7) Mason, T. J. Sonochemistry and the Environment – Providing a “Green” Link between Chemistry, Physics and Engineering. *Ultrason. Sonochem.* 2007, 14 (4), 476–483. DOI: 10.1016/j.ultsonch.2006.10.008.

(8) Varma, R. S. Journey on Greener Pathways: From the Use of Alternate Energy Inputs and Benign Reaction Media to Sustainable Applications of Nano-Catalysts in Synthesis and Environmental Remediation. *Green Chem.* 2014, 16 (4), 2027–2041. DOI: 10.1039/C3GC42640H.

(9) Crabtree, G. W.; Lewis, N. S. Solar Energy Conversion. *Phys. Today* 2007, 60 (3), 37–42. DOI: 10.1063/1.2718755.

(10) McCullagh, C.; Skillen, N.; Adams, M.; Robertson, P. K. J. Photocatalytic Reactors for Environmental Remediation: A Review. *J. Chem. Technol. Biotechnol.* 2011, 86 (8), 1002–1017. DOI: 10.1002/jctb.2650.

(11) Liao, L.; Zhang, Q.; Su, Z.; Zhao, Z.; Wang, Y.; Li, Y.; Lu, X.; Wei, D.; Feng, G.; Yu, Q.; et al. Efficient Solar Water-Splitting Using a Nanocrystalline CoO Photocatalyst. *Nat. Nanotechnol.* 2014, 9 (1), 69–73. DOI: 10.1038/nnano.2013.272.

(12) Kuriki, R.; Matsunaga, H.; Nakashima, T.; Wada, K.; Yamakata, A.; Ishitani, O.; Maeda, K. Nature-Inspired, Highly Durable CO_2 Reduction System Consisting of a Binuclear Ruthenium(II) Complex and an Organic Semiconductor Using Visible Light. *J. Am. Chem. Soc.* 2016, 138 (15), 5159–5170. DOI: 10.1021/jacs.6b01997.

(13) Darensbourg, D. J.; Holtcamp, M. W. Catalysts for the Reactions of Epoxides and Carbon Dioxide. *Coord. Chem. Rev.* 1996, 153, 155–174. DOI: 10.1016/0010-8545(95)01232-X.

(14) Inoue, S.; Koinuma, H.; Tsuruta, T. Copolymerization of Carbon Dioxide and Epoxide. *J. Polym. Sci. Part B Polym. Lett.* 1969, 7 (4), 287–292. DOI: 10.1002/pol.1969.110070408.

(15) Buysch, H. J. Carbonic Esters. Ullmann's Encyclopedia of Industrial Chemistry, 1st ed, Wiley & Sons, 2000. DOI: 10.1002/14356007.a05_197.

(16) Bayardon, J.; Holz, J.; Schäffner, B.; Andrushko, V.; Verevkin, S.; Preetz, A.; Börner, A. Propylene Carbonate as a Solvent for Asymmetric Hydrogenations. *Angew. Chemie Int. Ed.* 2007, 46 (31), 5971–5974. DOI: 10.1002/anie.200700990.

(17) Li, X. H.; Meng, Y. Z.; Wang, S. J.; Rajulu, A. V.; Tjong, S. C. Completely Biodegradable Composites of Poly(Propylene Carbonate) and Short, Lignocellulose Fiber Hildegardia Populifolia. *J. Polym. Sci. Part B Polym. Phys.* 2004, 42 (4), 666–675. DOI: 10.1002/polb.10761.

(18) Duval, A.; Avérous, L. Oxyalkylation of Condensed Tannin with Propylene Carbonate as an Alternative to Propylene Oxide. *ACS Sustain. Chem. Eng.* 2016, 4 (6), 3103–3112. DOI: 10.1021/acssuschemeng.6b00081.

(19) Chernyak, Y. Dielectric Constant, Dipole Moment, and Solubility Parameters of Some Cyclic Acid Esters. *J. Chem. Eng. Data* 2006, 51 (2), 416–418. DOI: 10.1021/je050341y.

(20) Chai, J.; Liu, Z.; Zhang, J.; Sun, J.; Tian, Z.; Ji, Y.; Tang, K.; Zhou, X.; Cui, G. A Superior Polymer Electrolyte with Rigid Cyclic Carbonate Backbone for Rechargeable Lithium Ion Batteries. *ACS Appl. Mater. Interfaces* 2017, 9 (21), 17897–17905. DOI: 10.1021/acsami.7b02844.

(21) Hoffmann, M. R.; Martin, S. T.; Choi, W.; Bahnemann, D. W. Environmental Applications of Semiconductor Photocatalysis. *Chem. Rev.* 1995, 95 (1), 69–96. DOI: 10.1021/cr00033a004.

(22) Anandan, S.; Ikuma, Y.; Niwa, K. An Overview of Semi-Conductor Photocatalysis: Modification of TiO_2 Nanomaterials. *Solid State Phenom.* 2010, 162, 239–260. DOI: 10.4028/www.scientific.net/SSP.162.239.

(23) Shan, A. Y.; Ghazi, T. I. M.; Rashid, S. A. Immobilisation of Titanium Dioxide onto Supporting Materials in Heterogeneous Photocatalysis: A Review. *Appl. Catal. A Gen.* 2010, 389 (1), 1–8. DOI: 10.1016/j.apcata.2010.08.053.

(24) Huang, Z. F.; Pan, L.; Zou, J. J.; Zhang, X.; Wang, L. Nanostructured Bismuth Vanadate-Based Materials for Solar-Energy-Driven Water Oxidation: A Review on Recent Progress. *Nanoscale* 2014, 6 (23), 14044–14063. DOI: 10.1039/C4NR05245E.

(25) Subramanian, V.; Wolf, E.; Kamat, P. V. Semiconductor−Metal Composite Nanostructures. To What Extent Do Metal Nanoparticles Improve the Photocatalytic Activity of TiO_2 Films? *J. Phys. Chem. B* 2001, 105 (46), 11439–11446. DOI: 10.1021/jp011118k.

(26) Fujishima, A.; Honda, K. Electrochemical Photolysis of Water at a Semiconductor Electrode. *Nature* 1972, 238, 37-38. DOI: 10.1038/238037a0.

(27) Dong, H.; Zeng, G.; Tang, L.; Fan, C.; Zhang, C.; He, X.; He, Y. An Overview on Limitations of TiO_2-Based Particles for Photocatalytic Degradation of Organic Pollutants and the Corresponding Countermeasures. *Water Res.* 2015, 79, 128–146. DOI: 10.1016/j.watres.2015.04.038.

(28) Yang, Y.; Javed, H.; Zhang, D.; Li, D.; Kamath, R.; McVey, K.; Sra, K.; Alvarez, P. J. J. Merits and Limitations of TiO_2-Based Photocatalytic Pretreatment of Soils Impacted by Crude Oil for Expediting Bioremediation. Front. *Chem. Sci. Eng*. 2017, 11 (3), 387–394. DOI: 10.1007/s11705-017-1657-8.

(29) Pelaez, M.; Nolan, N. T.; Pillai, S. C.; Seery, M. K.; Falaras, P.; Kontos, A. G.; Dunlop, P. S. M.; Hamilton, J. W. J.; Byrne, J. A.; O'Shea, K.; et al. A Review on the Visible Light Active Titanium Dioxide Photocatalysts for Environmental Applications. *Appl. Catal. B Environ.* 2012, 125, 331–349. DOI: 10.1016/j.apcatb.2012.05.036.

(30) Adhikari, S. P.; Hood, Z. D.; More, K. L.; Ivanov, I.; Zhang, L.; Gross, M.; Lachgar, A. Visible Light Assisted Photocatalytic Hydrogen Generation by Ta_2O_5/Bi_2O_3, $TaON/Bi_2O_3$, and Ta_3N_5/Bi_2O_3 Composites. *RSC Adv.* 2015, 5 (68), 54998–55005. DOI: 10.1039/C5RA06563A.

(31) Adhikari, S. P.; Dean, H.; Hood, Z. D.; Peng, R.; More, K. L.; Ivanov, I.; Wu, Z.; Lachgar, A. Visible-Light-Driven Bi_2O_3/WO_3 Composites with Enhanced Photocatalytic Activity. *RSC Adv.* 2015, 5 (111), 91094–91102. DOI: 10.1039/C5RA13579F.

(32) Martin, S. T.; Morrison, C. L.; Hoffmann, M. R. Photochemical Mechanism of Size-Quantized Vanadium-Doped TiO_2 Particles. *J. Phys. Chem.* 1994, 98 (51), 13695–13704. DOI: 10.1021/j100102a041.

(33) Burda, C.; Lou, Y.; Chen, X.; Samia, A. C. S.; Stout, J.; Gole, J. L. Enhanced Nitrogen Doping in TiO_2 Nanoparticles. *Nano Lett.* 2003, 3 (8), 1049–1051. DOI: 10.1021/nl034332o.

(34) Fukahori, S.; Ichiura, H.; Kitaoka, T.; Tanaka, H. Photocatalytic Decomposition of Bisphenol A in Water Using Composite TiO_2-Zeolite Sheets Prepared by a Papermaking Technique. *Environ. Sci. Technol.* 2003, 37 (5), 1048–1051. DOI: 10.1021/es0260115.

(35) Pahalagedara, M. N.; Pahalagedara, L. R.; Kuo, C. H.; Dharmarathna, S.; Suib, S. L. Ordered Mesoporous Mixed Metal Oxides: Remarkable Effect of Pore Size on Catalytic Activity. *Langmuir* 2014, 30 (27), 8228–8237. DOI: 10.1021/la502190b.

(36) Yuan, C.; Wu, H. Bin; Xie, Y.; Lou, X. W. Mixed Transition-Metal Oxides: Design, Synthesis, and Energy-Related Applications. *Angew. Chemie - Int. Ed.* 2014, 53 (6), 1488–1504. DOI: 10.1002/anie.201303971.

(37) Zhou, Y. X.; Yao, H. Bin; Zhang, Q.; Gong, J. Y.; Liu, S. J.; Yu, S. H. Hierarchical $FeWO_4$ Microcrystals: Solvothermal Synthesis and Their Photocatalytic and Magnetic Properties. *Inorg. Chem.* 2009, 48 (3), 1082–1090. DOI: 10.1021/ic801806r.

(38) Tan, F. K.; Hassan, J.; Wahab, Z. A.; Azis, R. S. Electrical Conductivity and Dielectric Behaviour of Manganese and Vanadium Mixed Oxide Prepared by Conventional Solid State Method. *Eng. Sci. Technol. an Int. J.* 2016, 19 (4), 2081–2087. DOI: 10.1016/j.jestch.2016.08.002.

(39) Shang, M.; Wang, W.; Ren, J.; Sun, S.; Zhang, L. A Novel $BiVO_4$ Hierarchical Nanostructure: Controllable Synthesis, Growth Mechanism, and Application in Photocatalysis. *CrystEngComm.* 2010, 12 (6), 1754–1758. DOI: 10.1039/B923115C.

(40) Arora, A. K.; Jaswal, V. S.; Singh, K.; Singh, R. Department of Economic and Social Affairs - World Urbanization Prospects. *Orient. J. Chem.* 2016, 32 (4), 2035–2042. DOI: 10.13005/ojc/320430.

(41) Gawande, M. B.; Pandey, R. K.; Jayaram, R. V. Role of Mixed Metal Oxides in Catalysis Science - Versatile Applications in Organic Synthesis. *Catal. Sci. Technol.* 2012, 2 (6), 1113–1125. DOI: 10.1039/c2cy00490a.

(42) Mao, N.; Jiao, Y. CuAl Hydrotalcite Formed CuAl-Mixed Metal Oxides for Photocatalytic Removal of Rhodamine B and Cr(VI). *Chemistry Select* 2018, 3 (44), 12676–12681. DOI: 10.1002/slct.201801888.

(43) Arora, A. K.; Jaswal, V. S.; Singh, K.; Singh, R. Applications of Metal/Mixed Metal Oxides as Photocatalyst: A Review. *Orient. J. Chem.* 2016, 32 (4), 2035–2042. DOI: 10.13005/ojc/320430.

(44) Su, J.; Guo, L.; Bao, N.; Grimes, C. A. Nanostructured $WO_3/BiVO_4$ Heterojunction Films for Efficient Photoelectrochemical Water Splitting. *Nano Lett.* 2011, 11 (5), 1928–1933. DOI: 10.1021/nl2000743.

(45) Rodriguez, J. A. Electronic and Chemical Properties of Mixed-Metal Oxides: Basic Principles for the Design of DeNOx and DeSOx Catalysts. *Catal. Today* 2003, 85 (2–4), 177–192. DOI: 10.1016/S0920-5861(03)00385-7.

(46) Cui, H.; Zayat, M.; Levy, D. Sol-Gel Synthesis of Nanoscaled Spinels Using Propylene Oxide as a Gelation Agent. *J. Sol-Gel Sci. Technol.* 2005, 35 (3), 175–181. DOI: 10.1007/s10971-005-4165-0.

(47) Elia, A.; Aispuro, P. M.; Quaranta, N.; Martín-Martínez, J. M.; Vázquez, P. Synthesis and Characterization of New Silica-Titania Mixed Oxides Obtained by Sol-Gel Technique. *Macromol. Symp.* 2011, 301 (1), 136–145. DOI: 10.1002/masy.201150317.

(48) Gawande, M. B.; Branco, P. S.; Parghi, K.; Shrikhande, J. J.; Pandey, R. K.; Ghumman, C. A. A.; Bundaleski, N.; Teodoro, O. M. N. D.; Jayaram, R. V. Synthesis and Characterization of Versatile $MgO\text{-}ZrO_2$ Mixed Metal Oxide Nanoparticles and Their Applications. *Catal. Sci. Technol.* 2011, 1 (9), 1653–1664. DOI: 10.1039/c1cy00259g.

(49) Sheets, W. C.; Stampler, E. S.; Kabbour, H.; Bertoni, M. I.; Cario, L.; Mason, T. O.; Marks, T. J.; Poeppelmeier, K. R. Facile Synthesis of BiCuOS by Hydrothermal Methods. *Inorg. Chem.* 2007, 46 (25), 2333–2335. DOI: 10.1021/ic7014622.

(50) Zyryanov, V. V. Mechanochemical Synthesis and Thermal Behavior of Metastable Mixed Oxides in the $CaO\text{-}Sb_2O_3\text{-}Bi_2O_3$ System. *Inorg. Mater.* 2003, 39 (11), 1163–1171. DOI: 10.1023/A:1027301626107.

(51) Cooper, J. K.; Gul, S.; Toma, F. M.; Chen, L.; Glans, P. A.; Guo, J.; Ager, J. W.; Yano, J.; Sharp, I. D. Electronic Structure of Monoclinic $BiVO_4$. *Chem. Mater.* 2014, 26 (18), 5365–5373. DOI: 10.1021/cm5025074.

(52) Saison, T.; Chemin, N.; Chanéac, C.; Durupthy, O.; Mariey, L.; Maugé, F.; Brezová, V.; Jolivet, J. P. New Insights Into $BiVO_4$ Properties as Visible Light Photocatalyst. *J. Phys. Chem. C* 2015, 119 (23), 12967–12977. DOI: 10.1021/acs.jpcc.5b01468.

(53) Jing, Q.; Feng, X.; Zhao, X.; Duan, Z.; Pan, J.; Chen, L.; Liu, Y. Bi/$BiVO_4$ Chainlike Hollow Microstructures: Synthesis, Characterization, and Application as Visible-Light-Active Photocatalysts. *ACS Appl. Nano Mater.* 2018, 1 (6), 2653–2661. DOI: 10.1021/acsanm.8b00330.

(54) Bierlein, J. D.; Sleight, A. W. Ferroelasticity in $BiVO_4$. *Solid State Commun.* 1975, 16 (1), 69–70. DOI: 10.1016/0038-1098(75)90791-7.

(55) Lim, R. L.; Choh, S. H.; Jang, M. S. Prominent Ferroelastic Domain Walls in $BiVO_4$ Crystal. *J. Phys. Condens. Matter* 1995, 7 (37), 7309-7323. DOI: 10.1088/0953-8984/7/37/005.

(56) Manolikas, C.; Amelinckx, S. Ferroelastic Domains in $BiVO_4$. *Phys. status solidi* 1980, 60 (1), 167–172. DOI:10.1002/pssa.2210600120.

(57) Hirota, K.; Komatsu, G.; Yamashita, M.; Takemura, H.; Yamaguchi, O. Formation, Characterization and Sintering of Alkoxy-Derived Bismuth Vanadate. *Mater. Res. Bull.* 1992, 27 (7), 823–830. DOI: 10.1016/0025-5408(92)90177-2.

(58) Pinczuk, A.; Welber, B.; Dacol, F. H. Mechanism of the Ferroelastic Transition of $BiVO_4$. *Solid State Commun.* 1979, 29 (7), 515–518. DOI: 10.1016/0038-1098(79)90347-8.

(59) Sayama, K.; Nomura, A.; Arai, T.; Sugita, T.; Abe, R.; Yanagida, M.; Oi, T.; Iwasaki, Y.; Abe, Y.; Sugihara, H. Photoelectrochemical Decomposition of Water into H_2 and O_2 on Porous $BiVO_4$ Thin-Film Electrodes under Visible Light and Significant Effect of Ag Ion Treatment. *J. Phys. Chem. B* 2006, 110 (23), 11352–11360. DOI: 10.1021/jp057539+.

(60) Luo, H.; Mueller, A. H.; McCleskey, T. M.; Burrell, A. K.; Bauer, E.; Jia, Q. X. Structural and Photoelectrochemical Properties of $BiVO_4$ Thin Films. *J. Phys. Chem. C* 2008, 112 (15), 6099–6102. DOI: 10.1021/jp7113187.

(61) Kudo, A.; Omori, K.; Kato, H. A Novel Aqueous Process for Preparation of Crystal Form-Controlled and Highly Crystalline $BiVO_4$ Powder from Layered Vanadates at Room Temperature and Its Photocatalytic and Photophysical Properties. *J. Am. Chem. Soc.* 1999, 121 (49), 11459–11467. DOI: 10.1021/ja992541y.

(62) Ding, K.; Chen, B.; Li, Y.; Zhang, Y.; Chen, Z. Comparative Density Functional Theory Study on the Electronic and Optical Properties of $BiMO_4$ (M = V, Nb, Ta). *J. Mater. Chem. A* 2014, 2 (22), 8294-8303. DOI: 10.1039/c3ta15367c.

(63) Frost, R. L.; Henry, D. A.; Weier, M. L.; Martens, W. Raman Spectroscopy of Three Polymorphs of $BiVO_4$: Clinobisvanite, Dreyerite and Pucherite, with Comparisons to $(VO_4)_3$-Bearing Minerals: Namibite, Pottsite and Schumacherite. *J. Raman Spectrosc.* 2006, 37 (7), 722–732. DOI: 10.1002/jrs.1499.

(64) Walsh, A.; Yan, Y.; Huda, M. N.; Al-Jassim, M. M.; Wei, S. H. Band Edge Electronic Structure of $BiVO_4$: Elucidating the Role of the Bi s and V d Orbitals. *Chem. Mater.* 2009, 21 (3), 547–551. DOI: 10.1021/cm802894z.

(65) Rao, K. S.; Buddhudu, S. Structural, Thermal and Dielectric Properties of $BiNbO_4$ Ceramic Powder. *Ferroelectr. Lett. Sect.* 2010, 37 (6), 101–109. DOI: 10.1080/07315171.2010.527806.

(66) Babu, R.; Kelkar, S.; Kashid, V.; Achary, S. N.; Salunke, H. G.; Gupta, N. M. Photophysical, Bandstructural, and Textural Properties of o-$FeNbO_4$ in Relation to Its Cocatalyst-Assisted Photoactivity for Water Oxidation. *RSC Adv.* 2014, 4 (63), 33435–33445. DOI: 10.1039/c4ra06059h.

(67) Dunkle, S. S.; Suslick, K. S. Photodegradation of $BiNbO_4$ Powder during Photocatalytic Reactions. *Scanning* 2009, 113, 1031–10345. DOI: 10.1021/jp903163u

(68) Aurivillius, B. X-Ray Investigations on $BiNbO_4$, $BiTaO_4$ and $BiSbO_4$. *Ark. Kemi* 1951, 3 (2–3), 153–161. Retrieved from: https://scifinder.cas.org/scifinder/view/scifinder/scifinderExplore.jsf (accessed Oct 29, 2019).

(69) Roth, R. S.; Waring, J. L. Phase Equilibrium Relations in the Binary System Bismuth Sesquioxide-Niobium Pentoxide. *J. Res. Natl. Bur. Stand. Sect. A Phys. Chem.* 1962, 66A (6), 451–463. DOI: 10.6028/jres.066A.046.

(70) Diehl, R.; Carpentier, C. The Crystal Structure of Triclinic β-$BiNbO_4$. *Acta Crystallogr.* 1973, B34, 1105–1111. DOI: 10.1107/S0567740878005014.

(71) Popolitov, V. I.; Ivanova, L. A.; Stephanovitch, S. Y.; Chetchkin, V. V.; Lobachev, A. N.; Venevtsev, Y. N. Ferroelectrics ABO_4: Synthesis of Single Crystals and Ceramics; Dielectric and Nonlinear Optical Properties. *Ferroelectrics* 1974, 8 (1), 519–520. DOI: 10.1080/00150197408234145.

(72) Subramanian, M. A.; Calabrese, J. C. Crystal Structure of The Low Temperature Form of Bismuth Niobium Oxide [α-$BiNbO_4$]. *Mater. Res. Bull.* 1993, 28 (c), 523–529. DOI: 10.1016/0025-5408(93)90048-I.

(73) Zhou, D.; Wang, H.; Yao, X.; Wei, X.; Xiang, F.; Pang, L. Phase Transformation in $BiNbO_4$ Ceramics. *Appl. Phys. Lett.* 2007, 90 (17), 172910. DOI: 10.1063/1.2732833.

(74) Zhai, H. F.; Qian, X.; Kong, J. Z.; Li, A. D.; Gong, Y. P.; Li, H.; Wu, D. Abnormal Phase Transition in $BiNbO_4$ Powders Prepared by a Citrate Method. *J. Alloys Compd.* 2011, 509 (42), 10230–10233. DOI: 10.1016/j.jallcom.2011.08.077.

(75) Zhai, H. F.; Li, A. D.; Kong, J. Z.; Li, X. F.; Zhao, J.; Guo, B. L.; Yin, J.; Li, Z. S.; Wu, D. Preparation and Visible-Light Photocatalytic Properties of $BiNbO_4$ and $BiTaO_4$ by a Citrate Method. *J. Solid State Chem.* 2013, 202, 6–14. DOI: 10.1016/j.jssc.2013.03.012.

(76) Xu, C.; He, D.; Liu, C.; Wang, H.; Zhang, L.; Wang, P.; Yin, S. High Pressure and High Temperature Study the Phase Transitions of $BiNbO_4$. *Solid State Commun.* 2013, 156, 21–24. DOI: 10.1016/j.ssc.2012.11.007.

(77) Zhou, D.; Xu, C.; He, D. W.; Fu, M. Sen; Guo, J.; Zhou, H. F.; Pang, L. X.; Yao, X. Dielectric Properties and Phase Transitions of $BiNbO_4$ Ceramic. *Scr. Mater.* 2014, 81, 40–43. DOI: 10.1016/j.scriptamat.2014.02.022.

(78) Zou, Z.; Arakawa, H.; Ye, J. Substitution Effect of Ta^{5+} by Nb^{5+} on Photocatalytic, Photophysical, and Structural Properties of BiTa1-x NbxO4 ($0≦x≦1$). *J. Mater. Res.* 2002, 17 (6), 1446–1454. DOI: 10.1557/JMR.2002.0215

(79) Zou, Z.; Ye, J.; Arakawa, H. Photocatalytic Water Splitting into H_2 and/or O_2 under UV and Visible Light Irradiation with a Semiconductor Photocatalyst. *Int. J. Hydrogen Energy* 2003, 28 (6), 663–669. DOI: 10.1016/S0360-3199(02)00159-3.

(80) Zou, Z.; Ye, J.; Arakawa, H. Optical and Structural Properties of the BiTa1−xNbxO4 ($0≦x≦1$) Compounds. *Solid State Commun.* 2001, 119 (7), 471–475. DOI: 10.1016/S0038-1098(01)00250-2.

(81) Wiegel, M.; Middel, W.; Blasse, G. Influence of Ns^2 Ions on the Luminescence of Niobates and Tantalates. *J. Mater. Chem.* 1995, 5 (7), 981–983. DOI: 10.1039/jm9950500981.

(82) Lee, C. Y.; Macquart, R.; Zhou, Q.; Kennedy, B. J. Structural and Spectroscopic Studies of BiTa1− XNbxO4. *J. Solid State Chem.* 2003, 174 (2), 310–318. DOI: 10.1016/S0022-4596(03)00225-1

(83) Maruyama, Y.; Izawa, C.; Watanabe, T. Synthesis of $BiNbO_4$ by the Flux Method. *ISRN Mater. Sci.* 2012, 2012, 1–5. DOI: 10.5402/2012/170362.

(84) Morrison, S. R. Electrochemistry at Semiconductor and Oxidized Metal Electrodes; Springer US, Plenum Press: New York, 1980.

(85) Pleskov, Y. V.; Gurevich, Y. Y. Semiconductor Photoelectrochemistry; Springer US, Consultants Bureau: New York, 1986.

(86) Li, M.; Li, F.; Yin, P. G. Tailoring the Band Structure of β-Bi_2O_3 by Co-Doping for Realized Photocatalytic Hydrogen Generation. *Chem. Phys. Lett.* 2014, 601, 92–97. DOI: 10.1016/j.cplett.2014.03.091.

(87) Hoffeditz, W. L.; Pellin, M. J.; Farha, O. K.; Hupp, J. T. Determining the Conduction Band-Edge Potential of Solar-Cell-Relevant Nb_2O_5 Fabricated by Atomic Layer Deposition. *Langmuir* 2017, 33 (37), 9298–9306. DOI: 10.1021/acs.langmuir.7b00683.

(88) Yu, Z.; Waclawik, E. R.; Wang, Z.; Gu, X.; Yuan, Y.; Zheng, Z. Dual Modification of $TiNb_2O_7$ with Nitrogen Dopants and Oxygen Vacancies for Selective Aerobic Oxidation of Benzylamine to Imine under Green Light. *J. Mater. Chem.* A 2017, 5 (9), 4607–4615. DOI: 10.1039/C6TA11061D.

(89) Jović, V. D.; Jović, B. M. Semiconducting Properties of Oxide Films Formed onto an Nb Electrode in NaOH Solutions. *J. Serbian Chem. Soc.* 2008, 73 (3), 351–367. DOI: 10.2298/JSC0803351J.

(90) Yu, H.; Xiao, P.; Tian, J.; Wang, F.; Yu, J. Phenylamine-Functionalized RGO/TiO_2 Photocatalysts: Spatially Separated Adsorption Sites and Tunable Photocatalytic Selectivity. *ACS Appl. Mater. Interfaces* 2016, 8 (43), 29470–29477. DOI: 10.1021/acsami.6b09903.

(91) Yaghi, O. M.; O'Keeffe, M.; Ockwig, N. W.; Chae, H. K.; Eddaoudi, M.; Kim, J. Reticular Synthesis and the Design of New Materials. *Nature* 2003, 423 (6941), 705–714. DOI: 10.1038/nature01650.

(92) Li, H.; Eddaoudi, M.; O'Keeffe, M.; Yaghi, O. M. Design and Synthesis of an Exceptionally Stable and Highly Porous Metal-Organic Framework. *Nature* 1999, 402, 276–279. DOI: 10.1038/46248.

(93) Furukawa, H.; Cordova, K. E.; O'Keeffe, M.; Yaghi, O. M. The Chemistry and Applications of Metal-Organic Frameworks. *Sci.* 2013, 341 (6149), 1230444. DOI: 10.1126/science.1230444.

(94) Vikrant, K.; Kumar, V.; Kim, K. H.; Kukkar, D. Metal–Organic Frameworks (MOFs): Potential and Challenges for Capture and Abatement of Ammonia. *J. Mater. Chem. A* 2017, 5 (44), 22877–22896. DOI: 10.1039/C7TA07847A.

(95) Hendon, C. H.; Rieth, A. J.; Korzyński, M. D.; Dincă, M. Grand Challenges and Future Opportunities for Metal–Organic Frameworks. *ACS Cent. Sci.* 2017, 3 (6), 554–563. DOI: 10.1021/acscentsci.7b00197.

(96) Liu, J. J.; Shan, Y. B.; Fan, C. R.; Lin, M. J.; Huang, C. C.; Dai, W. X. Encapsulating Naphthalene in an Electron-Deficient MOF to Enhance Fluorescence for Organic Amines Sensing. *Inorg. Chem.* 2016, 55 (7), 3680–3684. DOI: 10.1021/acs.inorgchem.6b00252.

(97) Senkovska, I.; Kaskel, S. Ultrahigh Porosity in Mesoporous MOFs: Promises and Limitations. *Chem. Commun.* 2014, 50 (54), 7089–7098. DOI: 10.1039/C4CC00524D.

(98) Yang, Q.; Liu, W.; Wang, B.; Zhang, W.; Zeng, X.; Zhang, C.; Qin, Y.; Sun, X.; Wu, T.; Liu, J.; Huo, F.; Lu, J. Regulating the Spatial Distribution of Metal Nanoparticles within Metal-Organic Frameworks to Enhance Catalytic Efficiency. *Nat. Commun.* 2017, 8 (1), 14429. DOI: 10.1038/ncomms14429.

(99) Dan-Hardi, M.; Serre, C.; Frot, T.; Rozes, L.; Maurin, G.; Sanchez, C.; Férey, G. A New Photoactive Crystalline Highly Porous Titanium(IV) Dicarboxylate. *J. Am. Chem. Soc.* 2009, 131 (31), 10857–10859. DOI: 10.1021/ja903726m.

(100) Hendon, C. H.; Tiana, D.; Fontecave, M.; Sanchez, C.; D'arras, L.; Sassoye, C.; Rozes, L.; Mellot-Draznieks, C.; Walsh, A. Engineering the Optical Response of the Titanium-MIL-125 Metal–Organic Framework through Ligand Functionalization. *J. Am. Chem. Soc.* 2013, 135 (30), 10942–10945. DOI: 10.1021/ja405350u.

(101) Logan, M. W.; Ayad, S.; Adamson, J. D.; Dilbeck, T.; Hanson, K.; Uribe-Romo, F. J. Systematic Variation of the Optical Bandgap in Titanium Based Isoreticular Metal–Organic Frameworks for Photocatalytic Reduction of CO_2 under Blue Light. *J. Mater. Chem. A* 2017, 5 (23), 11854–11863. DOI: 10.1039/C7TA00437K.

(102) Kim, S. N.; Kim, J.; Kim, H. Y.; Cho, H. Y.; Ahn, W. S. Adsorption/Catalytic Properties of MIL-125 and NH_2-MIL-125. *Catal. Today* 2013, 204, 85–93. DOI: 10.1016/j.cattod.2012.08.014.

(103) Chamorro, J. R.; McQueen, T. M. Progress toward Solid State Synthesis by Design. *Acc. Chem. Res.* 2018, 51 (11), 2918–2925. DOI: 10.1021/acs.accounts.8b00382.

(104) Davarpanah, A. M.; Mirzae, A. A.; Sargazi, M.; Feizi, M. Magnetic Properties of Fe-Ni Nanoparticles Prepared by Co-Precipitation Method. *J. Phys. Conf. Ser.* 2008, 126-130. DOI: 10.1088/1742-6596/126/1/012065.

(105) Adair, J. H.; Suvaci, E. Submicron Electroceramic Powders by Hydrothermal Synthesis. Encycl. *Mater. Sci. Technol.* 2001, 1–5. DOI: 10.1016/b0-08-043152-6/01607-7.

(106) Kumar, H.; Manisha; Sangwan, P. Synthesis and Characterization of MnO_2 Nanoparticles Using Co-Precipitation Technique. *Int. J. Chem. Chem. Eng.* 2013, 3 (3), 155–160. Retrieved from: https://www.ripublication.com/ijcce_spl/ijccev3n3spl_05.pdf (accessed Oct 29, 2019).

(107) Wang, H.; Xu, X.; Zhang, J.; Li, C. A Cost-Effective Co-Precipitation Method for Synthesizing Indium Tin Oxide Nanoparticles without Chlorine Contamination. *J. Mater. Sci. Technol.* 2010, 26 (11), 1037–1040. DOI: 10.1016/S1005-0302(10)60171-5.

(108) Lu, B. Y.; Zhang, D.; Sheng, W. Solubility Enhancement in Supercritical Solvents. *Pure Appl. Chem.* 2009, 62 (12), 2277–2285. DOI: 10.1351/pac199062122277.

(109) Wang, F.; Liu, X. Rare-Earth Doped Upconversion Nanophosphors. *Compr. Nanosci. Technol.* 2010, 1–5, 607–635. DOI: 10.1016/B978-0-12-374396-1.00146-X.

(110) Ramimoghadam, D.; Hussein, M. Z. Bin; Taufiq-Yap, Y. H. The Effect of Sodium Dodecyl Sulfate (SDS) and Cetyltrimethylammonium Bromide (CTAB) on the Properties of ZnO Synthesized by Hydrothermal Method. *Int. J. Mol. Sci.* 2012, 13 (10), 13275–13293. DOI: 10.3390/ijms131013275.

(111) Pechini, M. P. Method of Preparing Lead and Alkaline Earth Titanates and Niobates and Coating Method Using the Same to Form a Capacitor. U.S. Patent 3,330,697, July 11, 1967.

(112) Eror, N. G.; Anderson, H. U. Polymeric Precursor Synthesis of Ceramic Materials. *MRS Proc.* 1986, 73, 571-577. DOI: 10.1557/PROC-73-571.

(113) Zhou, D.; Wang, H.; Yao, X.; Wei, X.; Xiang, F.; Pang, L. Phase Transformation in $BiNbO_4$ Ceramics. *Appl. Phys. Lett.* 2007, 90 (17), 2005–2008. DOI: 10.1063/1.2732833.

(114) Devesa, S.; Graça, M. P.; Costa, L. C. Structural, Morphological and Dielectric Properties of $BiNbO_4$ Ceramics Prepared by the Sol-Gel Method. *Mater. Res. Bull.* 2016, 78 (3), 128–133. DOI: 10.1016/j.materresbull.2016.02.035.

(115) Liou, Y. C.; Tsai, W. C.; Chen, H. M. Low-Temperature Synthesis of $BiNbO_4$ Ceramics Using Reaction-Sintering Process. *Ceram. Int.* 2009, 35 (6), 2119–2122. DOI: 10.1016/j.ceramint.2008.11.030.

(116) Pourmand, M.; Mohammadizadeh, M. R. Influence of Temperature on TiO_2 Nanoparticles. *Curr. Nanosci.* 2008, 4 (2), 151–156. DOI: 10.2174/157341308784340859.

(117) Ali, W.; Ullah, H.; Zada, A.; Alamgir, M. K.; Muhammad, W.; Ahmad, M. J.; Nadhman, A. Effect of Calcination Temperature on the Photoactivities of ZnO/SnO_2 Nanocomposites for the Degradation of Methyl Orange. *Mater. Chem. Phys.* 2018, 213, 259–266. DOI: 10.1016/j.matchemphys.2018.04.015.

(118) Wan, Y.; Wang, S.; Luo, W.; Zhao, L. Impact of Preparative PH on the Morphology and Photocatalytic Activity of $BiVO_4$. *Int. J. Photoenergy* 2012, 2012, 1-7. DOI: 10.1155/2012/392865.

(119) Radha, R.; Gupta, U. N.; Samuel, V.; Muthurajan, H.; Kumar, H. H.; Ravi, V. A Co-Precipitation Technique to Prepare $BiNbO_4$ Powders. *Ceram. Int.* 2008, 34 (6), 1565–1567. DOI: 10.1016/j.ceramint.2007.03.022.

(120) Schreiner, W. N. A Standard Test Method for the Determination of RIR Values by X-Ray Diffraction. *Powder Diffr.* 1995, 10 (1), 25–33. DOI: 10.1017/S0885715600014263

(121) Cullity, B. D. Elements of X-Ray Diffraction, 2nd ed.; Addison-Wesley Pub. Co.: Massachusetts, 1978.

(122) Tauc, J. Absorption Edge and Internal Electric Fields in Amorphous Semiconductors. *Mater. Res. Bull.* 1970, 5 (8), 721–729. DOI: 10.1016/0025-5408(70)90112-1.

(123) Ting, C. C.; Chen, S. Y.; Liu, D. M. Structural Evolution and Optical Properties of TiO_2 Thin Films Prepared by Thermal Oxidation of Sputtered Ti Films. *J. Appl. Phys.* 2000, 88 (8), 4628–4633. DOI: 10.1063/1.1309039.

(124) Zhu, J.; Zäch, M. Nanostructured Materials for Photocatalytic Hydrogen Production. *Curr. Opin. Colloid Interface Sci.* 2009, 14 (4), 260–269. DOI: 10.1016/j.cocis.2009.05.003.

(125) Hernández-Alonso, M. D.; Fresno, F.; Suárez, S.; Coronado, J. M. Development of Alternative Photocatalysts to TiO_2: Challenges and Opportunities. *Energy Environ. Sci.* 2009, 2 (12), 1231–1257. DOI: 10.1039/B907933E.

(126) Kudo, A.; Miseki, Y. Heterogeneous Photocatalyst Materials for Water Splitting. *Chem. Soc. Rev.* 2009, 38 (1), 253–278. DOI: 10.1039/B800489G.

(127) Hao, J.; Wang, Q.; Zhao, Z. Synthesis and Characterization of $G\text{-}C_3N_4/BiNbO_4$ Composite Materials with Visible Light Photocatalytic Activity. *J. Photochem. Photobiol. A Chem.* 2017, 335, 94–101. DOI: 10.1016/j.jphotochem.2016.11.002.

(128) Shi, L.; Liang, L.; Wang, F.; Liu, M.; Liang, T.; Chen, K.; Sun, J. In Situ Bubble Template Promoted Facile Preparation of Porous GC_3N_4 with Excellent Visible-Light Photocatalytic Performance. *RSC Adv*. 2015, 5 (78), 63264–63270. DOI: 10.1039/C5RA09645F.

(129) Bian, Z.; Tachikawa, T.; Zhang, P.; Fujitsuka, M.; Majima, T. Au/TiO_2 Superstructure-Based Plasmonic Photocatalysts Exhibiting Efficient Charge Separation and Unprecedented Activity. *J. Am. Chem. Soc*. 2013, 136 (1), 458–465. DOI: 10.1021/ja410994f.

(130) Chen, Y. C.; Katsumata, K.; Chiu, Y. H.; Okada, K.; Matsushita, N.; Hsu, Y. J. ZnO–Graphene Composites as Practical Photocatalysts for Gaseous Acetaldehyde Degradation and Electrolytic Water Oxidation. *Appl. Catal. A Gen.* 2015, 490, 1–9. DOI: 10.1016/j.apcata.2014.10.055.

(131) Zong, X.; Yan, H.; Wu, G.; Ma, G.; Wen, F.; Wang, L.; Li, C. Enhancement of Photocatalytic H_2 Evolution on CdS by Loading MoS_2 as Cocatalyst under Visible Light Irradiation. *J. Am. Chem. Soc.* 2008, 130 (23), 7176–7177. DOI: 10.1021/ja8007825.

(132) Chen, G.; Li, F.; Huang, Z.; Guo, C. Y.; Qiao, H.; Qiu, X.; Wang, Z.; Jiang, W.; Yuan, G. Facile Synthesis of Ag/AgBr/RGO Nanocomposite as a Highly Efficient Sunlight Plasmonic Photocatalyst. *Catal. Commun.* 2015, 59, 140–144. DOI: 10.1016/j.catcom.2014.10.008.

(133) Shang, M.; Wang, W.; Zhou, L.; Sun, S.; Yin, W. Nanosized $BiVO_4$ with High Visible-Light-Induced Photocatalytic Activity: Ultrasonic-Assisted Synthesis and Protective Effect of Surfactant. *J. Hazard. Mater.* 2009, 172 (1), 338–344. DOI: 10.1016/j.jhazmat.2009.07.017.

(134) Zhang, L.; Zhang, X.; Huang, Y. Q.; Pan, C. L.; Hu, J. S.; Hou, C. M. Novel $Bi_{12}ZnO_{20}$–Bi_2WO_6 Heterostructures: Facile Synthesis and Excellent Visible-Light-Driven Photocatalytic Activities. *RSC Adv.* 2015, 5 (38), 30239–30247. DOI: 10.1039/c5ra01327e.

(135) Tian, G.; Chen, Y.; Zhou, J.; Tian, C.; Li, R.; Wang, C.; Fu, H. In Situ Growth of Bi_2MoO_6 on Reduced Graphene Oxide Nanosheets for Improved Visible-Light Photocatalytic Activity. *CrystEngComm* 2014, 16 (5), 842–849. DOI: 10.1039/C3CE41999A.

(136) Liu, C.; Huang, H.; Du, X.; Zhang, T.; Tian, N.; Guo, Y.; Zhang, Y. In Situ Co-Crystallization for Fabrication of g-C_3N_4/Bi_5O_7I Heterojunction for Enhanced Visible-Light Photocatalysis. *J. Phys. Chem. C* 2015, 119 (30), 17156–17165. DOI: 10.1021/acs.jpcc.5b03707.

(137) Radha, R.; Muthurajan, H.; Rao, N. K.; Pradhan, S.; Gupta, U. N.; Jha, R. K.; Mirji, S. A.; Ravi, V. Low Temperature Synthesis and Characterization of $BiNbO_4$ Powders. *Mater. Charact.* 2008, 59 (8), 1083–1087. DOI: 10.1016/j.matchar.2007.08.026.

(138) Shihua, D.; Xi, Y.; Yong, Y. Dielectric Properties of B_2O_3-Doped $BiNbO_4$ Ceramics. *Ceram. Int.* 2004, 30 (7), 1195–1198. DOI: 10.1016/j.ceramint.2003.12.030.

(139) Kang, Y. J.; Ghong, T. H.; Jung, Y. W.; Byun, J. S.; Kim, S.; Kim, Y. D.; Seong, T. G.; Cho, K. H.; Nahm, S. Optical Properties of Bismuth Niobate Thin Films Studied by Spectroscopic Ellipsometry. *Thin Solid Films* 2010, 518 (22), 6526–6530. DOI: 10.1016/j.tsf.2010.01.053.

(140) Devesa, S.; Kumar, J. S.; Graça, M. P. F.; Soares, M. J.; Costa, L. C. Photoluminescence in Europium Ion–Substituted Bismuth Niobate Particles. *Spectrosc. Lett.* 2017, 50 (5), 285–288. DOI: 10.1080/00387010.2017.1321020.

(141) Setter, N.; Waser, R. Electroceramic Materials. *Acta Mater.* 2000, 48 (1), 151–178. DOI: 10.1016/S1359-6454(99)00293-1.

(142) Wang, L.; Wang, W.; Shang, M.; Sun, S.; Yin, W.; Ren, J.; Zhou, J. Visible Light Responsive Bismuth Niobate Photocatalyst: Enhanced Contaminant Degradation and Hydrogen Generation. *J. Mater. Chem.* 2010, 20 (38), 8405–8410. DOI: 10.1039/C0JM01669A.

(143) He, L.; Du, N.; Wang, C.; Chen, X.; Zhang, W. A Facile Synthesis of Graphene-Supported Mesoporous TiO_2 Hybrid Sheets with Uniform Coverage and Controllable Pore Diameters. *Microporous Mesoporous Mater.* 2015, 206, 95–101. DOI: 10.1016/j.micromeso.2014.12.015.

(144) Padhi, D. K.; Parida, K.; Singh, S. K. Facile Fabrication of RGO/N-GZ Mixed Oxide Nanocomposite for Efficient Hydrogen Production under Visible Light. *J. Phys. Chem.* C 2015, 119 (12), 6634–6646. DOI: 10.1021/acs.jpcc.5b00311.

(145) Chang, K.; Mei, Z.; Wang, T.; Kang, Q.; Ouyang, S.; Ye, J. MoS_2/Graphene Cocatalyst for Efficient Photocatalytic H_2 Evolution under Visible Light Irradiation. *ACS Nano* 2014, 8 (7), 7078–7087. DOI: 10.1021/nn5019945.

(146) Jiang, L.; Yao, M.; Liu, B.; Li, Q.; Liu, R.; Lv, H.; Lu, S.; Gong, C.; Zou, B.; Cui, T. Controlled Synthesis of CeO_2/Graphene Nanocomposites with Highly Enhanced Optical and Catalytic Properties. *J. Phys. Chem. C* 2012, 116 (21), 11741–11745. DOI: 10.1021/jp3015113.

(147) Deng, D.; Chen, N.; Li, Y.; Xing, X.; Liu, X.; Xiao, X.; Wang, Y. Cerium Oxide Nanoparticles/Multi-Wall Carbon Nanotubes Composites: Facile Synthesis and Electrochemical Performances as Supercapacitor Electrode Materials. *Phys. E Low-dimensional Syst. Nanostructures* 2017, 86, 284–291. DOI: 10.1016/j.physe.2016.10.031

(148) Min, Y. L.; Zhang, F. J.; Zhao, W.; Zheng, F. C.; Chen, Y. C.; Zhang, Y. G. Hydrothermal Synthesis of Nanosized Bismuth Niobate and Enhanced Photocatalytic Activity by Coupling of Graphene Sheets. *Chem. Eng. J.* 2012, 209, 215–222. DOI: 10.1016/j.cej.2012.07.109.

(149) Rouquerol, J.; Rouquerol, F.; Llewellyn, P.; Maurin, G.; Sing, K. S. W. Adsorption by Powders and Porous Solids: Principles, Methodology and Applications, 2nd ed.; Academic Press: Massachusetts, 2013.

(150) Sun, D.; Ye, L.; Sun, F.; García, H.; Li, Z. From Mixed-Metal MOFs to Carbon-Coated Core–Shell Metal Alloy@Metal Oxide Solid Solutions: Transformation of Co/Ni-MOF-74 to CoxNi1–X@CoyNi1–YO@C for the Oxygen Evolution Reaction. *Inorg. Chem.* 2017, 56 (9), 5203–5209. DOI: 10.1021/acs.inorgchem.7b00333.

(151) Lee, D. T.; Zhao, J.; Oldham, C. J.; Peterson, G. W.; Parsons, G. N. UiO-66-NH_2 Metal–Organic Framework (MOF) Nucleation on TiO_2, ZnO, and Al_2O_3 Atomic Layer Deposition-Treated Polymer Fibers: Role of Metal Oxide on MOF Growth and Catalytic Hydrolysis of Chemical Warfare Agent Simulants. *ACS Appl. Mater. Interfaces* 2017, 9 (51), 44847–44855. DOI: 10.1021/acsami.7b15397.

(152) Koo, W. T.; Choi, S. J.; Kim, S. J.; Jang, J. S.; Tuller, H. L.; Kim, I. D. Heterogeneous Sensitization of Metal–Organic Framework Driven Metal@Metal Oxide Complex Catalysts on an Oxide Nanofiber Scaffold Toward Superior Gas Sensors. *J. Am. Chem. Soc.* 2016, 138 (40), 13431–13437. DOI: 10.1021/jacs.6b09167.

(153) Drobek, M.; Kim, J. H.; Bechelany, M.; Vallicari, C.; Julbe, A.; Kim, S. S. MOF-Based Membrane Encapsulated ZnO Nanowires for Enhanced Gas Sensor Selectivity. *ACS Appl. Mater. Interfaces* 2016, 8 (13), 8323–8328. DOI: 10.1021/acsami.5b12062.

(154) Lin, R.; Shen, L.; Ren, Z.; Wu, W.; Tan, Y.; Fu, H.; Zhang, J.; Wu, L. Enhanced Photocatalytic Hydrogen Production Activity via Dual Modification of MOF and Reduced Graphene Oxide on CdS. *Chem. Commun.* 2014, 50 (62), 8533–8535. DOI: 10.1039/C4CC01776E.

(155) Wei, M.; Wang, X.; Duan, X. Crystal Structures and Proton Conductivities of a MOF and Two POM–MOF Composites Based on CuII Ions and 2,2′-Bipyridyl-3,3′-Dicarboxylic Acid. *Chem. A Eur. J.* 2013, 19 (5), 1607–1616. DOI: 10.1002/chem.201203154.

(156) Feng, P. L.; Perry, J. J.; Nikodemski, S.; Jacobs, B. W.; Meek, S. T.; Allendorf, M. D. Assessing the Purity of Metal−Organic Frameworks Using Photoluminescence: MOF-5, ZnO Quantum Dots, and Framework Decomposition. *J. Am. Chem. Soc.* 2010, 132 (44), 15487–15489. DOI: 10.1021/ja1065625.

(157) Ahmed, I.; Panja, T.; Khan, N. A.; Sarker, M.; Yu, J. S.; Jhung, S. H. Nitrogen-Doped Porous Carbons from Ionic Liquids@MOF: Remarkable Adsorbents for Both Aqueous and Nonaqueous Media. *ACS Appl. Mater. Interfaces* 2017, 9 (11), 10276–10285. DOI: 10.1021/acsami.7b00859.

(158) Dhainaut, J.; Bonneau, M.; Ueoka, R.; Kanamori, K.; Furukawa, S. Formulation of Metal–Organic Framework Inks for the 3D Printing of Robust Microporous Solids toward High-Pressure Gas Storage and Separation. *ACS Appl. Mater. Interfaces* 2020, 12 (9), 10983–10992. DOI: 10.1021/acsami.9b22257.

(159) Lo, Y.; Lam, C. H.; Chang, C. W.; Yang, A. C.; Kang, D. Y. Polymorphism/Pseudopolymorphism of Metal–Organic Frameworks Composed of Zinc (II) and 2-Methylimidazole: Synthesis, Stability, and Application in Gas Storage. *RSC Adv.* 2016, 6 (92), 89148–89156. DOI: 10.1039/C6RA19437K.

(160) Luo, F.; Yan, C.; Dang, L.; Krishna, R.; Zhou, W.; Wu, H.; Dong, X.; Han, Y.; Hu, T. L.; O'Keeffe, M. UTSA-74: A MOF-74 Isomer with Two Accessible Binding Sites per Metal Center for Highly Selective Gas Separation. *J. Am. Chem. Soc.* 2016, 138 (17), 5678–5684. DOI: 10.1021/jacs.6b02030.

(161) Zhang, Q.; Wang, J.; Kirillov, A. M.; Dou, W.; Xu, C.; Xu, C.; Yang, L.; Fang, R.; Liu, W. Multifunctional Ln–MOF Luminescent Probe for Efficient Sensing of Fe^{3+}, Ce^{3+}, and Acetone. *ACS Appl. Mater. Interfaces* 2018, 10 (28), 23976–23986. DOI: 10.1021/acsami.8b06103.

(162) Shen, K.; Chen, X.; Chen, J.; Li, Y. Development of MOF-Derived Carbon-Based Nanomaterials for Efficient Catalysis. *ACS Catal.* 2016, 6 (9), 5887–5903. DOI: 10.1021/acscatal.6b01222.

(163) Fortea-Pérez, F. R.; Mon, M.; Ferrando-Soria, J.; Boronat, M.; Leyva-Pérez, A.; Corma, A.; Herrera, J. M.; Osadchii, D.; Gascon, J.; Armentano, D.; et al. The MOF-Driven Synthesis of Supported Palladium Clusters with Catalytic Activity for Carbene-Mediated Chemistry. *Nat. Mater.* 2017, 16 (7), 760–766. DOI: 10.1038/nmat4910.

(164) Diercks, C. S.; Liu, Y.; Cordova, K. E.; Yaghi, O. M. The Role of Reticular Chemistry in the Design of CO_2 Reduction Catalysts. *Nat. Mater.* 2018, 17 (4), 301–307. DOI: 10.1038/s41563-018-0033-5.

(165) Chen, X.; Peng, Y.; Han, X.; Liu, Y.; Lin, X.; Cui, Y. Sixteen Isostructural Phosphonate Metal-Organic Frameworks with Controlled Lewis Acidity and Chemical Stability for Asymmetric Catalysis. *Nat. Commun.* 2017, 8 (1), 2171. DOI: 10.1038/s41467-017-02335-0.

(166) Chen, L.; Jiang, Y.; Huo, H.; Liu, J.; Li, Y.; Li, C.; Zhang, N.; Wang, J. Metal-Organic Framework-Based Composite Ni@MOF as Heterogenous Catalyst for Ethylene Trimerization. *Appl. Catal. A Gen.* 2020, 594, 117457. DOI: 10.1016/j.apcata.2020.117457.

(167) Patel, P.; Parmar, B.; Kureshy, R. I.; Khan, N. H.; Suresh, E. Amine-Functionalized Zn(Ii) MOF as an Efficient Multifunctional Catalyst for CO_2 Utilization and Sulfoxidation Reaction. *Dalt. Trans.* 2018, 47 (24), 8041–8051. DOI: 10.1039/C8DT01297K.

(168) Wang, X. S.; Liang, J.; Li, L.; Lin, Z. J.; Bag, P. P.; Gao, S. Y.; Huang, Y. B.; Cao, R. An Anion Metal–Organic Framework with Lewis Basic Sites-Rich toward Charge-Exclusive Cationic Dyes Separation and Size-Selective Catalytic Reaction. *Inorg. Chem.* 2016, 55 (5), 2641–2649. DOI: 10.1021/acs.inorgchem.6b00019.

(169) He, H.; Xue, Y. Q.; Wang, S. Q.; Zhu, Q. Q.; Chen, J.; Li, C. P.; Du, M. A Double-Walled Bimetal–Organic Framework for Antibiotics Sensing and Size-Selective Catalysis. *Inorg. Chem.* 2018, 57 (24), 15062–15068. DOI: 10.1021/acs.inorgchem.8b01898.

(170) Hu, S.; Liu, M.; Li, K.; Song, C.; Zhang, G.; Guo, X. Surfactant-Assisted Synthesis of Hierarchical NH_2-MIL-125 for the Removal of Organic Dyes. *RSC Adv.* 2017, 7 (1), 581–587. DOI: 10.1039/C6RA25745C.

(171) Wang, M.; Yang, L.; Yuan, J.; He, L.; Song, Y.; Zhang, H.; Zhang, Z.; Fang, S. Heterostructured Bi_2S_3@NH_2-MIL-125(Ti) Nanocomposite as a Bifunctional Photocatalyst for Cr(vi) Reduction and Rhodamine B Degradation under Visible Light. *RSC Adv.* 2018, 8 (22), 12459–12470. DOI: 10.1039/C8RA00882E.

(172) Armstrong, D. A.; Huie, R. E.; Koppenol, W. H.; Lymar, S. V.; Merényi, G.; Neta, P.; Ruscic, B.; Stanbury, D. M.; Steenken, S.; Wardman, P. Standard Electrode Potentials Involving Radicals in Aqueous Solution: Inorganic Radicals (IUPAC Technical Report), *Pure and App. Chem.* 2015, 87 (11-12), 1139-1150. DOI: 10.1515/pac-2014-0502.

(173) Vermoortele, F.; Vandichel, M.; Van de Voorde, B.; Ameloot, R.; Waroquier, M.; Van Speybroeck, V.; De Vos, D. E. Electronic Effects of Linker Substitution on Lewis Acid Catalysis with Metal–Organic Frameworks. *Angew. Chemie Int. Ed.* 2012, 51 (20), 4887–4890. DOI: 10.1002/anie.201108565.

(174) Sun, D.; Liu, W.; Fu, Y.; Fang, Z.; Sun, F.; Fu, X.; Zhang, Y.; Li, Z. Noble Metals Can Have Different Effects on Photocatalysis Over Metal–Organic Frameworks (MOFs): A Case Study on M/NH_2-MIL-125(Ti) (M=Pt and Au). *Chem. A Eur. J.* 2014, 20 (16), 4780–4788. DOI: 10.1002/chem.201304067.

List of Publications

Bakiro, M.; Hussein Ahmed, S.; Alzamly, A. Effect of pH, Surfactant, and Temperature on Mixed-Phase Structure and Band Gap Properties of $BiNbO_4$ Nanoparticles Prepared Using Different Routes. *Chemistry* (2019), *1*, 89-110. DOI: 10.3390/chemistry1010008.

Bakiro, M.; Hussein Ahmed, S.; Alzamly, A. Investigation of the band gap energy shift and photocatalytic properties of Bi^{3+}-doped ceria. *Inorganic Chemistry Communications* (2020), 116, 107906. DOI: 10.1016/j.inoche.2020.107906.

Hussein Ahmed, S.; Bakiro, M.; Alzamly, A. Investigation of the band gap and photocatalytic properties of CeO_2/rGO composites. *Molecular Catalysis* (2020), 486, 110874. DOI: 10.1016/j.mcat.2020.110874.

Hussein Ahmed, S.; Bakiro, M.; Alzamly, A. Visible-Light-Driven Photocatalytic Formation of Propylene Carbonate using $FeNbO_4$/Reduced Graphene Oxide Composites. *Materialia* (2020), 12, 100781. DOI: 10.1016/j.mtla.2020.100781.

Hussein Ahmed, S.; Bakiro, M.; Alzamly, A. Effect of pH and surfactant on band gap properties of monoclinic $FeNbO_4$ prepared via different routes. *Nano-Structures & Nano-Objects* (2019), 20, 100400. DOI: 10.1016/j.nanoso.2019.100400.

Alzamly, A.; Bakiro, M.; Hussein Ahmed, S.; Sallabi, S.; Al Ajeil, R.; Alawadhi, S.; Selem, H.; Al Meshayei, S.; Khaleel, A.; Al-Shamsi, N.; Saleh, N. Construction of BiOF/BiOI nanocomposites with tunable band gaps as efficient visible-light photocatalysts. *Journal of Photochemistry and Photobiology A: Chemistry* (2019), 357, 30-39. DOI: 10.1016/j.jphotochem.2019.01.031.

Alzamly, A.; Hamed, F.; Ramachandran, T.; Bakiro, M.; Hussein Ahmed, S.; Mansour, S.; Salem, S.; Abdul al, K.; Al Kaabi, N.; Meetani, M.; Khaleel, A. Tunable band gap of Bi^{3+}-doped anatase TiO_2 for enhanced photocatalytic removal of acetaminophen under UV-visible light irradiation. *Journal of Water Reuse and Desalination* (2019), 9 (1), 31–46. DOI: 10.2166/wrd.2018.021.

Alzamly, A.; Alawadhi, A.; Hussein Ahmed, S.; Bakiro, M.; Bufaroosha M. Photosensitizer Using Visible Light: An Undergraduate Laboratory Experiment Utilizing an Affordable Photocatalytic Reactor. *International Journal for Innovation Education and Research* (2018), 6, 74-84. DOI: 10.31686/ijier.Vol6.Iss11.1232

Appendices

Appendix A: Equations used in calculation.

In the $BiNbO_4$ orthorhombic structure, the plane spacing d is related to the lattice constants a, b, c and the Miller indices by the following relations

$$d_{(hkl)} = \frac{abc}{\sqrt{(h^2b^2c^2+k^2a^2c^2+l^2b^2a^2)}} \tag{1}$$

And the unit cell volume V, can be calculated from the following equation:

$$V=abc \tag{2}$$

However, in the $BiNbO_4$ triclinic structure, the plane spacing d is related to the lattice constants a, b, c and the Miller indices by the following relations:

$$\frac{1}{d_{(hkl)}} = h^2a^{*2}+k^2b^{*2}+l^2c^{*2}+2klb^*c^*\cos\alpha^*+2lhc^*a^*\cos\beta^*+2khb^*a^*\cos\gamma^* \tag{3}$$

$$a^* = \frac{bc\sin\alpha}{V} \tag{4}$$

$$b^* = \frac{ca\sin\beta}{V} \tag{5}$$

$$c^* = \frac{ab\sin\gamma}{V} \tag{6}$$

$$\cos\alpha^* = \frac{\cos\beta\cos\gamma - \cos\alpha}{\sin\beta\sin\gamma} \tag{7}$$

$$\cos\beta^* = \frac{\cos\gamma\cos\alpha - \cos\beta}{\sin\gamma\sin\alpha} \tag{8}$$

$$\cos \gamma^{*} = \frac{\cos \alpha \cos \beta - \cos \gamma}{\sin \alpha \sin \beta} \tag{9}$$

$$V = 2bc\sqrt{\sin s.\ \sin(s-\alpha)\ \sin(s-\beta).\ \sin(s-\gamma)} \tag{10}$$

Where $s = \frac{1}{2}(\alpha+\beta+\gamma)$

Appendix B: %Triclinic content.

Table A1: %Triclinic in samples prepared using co-precipitation method at 1023 K.

	CPT pH 2	CPT pH 7	CPT pH 10
Mean	45.5625	86.4075	75.9500
Std. Deviation	4.18040	6.02874	9.54446
Std. Error of Mean	2.09020	3.01437	4.77223

Table A2: %Triclinic in samples prepared using hydrothermal method at 1023 K.

	Hydrothermal pH 2	Hydrothermal pH 7	Hydrothermal pH 10
Mean	60.1350	73.9228	92.2475
Std. Deviation	6.39166	8.06165	0.90644
Std. Error of Mean	3.19583	4.03083	0.45322

Table A3: %Triclinic in samples prepared using citrate method at 1023 K.

	Citrate pH 2	Citrate pH 7	Citrate pH 10
Mean	43.3525	40.4950	75.7125
Std. Deviation	12.10862	9.46539	3.45900
Std. Error of Mean	6.05431	4.73270	1.72950

Table A4: %Triclinic in samples prepared using co-precipitation method at 1023 K with different surfactants added.

	CPT pH 2	CPT pH 2 / SDS	CPT pH 2 / EG	CPT pH 2 / PEG
Mean	45.5625	34.2063	53.5500	48.2450
Std. Deviation	4.18040	10.63029	2.05115	6.66931
Std. Error of Mean	2.09020	5.31514	1.02557	3.33465

Table A5: %Triclinic in samples prepared using co-precipitation method at 1023 K and 1173 K.

	CPT pH 2 at 1023 K	CPT pH 7 at 1023 K	CPT pH 10 at 1023 K	CPT pH 2 at 1173 K	CPT pH 7 at 1173 K	CPT pH 10 at 1173 K
Mean	45.5625	86.4075	75.9500	83.5580	85.4325	70.2675
Std. Deviation	4.18040	6.02874	9.54446	6.04369	7.12445	12.57059
Std. Error of Mean	2.09020	3.01437	4.77223	3.02184	3.56223	6.28529

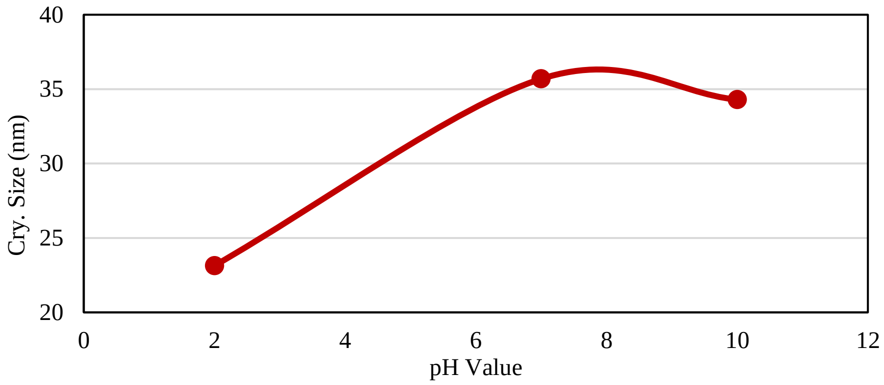

A6: Crystalline particle size vs. pH value of samples prepared using co-precipitation method calcined at 1023 K.

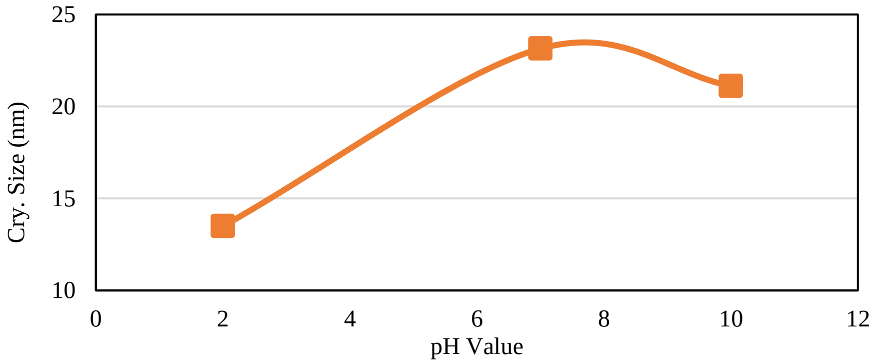

A7: Crystalline particle size vs. pH value of samples prepared using hydrothermal method and calcined at 1023 K.

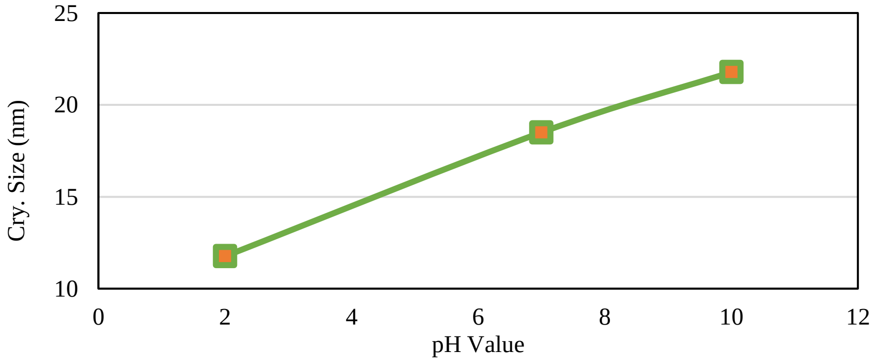

A8: Crystalline particle size vs. pH value of samples prepared using citrate method and calcined at 1023 K.

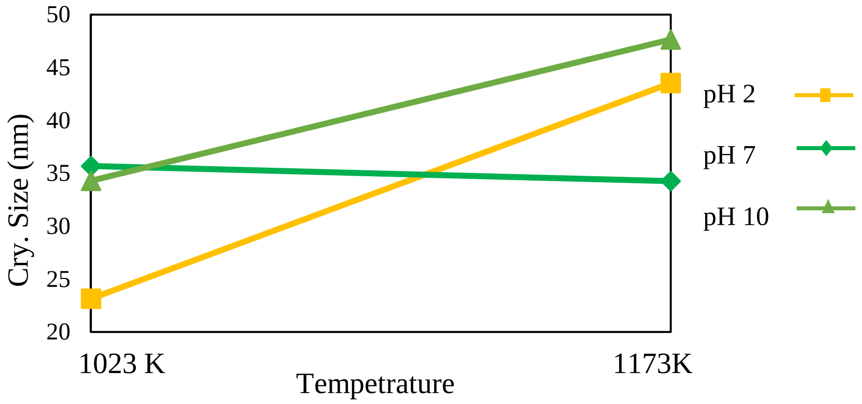

A9: Crystalline particle size vs. calcination temperature of samples prepared using co-precipitation method at different pH values.

Appendix C: Surface analysis.

Table A10: Weight and atomic percentage of $BiNbO_4$ prepared using co-precipitation method at pH 2

Element	Weight %	Atomic %
O K	16.79	65.66
Nb L	25.22	16.98
Bi M	57.98	17.35
Totals	100.00	

Table A11: Weight and atomic percentage of $BiNbO_4$ prepared using co-precipitation method at pH 7

Element	Weight %	Atomic %
O K	15.47	63.33
Nb L	25.99	18.32
Bi M	58.55	18.35
Totals	100.00	

Table A12: Weight and atomic percentage of $BiNbO_4$ prepared using co-precipitation method at pH 10

Element	Weight %	Atomic %
O K	16.60	66.24
Nb L	21.68	14.90
Bi M	61.73	18.86
Totals	100.00	

Table A13: Weight and atomic percentage of $BiNbO_4$ prepared using co-precipitation method at pH 2 with EG.

Element	Weight %	Atomic %
O K	18.99	70.94
Nb L	16.52	10.63
Bi M	64.48	18.44
Totals	100.00	

Table A14: Weight and atomic percentage of $BiNbO_4$ prepared using co-precipitation method at pH 2 with SDS.

Element	Weight %	Atomic %
O K	18.64	70.74
Nb L	15.49	10.12
Bi M	65.87	19.14
Totals	100.00	

Table A15: Weight and atomic percentage of $BiNbO_4$ prepared using co-precipitation method at pH 2 with PEG.

Element	Weight %	Atomic %
O K	14.92	64.13
Nb L	19.11	14.15
Bi M	65.97	21.72
Totals	100.00	

Table A16: Weight and atomic percentage of $BiNbO_4$ prepared using citrate method at pH 2

Element	Weight %	Atomic %
O K	21.70	72.76
Nb L	22.23	12.84
Bi M	56.07	14.40
Totals	100.00	

Table A17: Weight and atomic percentage of $BiNbO_4$ prepared using citrate method at pH 7.

Element	Weight %	Atomic %
O K	30.10	74.96
Nb L	49.18	21.09
Bi M	20.72	3.95
Totals	100.00	

Table A18: Weight and atomic percentage of $BiNbO_4$ prepared using citrate method at pH 10.

Element	Weight %	Atomic %
O K	19.54	70.36
Nb L	21.64	13.42
Bi M	58.82	16.22
Totals	100.00	

Table A19: Weight and atomic percentage of $BiNbO_4$ prepared using hydrothermal method at pH 2.

Element	Weight %	Atomic %
O K	25.36	76.67
Nb L	20.96	10.91
Bi M	53.68	12.42
Totals	100.00	

Table A20: Weight and atomic percentage of $BiNbO_4$ prepared using hydrothermal method at pH 7.

Element	Weight %	Atomic %
O K	22.74	74.16
Nb L	21.03	11.81
Bi M	56.23	14.04
Totals	100.00	

Table A21: Weight and atomic percentage of $BiNbO_4$ prepared using hydrothermal method at pH 10.

Element	Weight %	Atomic %
O K	23.05	74.11
Nb L	22.60	12.51
Bi M	54.35	13.38
Totals	100.00	

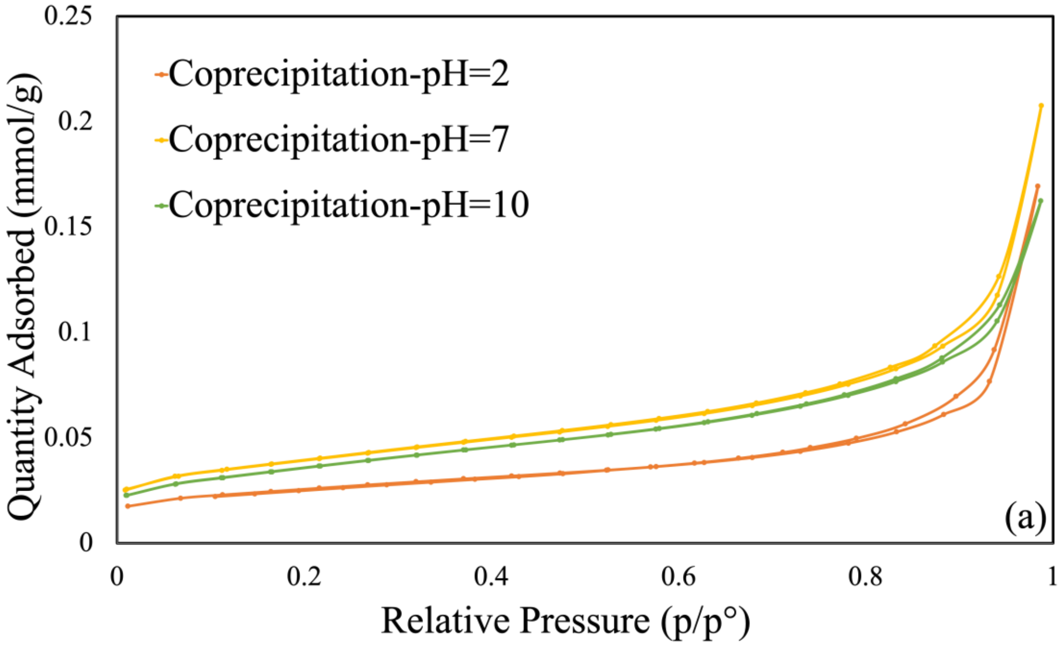

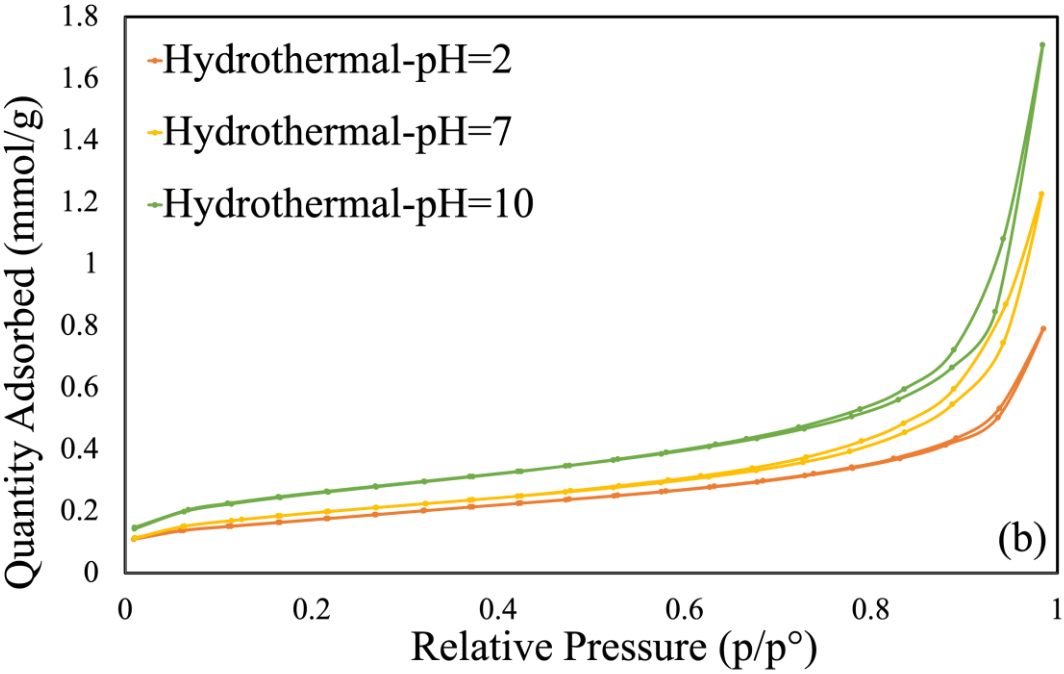

A22: BET analyses of $BiNbO_4$ calcined at 1023 K and synthesized using different synthetic approaches at different pH values; (a) co-precipitation, (b) hydrothermal, (c) citrate precursor method, (d) different surfactant added.

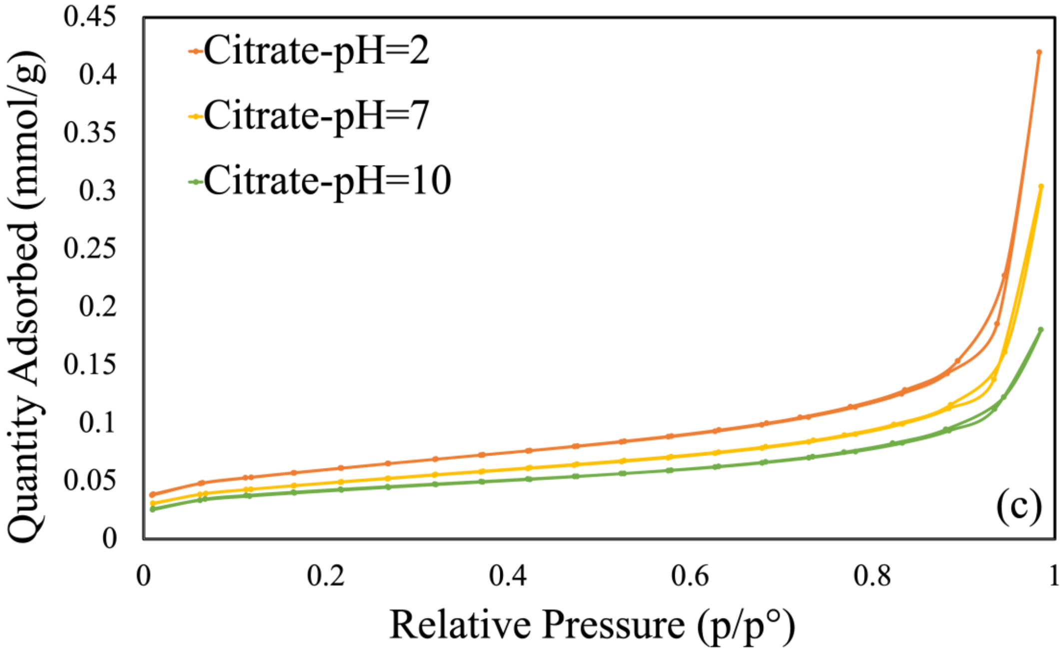

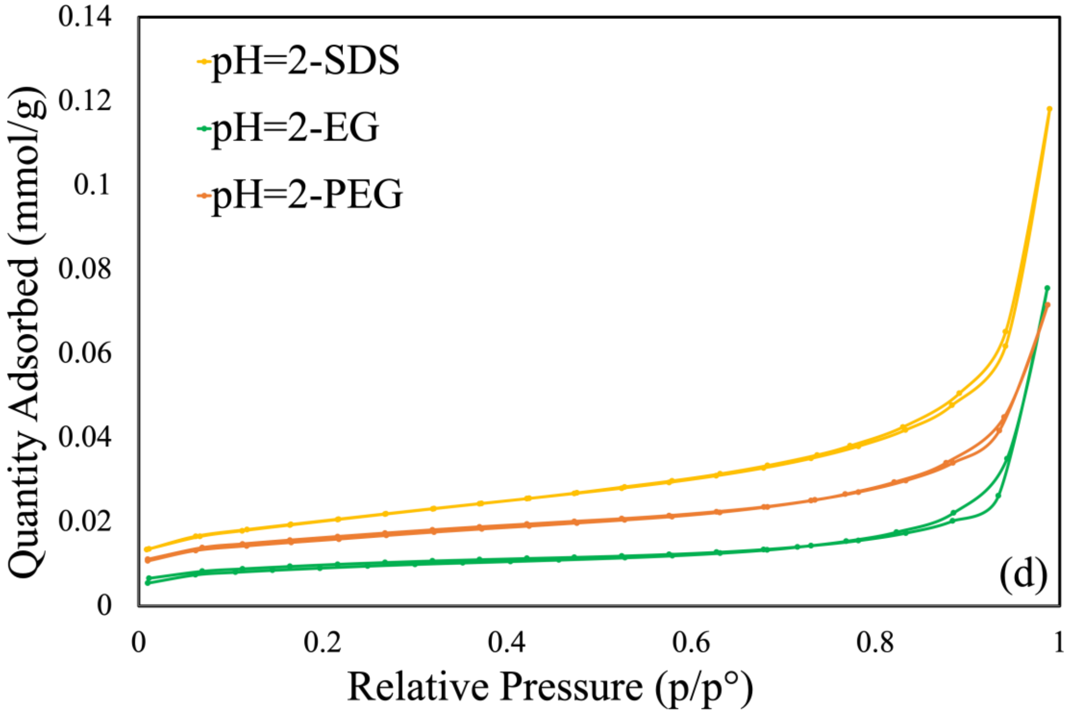

A22: BET analyses of $BiNbO_4$ calcined at 1023 K and synthesized using different synthetic approaches at different pH values; (a) co-precipitation, (b) hydrothermal, (c) citrate precursor method, (d) different surfactant added, (continued).

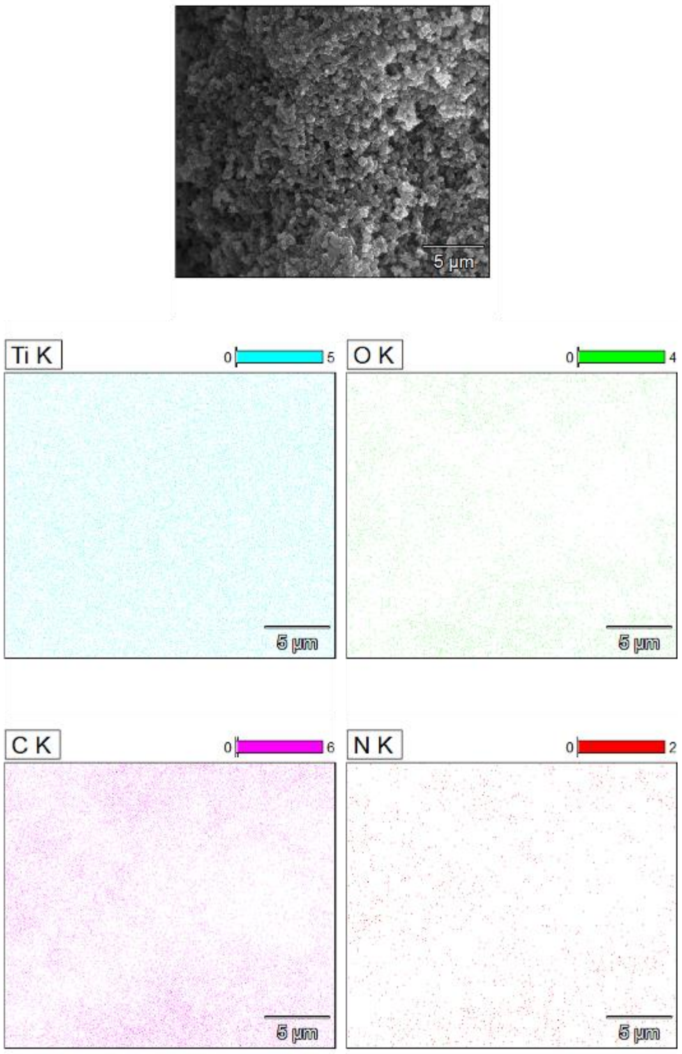

(a)

A23: EDX mapping images of: (a) NH_2-MIL-125(Ti), (b) $BiNbO_4$, (c) $BiNbO_4$/NH_2-MIL-125(Ti) $_{(25:75)}$, (d) $BiNbO_4$/NH_2-MIL-125(Ti)$_{(50:50)}$, (e) $BiNbO_4$/NH_2-MIL-125(Ti)$_{(75:25)}$.

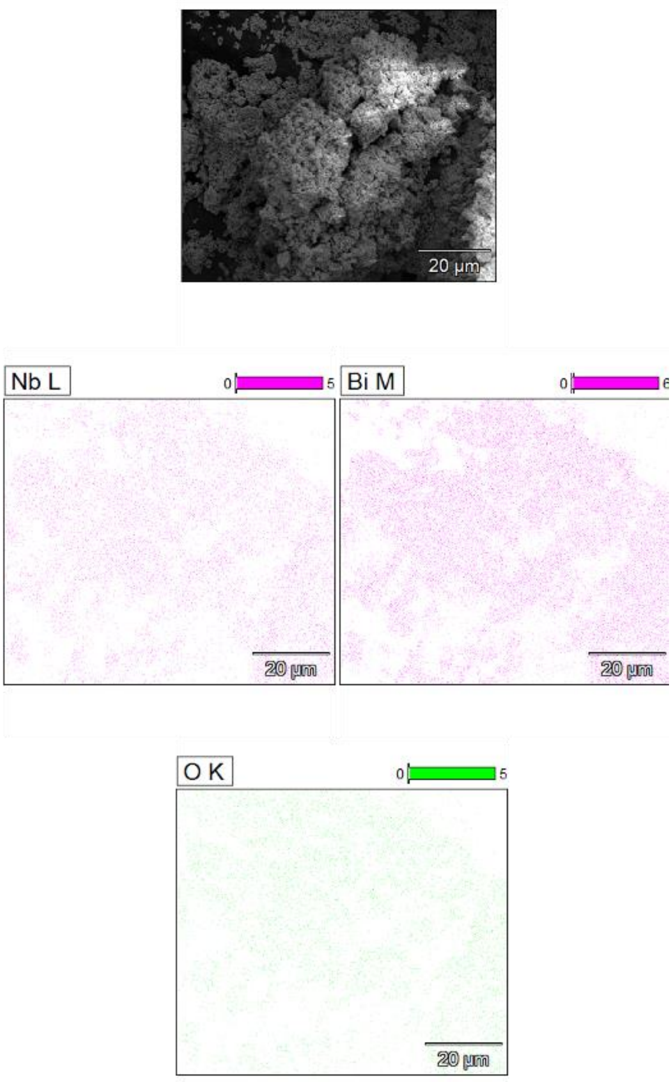

(b)

A23: EDX mapping images of: (a) NH_2-MIL-125(Ti), (b) $BiNbO_4$, (c) $BiNbO_4$/NH_2-MIL-125(Ti) $_{(25:75)}$, (d) $BiNbO_4$/NH_2-MIL-125(Ti)$_{(50:50)}$, (e) $BiNbO_4$/NH_2-MIL-125(Ti)$_{(75:25)}$, (continued)

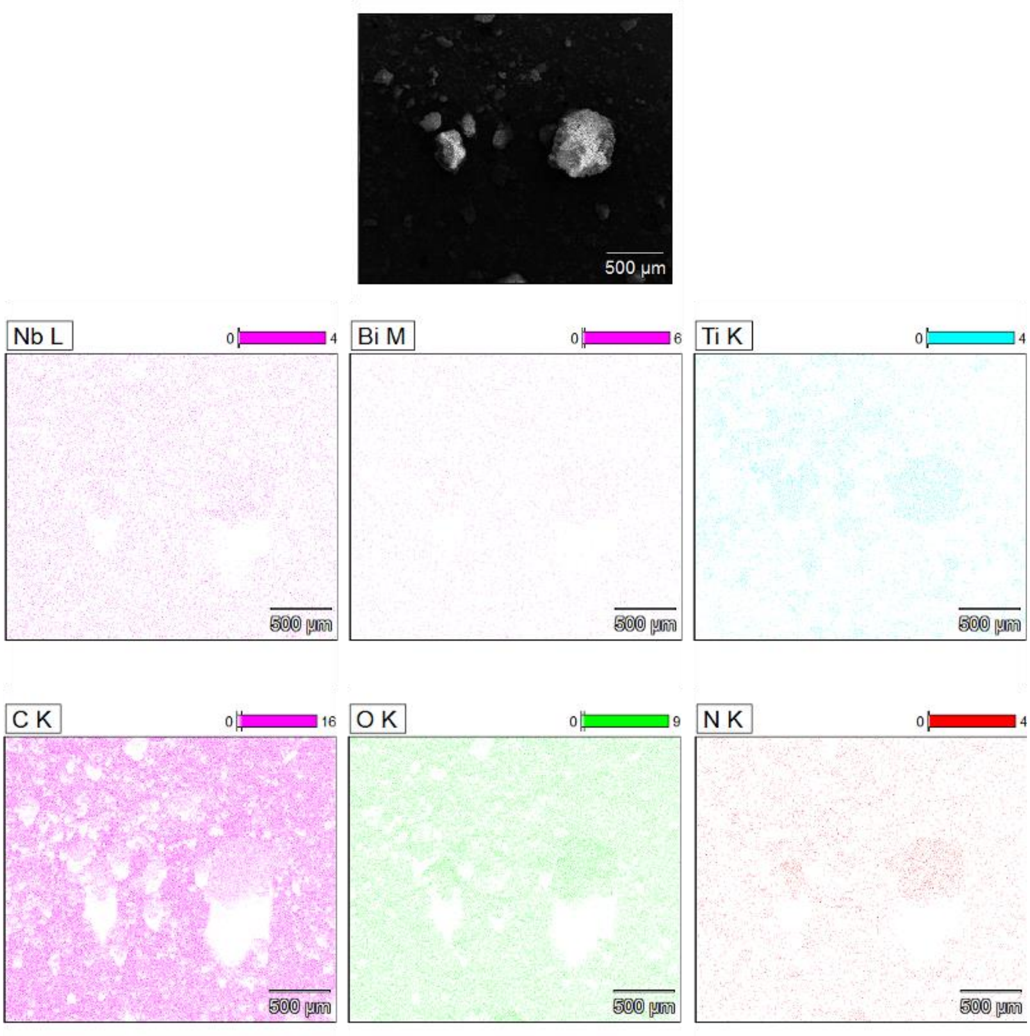

(c)

A23: EDX mapping images of: (a) NH_2-MIL-125(Ti), (b) $BiNbO_4$, (c) $BiNbO_4$/NH_2-MIL-125(Ti) $_{(25:75)}$, (d) $BiNbO_4$/NH_2-MIL-125(Ti)$_{(50:50)}$, (e) $BiNbO_4$/NH_2-MIL-125(Ti)$_{(75:25)}$, (continued)

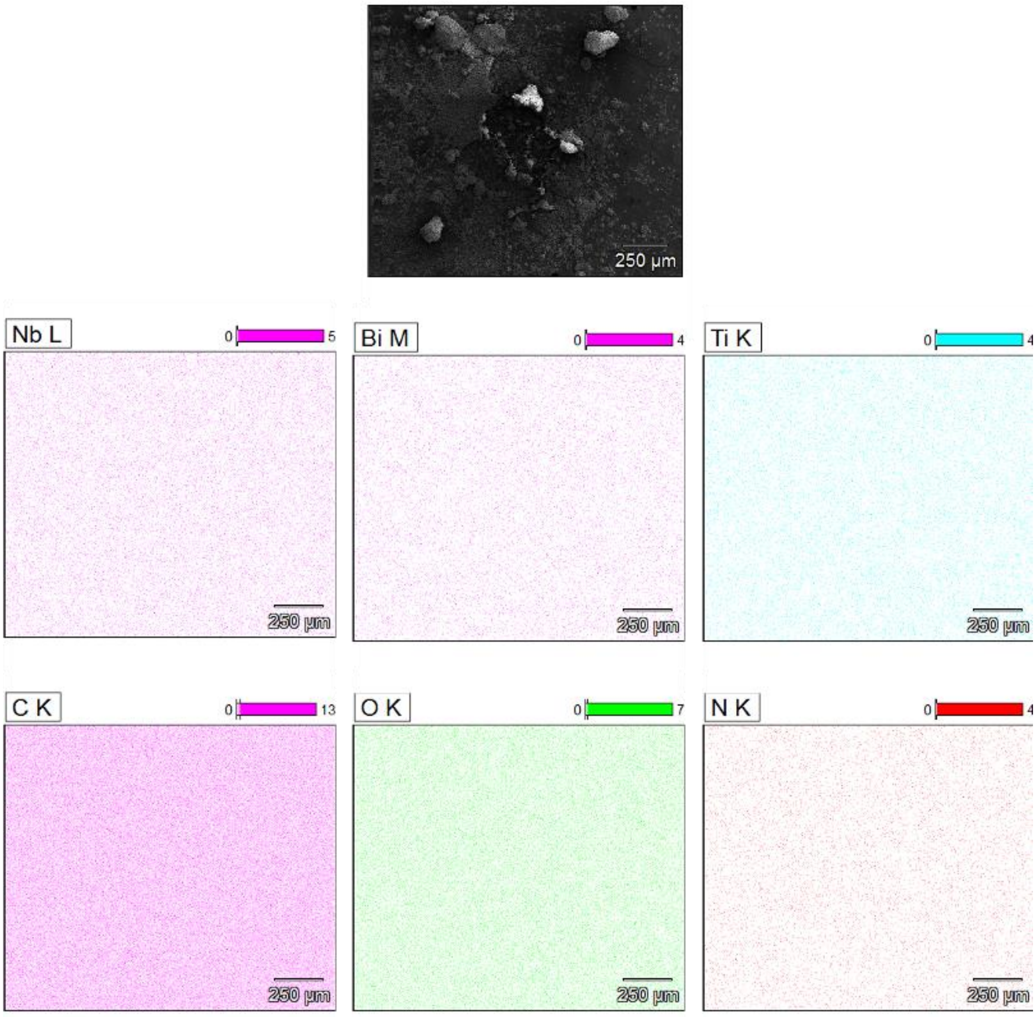

(d)

A23: EDX mapping images of: (a) NH_2-MIL-125(Ti), (b) $BiNbO_4$, (c) $BiNbO_4/NH_2$-MIL-125(Ti) $_{(25:75)}$, (d) $BiNbO_4/NH_2$-MIL-125(Ti)$_{(50:50)}$, (e) $BiNbO_4/NH_2$-MIL-125(Ti)$_{(75:25)}$, (continued)

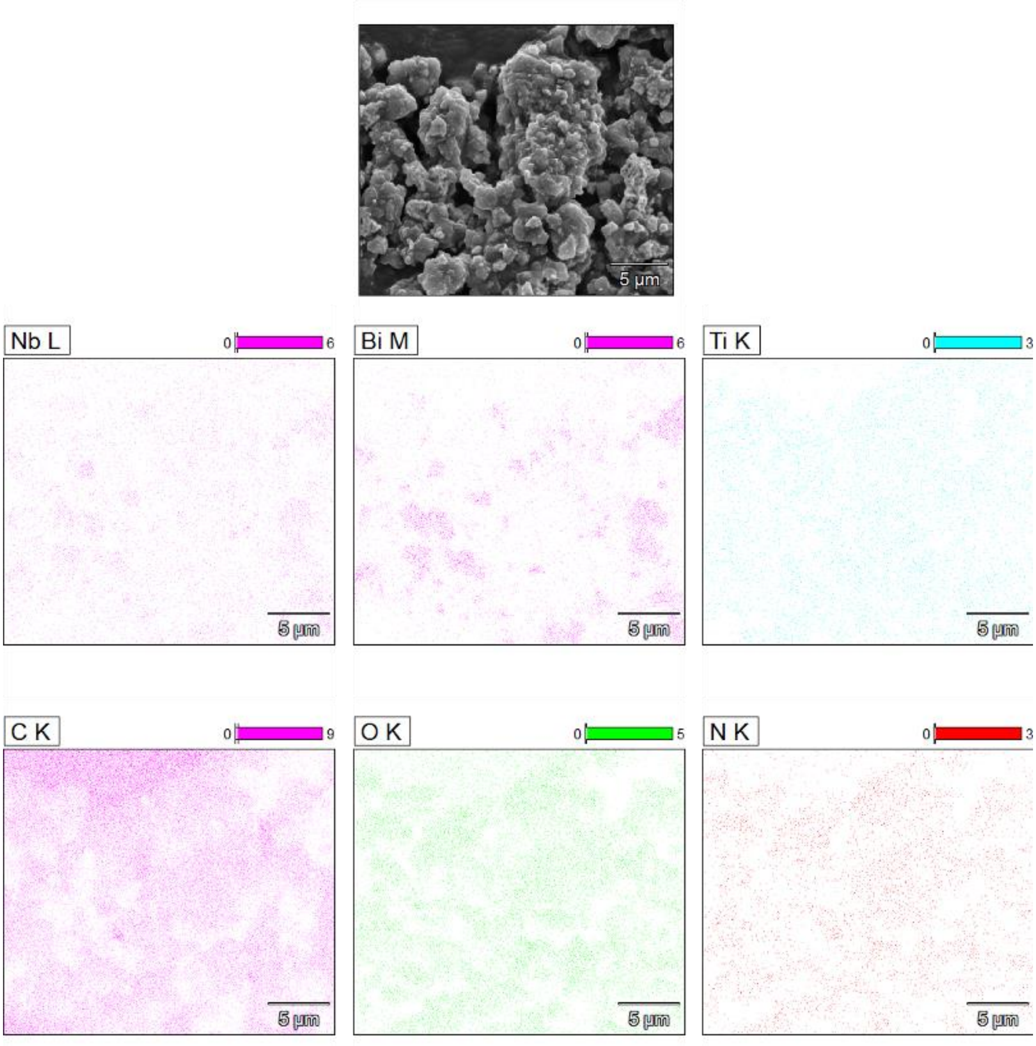

(e)

A23: EDX mapping images of: (a) NH_2-MIL-125(Ti), (b) $BiNbO_4$, (c) $BiNbO_4$/NH_2-MIL-125(Ti) $_{(25:75)}$, (d) $BiNbO_4$/NH_2-MIL-125(Ti)$_{(50:50)}$, (e) $BiNbO_4$/NH_2-MIL-125(Ti)$_{(75:25)}$, (continued)

Appendix D: Analysis of cyclic propylene carbonate.

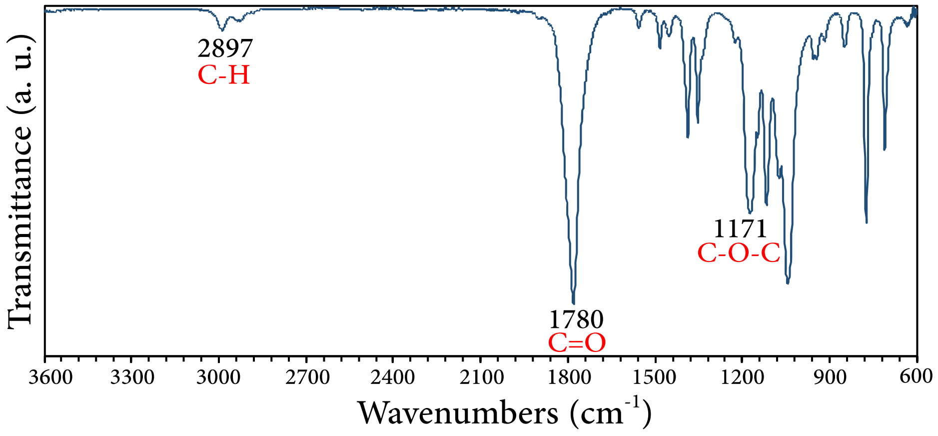

A24: FT-IR spectrum of cyclic propylene carbonate.

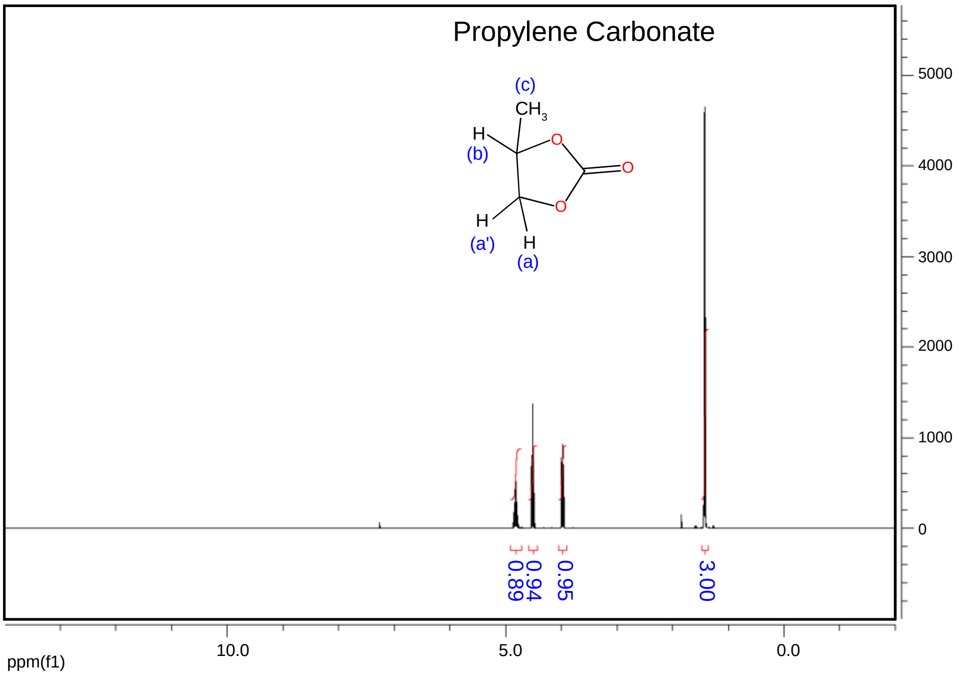

A25: ^{1}H NMR of cyclic propylene carbonate.

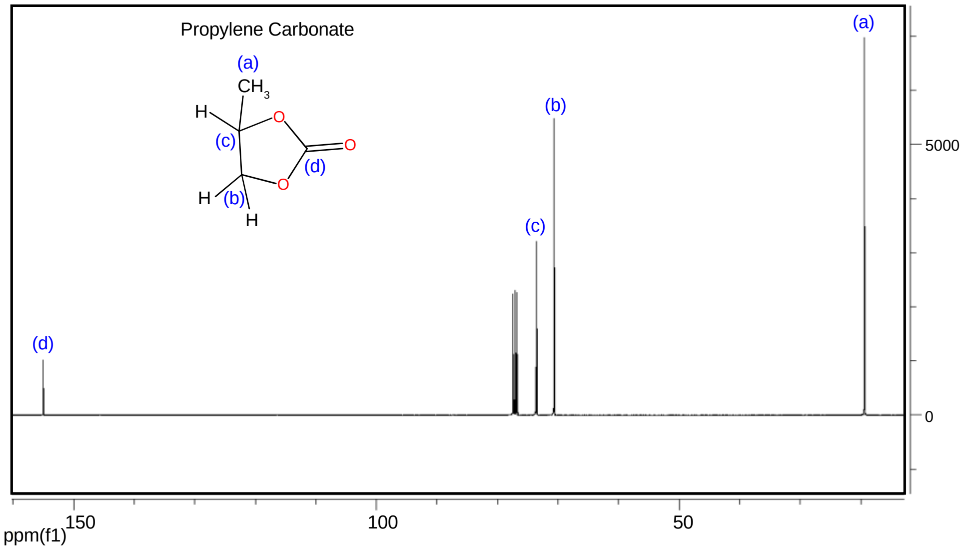

A26: ^{13}C NMR of cyclic propylene carbonate.